Aeroelastic Analysis of a Wind Turbine Blade Using the Harmonic Balance Method

A Dissertation Presented for the

Doctor of Philosophy

Degree

The University of Tennessee, Knoxville

Jason Charles Howison

December 2015

© by Jason Charles Howison, 2015
All Rights Reserved.

To my wife, Patty

Acknowledgements

I would like to thank my dissertation advisor, Dr. Kivanc Ekici. He has been tremendously helpful in both my research and preparing me for my career. We have developed a great relationship over the past few years, and I look forward to future collaborations.

I would also like to thank Dr. Robert Moore and Dr. Trevor Moeller from the University of Tennessee Space Institute (UTSI). Both were very generous with their time to give me guidance when I desperately needed it. Many thanks to my dissertation committee as well for agreeing to serve and providing insightful feedback. I am also grateful for the financial support provided by UTSI and the National Science Foundation under Grant No: CBET-1150332.

During my tenure at the University of Tennessee, I was privileged to work one summer at Wright-Patterson Air Force Base. I would like to thank Dr. Phil Beran for sponsoring and supervising my time there. I'd also like to thank Dr. Jeffrey Thomas of Duke University for his valuable input on the harmonic balance method and flutter throughout my dissertation work.

My friends and family have been extremely helpful throughout my doctoral work. I especially thank my wife Patty for her unwaivering support through the ups and downs. I also must thank Dr. Jack Abboud for his companionship as we determined the direction of our dissertations together. Finally, I wish to thank my parents for nothing but complete support for my education and the pursuit of my dreams.

Abstract

Most current wind turbine aeroelastic codes rely on the blade element momentum method with empirical corrections to compute aerodynamic forces on the wind turbine blades. While efficient, this method relies on experimental data and does not allow designers much flexibility for alternative blade designs. Unsteady solutions to the Navier-Stokes equations offer a significant improvement in aerodynamic modeling, but these are currently too computationally expensive to be useful in a design situation. However, steady-state solutions to the Navier-Stokes equations are possible with reasonable computation times. The harmonic balance method provides a way to represent unsteady, periodic flows through coupled a set of steady-state solutions. This method offers the possibility of unsteady flow solutions at a computational cost on the order of a few steady-state solutions. By coupling a harmonic balance driven aerodynamic model with a mode shape-based structural dynamics model, an efficient aeroelastic model for a wind turbine blade driven by the Navier-Stokes equations is developed in this dissertation.

For wind turbine flows, turbulence modeling is essential, especially in the transition of the boundary layer from laminar to turbulent. As part of this dissertation, the Spalart-Allmaras turbulence model and the gamma-Re_theta-t transition model are included in the aerodynamic model. This marks the first time that this transition model, turbulence model, and the harmonic balance method have been coupled to study unsteady wind turbine aerodynamics. Results show that the

transition model matches experimental data more closely than a fully turbulent model for the onset of both static and dynamic stall.

Flutter is of particular interest as turbines continue to increase in size, and longer and softer blades continue to enter the field. In this dissertation, flutter is investigated for the 1.5 MW WindPACT rotor blade. The aeroelastic model created, which incorporates the harmonic balance method and a fully turbulent aerodynamic model, is the first of its kind for wind turbine flutter analysis. Predictions match those of other aeroelastic models for the 1.5 MW WindPACT blade, and the first flapwise and edgewise modes are shown to dominate flutter for the rotor speeds considered.

Table of Contents

1 Introduction **1**

1.1 Motivation 1

1.2 Related Work 2

1.2.1 Wind Turbine Aerodynamics 3

1.2.2 Wind Turbine Aeroelasticity 7

1.3 Contributions to State of the Art 11

1.4 Outline 12

2 Governing Equations **14**

2.1 Navier-Stokes Equations 14

2.1.1 Viscous Stresses 16

2.1.2 Perfect Gas Model 16

2.1.3 Rotating Frame of Reference 17

2.2 Spalart-Allmaras Turbulence Model 19

2.3 Transition Model 21

2.4 Harmonic Balance Equations 25

2.5 Structural Dynamics 27

3 Numerical Approach for Flow Solver **31**

3.1 Non-Dimensionalization 31

3.2 Spatial Discretization 32

3.2.1 Grid Topology 33

3.2.2 Cell-Centered Approach 34
3.2.3 Convective Fluxes 35
3.2.4 Viscous Fluxes 42
3.3 Temporal Discretization 45
3.3.1 Runge-Kutta Scheme 46
3.3.2 Lower-Upper Symmetric Gauss-Seidel Scheme (LU-SGS) . . . 49
3.4 Discrete Boundary Conditions 53
3.4.1 Solid Wall 53
3.4.2 Far Field 57
3.4.3 Coordinate Cut 60
3.4.4 Periodic Boundary 60
3.5 Convergence Acceleration Techniques 60
3.5.1 Local Time Stepping 61
3.5.2 Residual Smoothing 61
3.5.3 Multigrid 61
3.5.4 Low Speed Preconditioning 65

4 Numerical Approach for Structural Solver **70**
4.1 Conversion to Frequency Domain 70
4.2 Aeroelastic Solution Technique 72

5 Validation Studies **74**
5.1 Steady Flat Plate 74
5.2 Steady Aerospatiale-A Airfoil 76
5.3 Pitching NACA 64A010 Airfoil 78
5.4 Steady ONERA M6 Wing 81
5.5 Caradonna-Tung Rotor 82
5.6 Vortex-Shedding Cylinder in Cross Flow 84
5.7 AGARD 445.6 Wing 88

6 Pitching S809 Airfoil **93**

6.1 Steady Results 93

6.2 Unsteady Results 98

7 WindPACT Flutter Analysis **107**

7.1 Model Properties 107

7.2 Structural Analysis 108

7.3 Steady Aerodynamics 111

7.4 Flutter Analysis 114

8 Conclusion **124**

8.1 Summary 124

8.2 Future Work 125

Bibliography **126**

Appendix **139**

A Face Vectors in 3-D 140

Vita **142**

List of Tables

3.1 Coefficients for Hybrid Multistage Runge-Kutta Scheme 47

3.2 Far Field Boundary Conditions 59

5.1 Sample AGARD 445.6 Turbulent Flutter Calculation, $M_\infty = 0.960$ . . 91

6.1 Unsteady S809 Airfoil Simulation Matrix 99

7.1 Characteristics of 1.5 MW Baseline WindPACT Blade 108

7.2 WindPACT Natural Frequencies (Hz) 110

7.3 Sample WindPACT Flutter Calculation, $M_{tip} = 0.500$ 117

List of Figures

1.1 Streamtube around an actuator disc representing a 1-D model of a wind turbine rotor. 3

1.2 In-plane and out-of-plane blade deflections. 8

3.1 C-grid topology. **Left**: Physical plane. **Right**: Computational plane. 33

3.2 Cell-centered discretization 35

3.3 Viscous flux auxiliary cell 43

3.4 Viscous flux auxiliary cell 45

3.5 Split flux Jacobian definitions for LU-SGS operators in cell i, j 51

3.6 Wall adjacent and ghost cells at a solid boundary 54

3.7 Characteristics at subsonic inflow boundary 57

3.8 Multigrid V-cycle. Symbols designate: $\bullet$ solve equations and restrict solution and $\circ$ prolongate corrections. 62

3.9 Restriction of residual to coarse grid. 63

3.10 Zeroth order prolongation of coarse grid correction to finer grid. . . . 65

5.1 577 x 257 flat plate C-grid. 75

5.2 Boundary layer quantities for a flat plate with Re = 5 million at $x = 1$ and $M = 0.2$. **Top Left**: Skin friction along the upper surface. **Top Right**: Ratio of eddy viscosity to free stream viscosity at $x = 0.97$. **Bottom Left**: Law of the wall at $x = 0.97$. **Bottom Right**: Velocity profile at $x = 0.97$. 76

5.3 Ratio of the turbulent eddy viscosity to the free stream viscosity for a flat plate with Re = 5 million at $x = 1$. **Left:** CFL3D. **Right:** Current solver. 77
5.4 321 x 129 Aerospatiale-A C-grid. 77
5.5 Boundary layer transition along upper surface of Aerospatiale-A airfoil showing increase in intermittency and corresponding increase in eddy viscosity. **Left**: Intermittency, γ. **Right**: Non-dimensional eddy viscosity, μ_T/μ_∞. 78
5.6 NACA 64A010 C-grid. **Left**: 193 x 33 inviscid grid. **Right**: 225 x 65 viscous grid. 79
5.7 Pitching NACA 64A010 airfoil force coefficients. **Left:** Lift coefficient. **Right:** Moment coefficient. 80
5.8 Convergence history for pitching NACA 64A010 airfoil. 80
5.9 Inviscid ONERA M6 wing C-H grid (193 x 33 x 33). 81
5.10 Coefficient of pressure distribution for ONERA M6 wing. **Top Left:** 20% span. **Top Middle:** 44% span. **Top Right:** 65% span. **Bottom Left:** 80% span. **Bottom Middle:** 90% span. **Bottom Right:** 95% span. 82
5.11 Contours of pressure on ONERA M6 wing and symmetry plane. **Left:** Inviscid. **Right:** Turbulent. 83
5.12 Viscous Caradonna-Tung C-H grid (257 x 65 x 33). 83
5.13 Coefficient of pressure distribution for Caradonna-Tung rotor in hover with tip Mach number of 0.439. 84
5.14 Coefficient of pressure distribution for Caradonna-Tung rotor in hover with tip Mach number of 0.877. 85
5.15 Contours of static pressure for Caradonna-Tung rotor in hover with tip Mach number of 0.877. **Top Left:** 50% span. **Top Middle:** 65% span. **Top Right:** 77% span. **Bottom Left:** 87% span. **Bottom Middle:** 97% span. **Bottom Right:** 100% span. 86

5.16 Infinite span cylinder O-grid (257 x 129). 87
5.17 Lift coefficient for Re = 100. **Left:** Temporal lift coefficient. **Right:** FFT of temporal lift coefficient. 88
5.18 Contours of vorticity through one cycle of vortex shedding with Re = 100. 89
5.19 Measured mode shapes for AGARD 445.6 Weakened configuration. **Top Left:** Mode one (first bending) 9.6 Hz. **Top Right:** Second Mode (first twisting) 38.2 Hz. **Bottom Left:** Third mode (second bending) 48.4 Hz. **Bottom Right:** Fourth mode (second twisting) 91.5 Hz. 90
5.20 Inviscid and viscous predictions for AGARD 445.6 wing. **Left:** Flutter velocity. **Right:** Frequency ratio. 92

6.1 S809 C-grid, 449 x 129 nodes. 94
6.2 Steady force coefficients. **Left:** Lift. **Middle:** Drag. **Right:** Moment. 95
6.3 Coefficients of pressure. **Left:** 4.1°. **Right:** 12.2°. 96
6.4 Non-dimensional eddy viscosity contours at 4.1°. **Top:** With transition model. **Bottom:** Fully turbulent. 96
6.5 Non-dimensional eddy viscosity contours at 12.2°. **Top:** With transition model. **Bottom:** Fully turbulent. 97
6.6 Transition model intermittency contours. **Top:** 4.1°. **Bottom:** 12.2°. 97
6.7 Steady convergence rates. L2 norm computed from residuals from Navier-Stokes and Spalart-Allmaras equations. 98
6.8 Case 1 lift coefficients. Mean angle of attack is 8.0°, oscillation amplitude is 5.5°, reduced frequency is 0.026, and Reynolds number is 1.01 million. **Left:** With transition model. **Right:** Fully turbulent. 100
6.9 Case 1 drag coefficients. Mean angle of attack is 8.0°, oscillation amplitude is 5.5°, reduced frequency is 0.026, and Reynolds number is 1.01 million. **Left:** With transition model. **Right:** Fully turbulent. 101

6.10 Case 1 moment coefficients. Mean angle of attack is 8.0°, oscillation amplitude is 5.5°, reduced frequency is 0.026, and Reynolds number is 1.01 million. **Left:** With transition model. **Right:** Fully turbulent. . 101
6.11 Case 1 contours of velocity magnitude at 10° angle of attack with transition. **Left:** Upstroke. **Right:** Downstroke. 102
6.12 Case 1 fully turbulent contours of velocity magnitude at 10° angle of attack. **Left:** Upstroke. **Right:** Downstroke. 102
6.13 Case 1 contours of vorticity and streamlines throughout a complete cycle with transition. Arrows indicate either upstroke or downstroke portion of the cycle. 103
6.14 Case 1 fully turbulent contours of vorticity and streamlines throughout a complete cycle. Arrows indicate either upstroke or downstroke portion of the cycle. 103
6.15 Case 2 force coefficients. The transition model solution contains 7 harmonics, and the fully turbulent solution contains 5 harmonics. Mean angle of attack is 8.0°, oscillation amplitude is 5.5°, reduced frequency is 0.077, and Reynolds number is 1.00 million. **Left:** Lift. **Middle:** Drag. **Right:** Moment. 104
6.16 Case 2 contours of vorticity and streamlines at 10° angle of attack with transition. **Top:** Upstroke. **Bottom:** Downstroke. 105
6.17 Case 3 force coefficients. The transition model solution contains 7 harmonics, and the fully turbulent solution contains 5 harmonics. Mean angle of attack is 20.0°, oscillation amplitude is 5.5°, reduced frequency is 0.025, and Reynolds number is 1.00 million. **Left:** Lift. **Middle:** Drag. **Right:** Moment. 105
6.18 Case 3 contours of vorticity and streamlines at 14.5° angle of attack. . 106

6.19 Case 4 force coefficients. The transition model solution contains 7 harmonics, and the fully turbulent solution contains 5 harmonics. Mean angle of attack is 8.0°, oscillation amplitude is 10.0°, reduced frequency is 0.077, and Reynolds number is 0.98 million. **Left:** Lift. **Middle:** Drag. **Right:** Moment. 106

7.1 WindPACT 1.5 MW blade geometry. **Left:** Blade planform. **Right:** Blade profiles from near root to tip. 108

7.2 Campbell diagram for WindPACT rotor blade. 110

7.3 Computed mode shapes for WindPACT blade rotating at 2 rad/s. **Top Left:** Mode one (1st flapwise) 1.28 Hz. **Top Right:** Second Mode (1st edgewise) 2.00 Hz. **Bottom Left:** Third mode (2nd flapwise) 3.45 Hz. **Bottom Right:** Sixth mode (1st torsion) 11.64 Hz. 111

7.4 Viscous WindPACT C-H grid (257 x 65 x 33). The grid on the right shows the blade starting at 39% span. 112

7.5 Coefficient of pressure distribution for 1.5 MW WindPACT rotor operating at 42 RPM in still air. 113

7.6 Generalized aerodynamic forces for mode shape one with $M_{tip} = 0.500$. 115

7.7 Generalized aerodynamic forces for mode shape two with $M_{tip} = 0.500$. 115

7.8 Generalized aerodynamic forces for mode shape three with $M_{tip} = 0.500$. 116

7.9 Generalized aerodynamic forces for mode shape four with $M_{tip} = 0.500$. 116

7.10 Generalized aerodynamic forces for mode shape six with $M_{tip} = 0.500$. 117

7.11 Real and imaginary pressures for 1st flapwise mode for 1.5 MW WindPACT rotor operating at $M_{tip} = 0.500$. 119

7.12 Real and imaginary pressures for 1st edgewise mode for 1.5 MW WindPACT rotor operating at $M_{tip} = 0.500$. 120

7.13 Unsteady pressure distributions ($\bar{p}/0.5\rho U_{tip}^2$) on suction and pressure sides of WindPACT blade surface for first flapwise mode with $M_{tip} = 0.500$. Real component is shown in (a), and imaginary component is shown in (b). 120
7.14 Unsteady pressure distributions ($\bar{p}/0.5\rho U_{tip}^2$) on suction and pressure sides of WindPACT blade surface for first edgewise mode with $M_{tip} = 0.500$. Real component is shown in (a), and imaginary component is shown in (b). 121
7.15 Generalized aerodynamic forces for mode shape one with $M_{tip} = 0.475$. 121
7.16 Generalized aerodynamic forces for mode shape two with $M_{tip} = 0.475$. 122
7.17 Generalized aerodynamic forces for mode shape one with $M_{tip} = 0.525$. 122
7.18 Generalized aerodynamic forces for mode shape two with $M_{tip} = 0.525$. 122
7.19 Frequency ratio 123

1 Face vectors on a 3-D volume 140

Nomenclature

α	angle of attack
γ	specific heat ratio or intermittency
δ	Kronecker delta or boundary layer thickness
θ	momentum thickness
κ	reduced frequency
λ	second viscosity coefficient or spectral radius
μ	reduced mass
μ_l	laminar viscosity
μ_t	eddy viscosity
$\tilde{\nu}$	Spalart-Allmaras working turbulent variable
ξ, η, ζ	computational plane coordinates
ρ	density
τ	pseudo-time or shear stress
τ_{xx},τ_{xy}, etc.	viscous stresses
$\mathbf{\Phi}$	modal matrix

ϕ_i	i^{th} mode shape
$\boldsymbol{\phi}$	eigenvector
σ	internal stress
Ψ	Roe scheme limiter
Ω	vorticity magnitude or angular velocity
ω	frequency or turbulent dissipation rate
$\bar{\omega}$	reduced frequency
$\boldsymbol{A}_n, \boldsymbol{B}_n$	n^{th} temporal Fourier coefficients
$\mathbf{A}_{Roe}$	Roe averaged matrix
b_s	root semi-chord
$\boldsymbol{C}_q$	generalized force vector
c	speed of sound
c_p, c_v	specific heat at constant pressure or volume
c_r	root chord
$\mathbf{D}$	pseudo-spectral operator
$\boldsymbol{D}$	artificial dissipation vector
d	wall distance
E	total energy
$\mathbf{E}, \mathbf{E}^{-1}$	discrete inverse Fourier and Fourier transformation matrices
$\boldsymbol{F}$	generalized aerodynamic force vector

$\boldsymbol{F_c}$	convective flux vector
$\boldsymbol{F}, \boldsymbol{G}, \boldsymbol{H}$	conservation flux vectors
$\boldsymbol{F}_r, \boldsymbol{G}_r, \boldsymbol{H}_r$	conservation flux vectors in relative velocity frame
$\dot{f}, \dot{g}, \dot{h}$	unsteady grid velocity
$\mathbf{G}$	matrix of aerodynamic transfer functions
f_e	external force
h	enthalpy
$\mathbf{I}$	identity matrix
I	rothalpy
J	coordinate transformation Jacobian
$\mathbf{K}$	structural stiffness matrix
k	coefficient of thermal conductivity
k_j	generalized stiffness
$\mathbf{M}$	structural mass matrix
M	Mach number
m_j	generalized mass
$\hat{\boldsymbol{n}}$	unit normal vector
p	pressure
Pr_l	laminar Prandtl number
Pr_t	turbulent Prandtl number

q_i	i^{th} modal displacement
$\mathbf{R}$	rotation matrix
$\boldsymbol{R}$	residual vector
R_{gas}	specific gas constant
Re_{θ_c}	critical Reynolds number
Re_{θ_ν}	vorticity Reynolds number
$\overline{\mathrm{Re}_{\theta t}}$	momentum thickness Reynolds number
R_T	viscosity ratio
$\boldsymbol{S}$	source term vector or control volume face vector
S	strain rate magnitude
T	temperature or period
t	time
$\boldsymbol{U}$	conservation variables vector
$\boldsymbol{U}^*$	conservation variables vector for all sub-time levels
$\tilde{\boldsymbol{U}}$	Fourier coefficient vector of conservation variables
u, v, w	Cartesian velocity components
$u_\Omega, v_\Omega, w_\Omega$	rotational velocity components
u_r, v_r, w_r	relative velocity components
$\mathcal{V}$	volume
V_f	reduced velocity

$\boldsymbol{x}$	vector of physical displacements
x, y, z	Cartesian coordinates

Chapter 1

Introduction

1.1 Motivation

The next generation of wind turbines will be required to operate in more diverse environmental conditions with an increased energy output compared to today's wind turbines. In order to meet these demands, high resolution unsteady aerodynamic analyses, such as those from a large-eddy simulation (LES) or a detached-eddy simulation (DES), will be essential in the design process so that performance over a range of realistic operating conditions may be predicted with high accuracy. Unfortunately, such analyses are currently too computationally expensive to be effective in an industrial setting. However, there is ample room for improvement over the currently widely-used blade element momentum (BEM) method in terms of wind turbine aerodynamic modeling.

The family of BEM methods became popular in wind turbine design due to their ease of implementation and cheap computational cost. These models rely on existing airfoil data, and thus, load predictions are only as accurate as the available data. Moreover, designs are restricted to airfoils for which sufficient data exists. To be effective in new blade designs, computational models must be able to predict performance without requiring an existing experimental dataset.

Steady-state solutions to the Reynolds-averaged Navier-Stokes (RANS) equations offer a significant improvement in aerodynamic modeling at a reasonable computational cost, but wind turbine flows are inherently unsteady. Even if the unsteadiness due to the rotation of the rotor is eliminated with a relative coordinate system, which is only possible for orthogonal inflow, the vibrations of the turbine blades add additional unsteadiness. Time accurate unsteady solutions of the RANS equations are too costly to be effective, but with the harmonic balance method, there exists a way to represent unsteady, periodic flows by coupling a set of steady-state solutions. If a harmonic balance based aerodynamics model is coupled to a suitable structural dynamics model, it is possible to create an efficient aeroelastic wind turbine model driven by the unsteady RANS equations.

Aeroelastic analysis of wind turbines is an essential part of the design process to ensure that no structural vibrations, catastrophic or fatiguing, will exist in the structure over a range of operating conditions. The work in this dissertation is directed at improving current aeroelastic modeling capability by improving the aerodynamic solution via the unsteady RANS equations. The Spalart-Allmaras turbulence model and the γ–$\overline{\mathrm{Re}_{\theta t}}$ transition model are included to model critical turbulent flow features.

1.2 Related Work

This section presents related work in wind turbine aerodynamics, including transition modeling and the harmonic balance method. Wind turbine aeroelastic modeling and known instabilities are also presented. Two popular wind turbine aeroelastic models from industry are briefly described, and finally, work related to flutter predictions for wind turbine blades is provided.

1.2.1 Wind Turbine Aerodynamics

Traditionally, wind turbines were designed using blade element momentum (BEM) theory with corrections for dynamic wake, stall, or inflow to predict aerodynamic loads acting on turbine blades [31]. In the steady BEM method, momentum theory is combined with the blade element method to predict loads on turbine blades for constant wind speeds, rotational speeds, or pitch angles. In momentum theory, a streamtube enclosing an actuator disc is considered as in Fig. 1.1. The ambient conditions upstream, p_∞ and U_∞, are known. The actuator disc represents the rotor where the incoming wind is slowed down by some amount, U_d. There is also a step change in pressure at the disc corresponding to the thrust exerted by the wind on the rotor. Due to the decreasing velocity, the streamlines must diverge as they cross the actuator disc moving downstream. The pressure returns to the ambient value far downstream, but the velocity in the wake, U_w, is slightly less than the free stream. Under these conditions, it is possible to relate the free stream velocity, velocity at the rotor, velocity downstream, thrust, and absorbed power. In blade element theory, the aerodynamic forces acting on a blade are determined at sections along a blade rather than the entire blade.

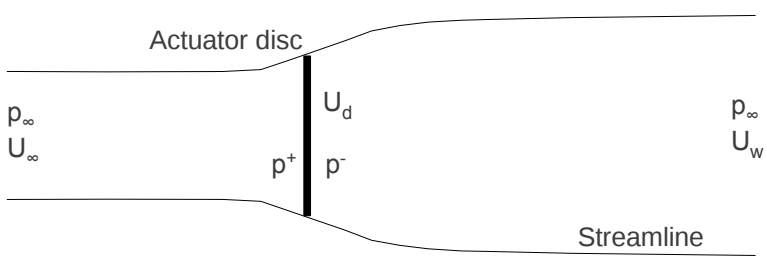

Figure 1.1: Streamtube around an actuator disc representing a 1-D model of a wind turbine rotor.

Glauert [27] combined momentum theory and blade element theory to model flow over airplane propellers. He considered the flow in annuli around the rotor. The forces and induced velocity in each annulus were found using blade element and momentum

theories. Glauert assumed that there was no radial dependency between elements and that the force in each annulus was constant. The second assumption implies an infinite number of blades. Prandtl's tip loss factor is used to correct this assumption so that a finite number of blades may be represented.

To account for unsteadiness in the flow, a number of corrections must be applied to the steady BEM method. The unsteadiness of the incoming wind is included using a dynamic inflow model. There are a number of models available for this purpose [58, 64]. Additionally, a non-stationary airfoil will have different stall characteristics than a stationary one. The forces on an airfoil change dramatically once stall occurs so some representation of this phenomenon should be included. A popular choice here is the Beddoes-Leishman model [46]. Other possible corrections include yaw/tilt for non-orthogonal inflow and a turbulent wake for high loading.

BEM methods are limited in that existing airfoil data is required as an input. Navier-Stokes solvers overcome this limitation, but they come with a much higher computational cost. Steady solutions remain practical, but time-accurate unsteady solutions are still prohibitively costly. Despite the limitations for industrial design, a growing number of Navier-Stokes solvers have appeared in the literature in the past decade as the available computational power has increased. Le Pape and Lecanu [43] used ONERA's compressible flow solver elsA to create a 3-D simulation of a stall-regulated wind turbine. They achieve some success with their model but cite the need for low speed preconditioning and a boundary layer transition model for better results. Tongchitpakdee et al. [86] modeled several upwind cases from the National Renewable Energy Laboratory's (NREL) Phase VI rotor. They report success for attached flow and massively separated flows. In the partially separated regime, their solver does not perform as well. They use Eppler's transition model to improve results in this area.

Transition Modeling

One challenge that comes with Navier-Stokes solvers is accurately modeling more of the flow physics. Wind turbines operate in a flow regime where boundary layer transition from laminar to turbulent flow has a major impact on the solution. In unsteady RANS solvers, the success of the model seems to depend largely on the ability of the turbulence model to predict the location of the laminar separation bubble and turbulent reattachment during stall [40]. Many turbulence models assume fully turbulent flow everywhere including inside the boundary layer unless a location is defined by the user to trip the boundary layer. However, in that approach, the location must be known *a priori* making it less appealing for design. A transition model is necessary to predict the location and extent of the boundary layer transition.

One of the most successful transition models for airfoils is the e^n method of Smith and Gamberoni [73] and van Ingren [94]. This method uses linear stability theory and assumes a parallel flow to compute the growth of disturbance waves. However, some knowledge of the flow is required as an input to the model, and the prediction of flow reattachment is not possible. Moreover, disturbances are tracked along streamlines, which can be very challenging in 3-D codes where the grid and streamsurfaces are not aligned. Empirically-based transition models gained popularity due to their success in matching experimental data. In these models, the momentum thickness Reynolds number based on a laminar solution is computed along the surface, and transition is said to occur when the momentum thickness Reynolds number in the turbulent solution exceeds the laminar value. Two of the more widely known transition models are attributed to Mayle [52] and Abu-Ghannam and Shaw [1].

Computation of the momentum thickness Reynolds number is not ideal since the edge of the boundary layer may not be well-defined, and search algorithms to find the edge of the boundary layer are too complex in the age of unstructured grids and parallel computing. This problem can be avoided if a correlation based on local flow variables is developed. The γ–$\overline{\mathrm{Re}_{\theta t}}$ transition model of Langtry [39] offers this

advantage. This model was developed for use with the k-ω SST turbulence model, and it includes an intermittency transport equation to slowly increase turbulence in the boundary layer from the onset location. A modified version of this transition model for use with the Spalart-Allmaras turbulence model has recently been developed by Medida and Baeder [54]. This implementation has the advantage of solving one less equation since the Spalart-Allmaras turbulence model is a one equation model compared to the two equation k-ω SST model.

Harmonic Balance Method

Many flow characteristics about wind turbines are periodic, making their aerodynamic analysis ideally suited for frequency domain techniques such as the harmonic balance method. The generalized harmonic balance method put forward by Hall et al. [30] for the analysis of nonlinear unsteady flows in turbomachinery is a mixed time domain/frequency domain technique that computes the dependent flow variables at equally spaced sub-time levels over a single period. Through the use of a pseudo-spectral operator, the problem can be simplified to a set of coupled steady-state problems where convergence acceleration techniques such as local time stepping, residual smoothing, and multigrid can be employed to greatly reduce the computational cost in comparison to unsteady methods in the temporal domain [25, 23].

Using the harmonic balance method, it is possible to perform unsteady analyses in wind turbine blade design at a cost that is only approximately 5-10 times the cost of a steady Navier-Stokes analysis. Despite these potential savings, application of the harmonic balance method to wind turbines has been very limited. Campobasso and Baba-Ahmadi [15] developed a compressible harmonic balance solver with low speed preconditioning necessary for modeling low Mach number regimes typical for wind turbines. In their work, they applied the technique to a NACA 0012 airfoil section. Extension of their solver to wind turbine type airfoils would require an additional step

since the thicker airfoils require transition modeling to correctly predict the near-stall flow regime.

1.2.2 Wind Turbine Aeroelasticity

Aeroelasticity is the study of the interaction of aerodynamic, inertial, and elastic forces [9]. Consider air passing over a wind turbine blade where the aerodynamic force of the air on the blade causes a small elastic deformation of the blade. The elastic deformation of the blade changes the orientation of the blade in the air stream, which, in turn, changes the aerodynamic force on the blade. The interactions will either reach a new equilibrium state or diverge catastophically resulting in structural failure. The inertial force plays a role in the interaction between the aerodynamic and elastic forces predominantly through mass distribution.

Elastic structures will vibrate in discrete geometric patterns known as mode shapes in response to periodic external forces. Each mode shape has a corresponding frequency at which the vibration will occur. If undamped, these vibrations have the potential to grow exponentially or interact with other vibrations containing a multiple of this frequency. Wind turbine designers use aeroelastic analyses to ensure that these vibrations are damped so that the stucture is safe and fatigue loads are minimized. Thus, the aeroelastic design of wind turbines is concerned with maximizing the damping of the system components and keeping the modal frequencies of the system components separated. Of particular importance are the blade and tower natural frequencies, which should be kept apart from each other. Multiples of the rotational frequency should also be avoided.

Wind turbine aeroelasticity is closely related to helicopter aeroelasticity. Exhaustive reviews of potential aeroelastic instabilities have been conducted by Pavel and Schoones [61], van Holten et al. [93], and Holierhoek [33]. A few of the instabilities associated with the blades and the coupling between the rotor and the tower are given in the following sections.

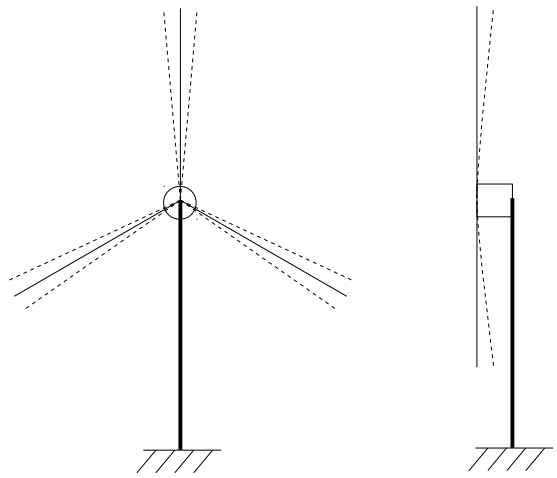

(a) Edgewise **(b)** Flapwise

Figure 1.2: In-plane and out-of-plane blade deflections.

Blade Instabilities

Two single degrees-of-freedom (DOF) instabilities associated with turbine blades are edgewise and flapwise instability. The names are derived from the associated blade deflections, which are shown in Fig. 1.2. Edgewise deflections refer to blade displacements in the rotor plane. Flapwise deflections refer to blade displacements normal to the rotor plane. Note that there is some simplification in this description as deflections are usually defined with respect to the local chord, which twists considerably from blade root to tip. True edgewise deflections, for example, are not purely in the rotor plane but contain a small component normal to the rotor plane. Edgewise deflections are a result of the tangential force on the blade responsible for creating torque to turn the rotor. Flapwise deflections are due to the thrust created by the pressure jump as the wind crosses the rotor plane.

Stall regulated wind turbines are known to suffer from edgewise blade vibration instability. The problem emerged as wind turbines began to increase in size. Stiesdal reported edgewise vibrations on a 37 meter diameter rotor in 1994 [77]. The Aerpac APX40T is a 600 kW, 43 meter diameter wind turbine that was subject to edgewise

vibrations in high wind speeds [4]. The reason for the instability was explained by Petersen et al. [63]. For a blade translating harmonically in the rotor plane (or a plane near the rotor plane), the aerodynamic damping is negative or unstable at low and high wind speeds. Given this result, it should be expected that this instability is always present. However, due to the local orientation of the blade, the vibration is typically never totally in the rotor plane. There is some component in the flapwise direction, which has very good damping characteristics. The edgewise instability can be controlled by designing blades to vibrate more in the flapwise direction so that the edgewise vibrations are effectively damped.

Flapwise blade vibration instability has been observed, for example, on the Nibe A turbine operating in stall [49]. However, the analysis of Petersen el at. [63] shows that flapwise vibrations are well damped except at very high wind speeds. This instability is of little concern in modern wind turbines, which are typically pitch regulated.

Other couplings of single DOF blade instabilities have been investigated. Chaviaropoulos [18] studied the coupling of the flapwise and edgewise instabilities. Here, the edgewise instability is referred to as lead-lag instability, which refers to the blade deflection leading or lagging in the rotor plane. Although the model in this case is highly simplified, some general trends reported are more stability with thicker airfoils or minimal structural damping.

Flutter

Flutter is a common instability in turbomachinery and fixed-wing aircraft, but it has never been a problem with commercial wind turbines [31]. In fixed-wing aircraft, flutter results from the torsional DOF coupling with a translational DOF, usually a flapwise mode. To better understand flutter, consider a wing rigidly attached at the root. Due to the elastic properties of the wing material, it has freedom to bend and twist as a cantilever beam. The wing also has freedom in other directions, but they are not important here. Any small disturbance to the wing structure will cause the wing to oscillate in these directions. Without any sustained source of perturbation,

the oscillations will eventually be damped. As the wing encounters increasing wind speeds, the dampening will at first increase before beginning to decrease. When the flutter speed is encountered, the oscillations can just maintain themselves. Above the flutter speed, the oscillations can become violent and destructive to the wing structure [26]. In terms of damping, when the sum of the aerodynamic and structural damping is zero, this corresponds to a neutrally stable solution known as flutter. If the damping becomes negative, the system is unstable. Thus, it is critical to understand the flutter onset point in aeroelastic structures since any small disturbance above this condition has the potential to be catastrophic.

There is concern that flutter might emerge with larger wind turbines as the torsional frequency decreases with increased stuctural flexibility. Lobitz performed a flutter analysis on the WindPACT 1.5 MW turbine blade and found that the flutter did not occur until about twice the max operating speed of the rotor [48]. The Wind Energy Technologies Department at Sandia National Laboratories has continued to investigate flutter in large wind turbines building off of his initial work [67, 57]. Vatne [97] analyzed the NOWITECH reference turbine using HAWC2 (see below for description of HAWC2). He also found flutter for this 10 MW, 140 m diameter rotor near double the max operational speed [97]. Larwood investigated flutter onset and alleviation in straight and swept wind turbine blades [42]. One of the findings of this work was the importance in moving the blade center of mass forward of the elastic axis to increase the flutter speed.

Coupled Rotor/Tower Instabilities

Aeroelastic analysis of a single turbine blade is typically insufficient since it is possible for the vibrations of other system components, e.g. tower, nacelle, etc., to couple with blade vibrations through the structural connections. It is possible for the edgewise blade vibrations to couple with various tower modes of vibration. Van Holten et al. [93] found several instances in the literature of edgewise blade vibration coupling with the translational modes of the tower. A slightly different version of this instability is

a coupling of the advancing lead/lag mode with either the first tower torsion mode or second tower bending mode. A famous example of this instability occurred on the KEWT (Kosten Effectieve Wind Turbine) prototype in the 1980s where the first tower torsion mode and lead/lag mode coupled when the angular velocity of the rotor was half the frequency of first tower torsion mode. A second instability occurred when the angular velocity was half the frequency of the second tower bending mode [61, 62].

Aeroelastic Models

The dominant aeroelastic models in industry currently are RISØ's HAWC2 [41] and the National Renewable Energy Laboratory's (NREL) Fatigue, Aerodynamics, Structures, and Turbulence (FAST) [38]. HAWC2 is a standard analysis tool developed and maintained by the RISØ National Laboratory in Denmark. The structural dynamics are modeled using a multibody formulation applied to Timoshenko beam elements. The multibody approach allows for larger deformations to more accurately model new, larger wind turbines. Aerodynamics are modeled using the BEM method with corrections for dynamic stall, dynamic wake, skewed inflow, and tip losses.

FAST employs a combined multibody and mode shape formulation where the blades and tower are modeled via mode shapes and the platform, nacelle, generator, gears, hub, and tail are modeled via the multibody formulation. Aerodynamics in FAST are also modeled with the BEM method with corrections as in HAWC2. HAWC2 and FAST have both recently added capabilities to model offshore wind turbines where there is an added complexity due to the interaction of the ocean and sea floor with the support structure.

1.3 Contributions to State of the Art

The primary objective of this dissertation is to develop a wind turbine aeroelastic model by coupling an unsteady Reynolds-averaged Navier-Stokes flow solver and a

mode shape-based structural dynamics model. Utilization of the harmonic balance method to model the unsteady flow behavior will keep the computational workload favorable for use in a design setting. The presented aeroelastic model offers significant improvement in the aerodynamics modeling capability over current aeroelastic models based on the blade element momentum approach. Not only will this be the first wind turbine aeroelastic model to utilize the harmonic balance method, this work will also include the first use of the γ–$\overline{\mathrm{Re}_{\theta t}}$ transition model to analyze unsteady wind turbine aerodynamics via the harmonic balance method.

The specific contributions of this work are worth noting. The author converted an in-house 2-D turbomachinery CFD code into a 3-D external CFD code. New far field boundary conditions and periodic boundary conditions were added in the process. The discretization was changed from vertex-based to cell-centered, and Roe fluxes with MUSCL were also added. The original solver was designed for H-O-H type meshes in turbomachinery, but the topology was converted to C-type meshes for 2-D simulations and C-H-type meshes for 3-D simulations. The implicit LU-SGS time integration scheme was added to the solver as was the γ–$\overline{\mathrm{Re}_{\theta t}}$ transition model and the harmonic balance method. Parallel computing capability was added to the code via the OpenMPI framework. The governing aeroelastic equation in the frequency domain was derived from the general form of the structural dynamics equation since no form existed previously for wind turbine blade flutter.

1.4 Outline

The structure of the dissertation is as follows. The governing equations for the aerodynamic and structural dynamic models are presented in the next chapter. Chapter 3 details the numerical techniques employed to solve the governing flow equations, and Chapter 4 details the flutter solution technique. Validation results for the flow solver and aeroelastic model are provided in Chapter 5. Chapter 6 compares results between fully turbulent and boundary layer transition solutions for a pitching

S809 airfoil, and Chapter 7 investigates flutter of the 1.5 MW WindPACT turbine blade. The dissertation closes with a summary and discussion of potential future work in Chapter 8.

Chapter 2

Governing Equations

This chapter presents the governing equations for the aerodynamic and structural dynamic models used in this work. The chapter begins with the governing equations of fluid dynamics known as the Navier-Stokes equations (Section 2.1). Section 2.2 describes the Spalart-Allmaras turbulence model, which is used to set the eddy viscosity. For separated flows, it is essential to model the boundary layer transition from laminar to turbulent. For this purpose, the γ–$\overline{\mathrm{Re}_{\theta t}}$ transition model is used, which is described in Section 2.3. The chapter closes with the harmonic balance equations in Section 2.4 and the governing structural dynamics equation in Section 2.5.

2.1 Navier-Stokes Equations

The Navier-Stokes equations are derived from the conservation of mass, momentum, and energy. When viscosity is neglected, the well-known Euler equations result. The details of the derivation are readily available in textbooks and omitted here. The interested reader may find an excellent discussion of the derivation in Hirsch [32]. In integral form, the Navier-Stokes equations are written

$$\frac{\partial}{\partial t}\int_{\mathcal{V}} \rho \, d\mathcal{V} + \oint_{S} \rho \boldsymbol{v} \cdot d\boldsymbol{S} = 0 \tag{2.1}$$

$$\frac{\partial}{\partial t}\int_{\mathcal{V}} \rho \boldsymbol{v}\, d\mathcal{V} + \oint_S \rho \boldsymbol{v}(\boldsymbol{v}\cdot d\boldsymbol{S}) = \int_{\mathcal{V}} \rho \boldsymbol{f_e}\, d\mathcal{V} - \oint_S p d\boldsymbol{S} + \oint_S \bar{\bar{\tau}}\cdot d\boldsymbol{S} \tag{2.2}$$

$$\frac{\partial}{\partial t}\int_{\mathcal{V}} \rho E\, d\mathcal{V} + \oint_S \rho E(\boldsymbol{v}\cdot d\boldsymbol{S}) = \oint_S k\nabla T\cdot d\boldsymbol{S} + \int_{\mathcal{V}} (\rho \boldsymbol{f_e}\cdot\boldsymbol{v} + q_H)\, d\mathcal{V} + \oint_S (\bar{\bar{\sigma}}\cdot\boldsymbol{v})\cdot d\boldsymbol{S} \tag{2.3}$$

The Navier-Stokes equations define the time rate change of the conservation variables in terms of convective and diffusive fluxes. The convective flux is due to the bulk motion of the fluid, and the diffusive flux is due to molecular agitation. Thus, a diffusive flux is possible in a fluid at rest, but a convective flux is not. The Navier-Stokes equations may be written in strong conservation form according to

$$\frac{\partial \boldsymbol{U}}{\partial t} + \frac{\partial \boldsymbol{F}}{\partial x} + \frac{\partial \boldsymbol{G}}{\partial y} + \frac{\partial \boldsymbol{H}}{\partial z} = \boldsymbol{S} \tag{2.4}$$

where the vector of conservation variables, $\boldsymbol{U}$, and the flux vectors $\boldsymbol{F}$, $\boldsymbol{G}$, and $\boldsymbol{H}$ and source vector $\boldsymbol{S}$ are given by

$$\boldsymbol{U} = \begin{bmatrix} \rho \\ \rho u \\ \rho v \\ \rho w \\ \rho E \end{bmatrix} \quad ; \quad \boldsymbol{F} = \begin{bmatrix} \rho u - \rho \dot{f} \\ \rho u^2 + p - \tau_{xx} - \rho u \dot{f} \\ \rho uv - \tau_{xy} - \rho v \dot{f} \\ \rho uw - \tau_{xz} - \rho w \dot{f} \\ \rho uh - \tau_{xh} - \rho E \dot{f} \end{bmatrix} \tag{2.5}$$

$$\boldsymbol{G} = \begin{bmatrix} \rho v - \rho \dot{g} \\ \rho uv - \tau_{yx} - \rho u \dot{g} \\ \rho v^2 + p - \tau_{yy} - \rho v \dot{g} \\ \rho vw - \tau_{yz} - \rho w \dot{g} \\ \rho vh - \tau_{yh} - \rho E \dot{g} \end{bmatrix} \quad ; \quad \boldsymbol{H} = \begin{bmatrix} \rho w - \rho \dot{h} \\ \rho uw - \tau_{zx} - \rho u \dot{h} \\ \rho vw - \tau_{zy} - \rho v \dot{h} \\ \rho w^2 + p - \tau_{zz} - \rho w \dot{h} \\ \rho wh - \tau_{zh} - \rho E \dot{h} \end{bmatrix} \quad ; \quad \boldsymbol{S} = \begin{bmatrix} 0 \\ 0 \\ 0 \\ 0 \\ 0 \end{bmatrix} \tag{2.6}$$

The source vector $\boldsymbol{S}$ is zero in the absence of body forces such as gravity or buoyancy. The shear stresses and pressure are defined in the coming sections. The $\dot{f}$, $\dot{g}$, and $\dot{h}$ terms are added as the x, y, and z components of the unsteady grid motion velocity, respectively.

2.1.1 Viscous Stresses

The most general form of the viscous stress tensor includes the dynamic viscosity, μ, and a second viscosity coefficient, λ. Stokes [78] hypothesized the two were related according to

$$2\mu + 3\lambda = 0 \tag{2.7}$$

In a Newtonian fluid, the shear stress is proportional to the velocity gradient. Using this assumption with the Stokes hypothesis, the viscous shear stresses may be written [69, 100]

$$\tau_{ij} = \mu \left[\left(\frac{\partial v_j}{\partial x_i} + \frac{\partial v_i}{\partial x_j} \right) - \frac{2}{3} (\boldsymbol{\nabla} \cdot \boldsymbol{v}) \delta_{ij} \right] \tag{2.8}$$

Thus, the shear stress terms in the x-direction are given by

$$\tau_{xx} = (\mu_l + \mu_t) \left[\frac{4}{3} \frac{\partial u}{\partial x} - \frac{2}{3} \left(\frac{\partial v}{\partial y} + \frac{\partial w}{\partial z} \right) \right] \tag{2.9}$$

$$\tau_{xy} = (\mu_l + \mu_t) \left(\frac{\partial u}{\partial y} + \frac{\partial v}{\partial x} \right) \tag{2.10}$$

$$\tau_{xz} = (\mu_l + \mu_t) \left(\frac{\partial u}{\partial z} + \frac{\partial w}{\partial x} \right) \tag{2.11}$$

$$\tau_{xh} = u\tau_{xx} + v\tau_{xy} + w\tau_{xz} + \left(\frac{\mu_l}{Pr_l} + \frac{\mu_t}{Pr_t} \right) \frac{\partial h}{\partial x} \tag{2.12}$$

Similar terms define the shear stress terms in the y- and z-directions. The viscosity is broken into two components in the shear stress terms, μ_l and μ_t. The laminar viscosity, μ_l, is a fluid property determined with the Sutherland formula. The latter is the eddy viscosity, and it is computed by a suitable turbulence model such as the Spalart-Allmaras [75] or $k - \omega$ SST [55] model.

2.1.2 Perfect Gas Model

The Navier-Stokes equations are composed of five equations with seven unknown flow variables: ρ, u, v, w, E, p, and T. It can be shown using the ideal gas assumption

that the pressure can be related to the conservation variables through

$$p = (\gamma - 1)\rho \left[E - \frac{1}{2}\left(u^2 + v^2 + w^2\right) \right] \tag{2.13}$$

The temperature can be computed using

$$p = \rho R_{gas} T \tag{2.14}$$

2.1.3 Rotating Frame of Reference

It is convenient to use the Navier-Stokes equations in a rotating frame of reference when the computational domain is steadily rotating about some axis such as in turbomachinery, helicopter rotors, or wind turbines. This allows an unsteady flow in an inertial frame of reference to be considered as a steady flow in a rotating frame of reference.

Following the development by Agarwal and Deese [2, 3], the Navier-Stokes equations may be recast in a rotating reference frame using absolute velocity components. Letting (u, v, w), (u_r, v_r, w_r), and $(u_\Omega, v_\Omega, w_\Omega)$ denote the absolute, relative, and rotational velocity components, the velocity components are related according to

$$u = u_r - u_\Omega \ ; \quad v = v_r - v_\Omega \ ; \quad w = w_r - w_\Omega \tag{2.15}$$

where Ω is angular velocity of the rotor. For a rotation about the y-axis, the rotational velocity components are given by

$$u_\Omega = -\Omega z \ ; \quad v_\Omega = 0 \ ; \quad w_\Omega = \Omega x \tag{2.16}$$

Considering the Euler equations only, the governing equations in relative velocity components are written

$$\frac{\partial \boldsymbol{U}_r}{\partial t} + \frac{\partial \boldsymbol{F}_r}{\partial x} + \frac{\partial \boldsymbol{G}_r}{\partial y} + \frac{\partial \boldsymbol{H}_r}{\partial z} = \boldsymbol{S}_r \tag{2.17}$$

where now the conservation variables, flux vectors, and source terms are given by

$$\boldsymbol{U}_r = \begin{bmatrix} \rho \\ \rho u_r \\ \rho v_r \\ \rho w_r \\ \rho E_r \end{bmatrix} \quad ; \quad \boldsymbol{F}_r = \begin{bmatrix} \rho u_r \\ \rho {u_r}^2 + p \\ \rho u_r v_r \\ \rho u_r w_r \\ \rho u_r I \end{bmatrix} \tag{2.18}$$

$$\boldsymbol{G}_r = \begin{bmatrix} \rho v_r \\ \rho u_r v_r \\ \rho {v_r}^2 + p \\ \rho v_r w_r \\ \rho v_r I \end{bmatrix} \quad ; \quad \boldsymbol{H}_r = \begin{bmatrix} \rho w_r \\ \rho u_r w_r \\ \rho v_r w_r \\ \rho {w_r}^2 + p \\ \rho w_r I \end{bmatrix} \quad ; \quad \boldsymbol{S}_r = \begin{bmatrix} 0 \\ \rho \Omega^2 x - 2\rho\Omega w_r \\ 0 \\ \rho \Omega^2 z + 2\rho\Omega u_r \\ 0 \end{bmatrix} \tag{2.19}$$

and the total relative enthalpy and the total rothalpy are defined as

$$E_r = \frac{p}{(\gamma - 1)\rho} + \frac{1}{2}\left(u_r^2 + v_r^2 + w_r^2\right) - \frac{1}{2}\left(u_\Omega^2 + w_\Omega^2\right) \tag{2.20}$$

$$I = E_r + \frac{p}{\rho} \tag{2.21}$$

The rothalpy represents the total energy in a steadily rotating frame of reference. The source vector in this variable set is augmented by the Coriolis and centrifugal force terms. The governing equations can be converted back to absolute variables using the relations in Eq. 2.15. The conservation variables, flux vectors, and source term then become

$$\boldsymbol{U} = \begin{bmatrix} \rho \\ \rho u \\ \rho v \\ \rho w \\ \rho E \end{bmatrix} \quad ; \quad \boldsymbol{F} = \begin{bmatrix} \rho u + \rho u_\Omega \\ \rho u^2 + p + \rho u u_\Omega \\ \rho u v + \rho v u_\Omega \\ \rho u w + \rho w u_\Omega \\ \rho u h + \rho e u_\Omega \end{bmatrix} \tag{2.22}$$

$$\boldsymbol{G} = \begin{bmatrix} \rho v \\ \rho uv \\ \rho v^2 + p \\ \rho vw \\ \rho vh \end{bmatrix} \quad ; \quad \boldsymbol{H} = \begin{bmatrix} \rho w + \rho w_\Omega \\ \rho uw + \rho uw_\Omega \\ \rho vw + \rho vw_\Omega \\ \rho w^2 + p + \rho ww_\Omega \\ \rho wh + \rho ew_\Omega \end{bmatrix} \quad ; \quad \boldsymbol{S} = \begin{bmatrix} 0 \\ -\rho\Omega w \\ 0 \\ \rho\Omega u \\ 0 \end{bmatrix} \tag{2.23}$$

Note that for zero angular velocity, the inertial frame of reference is recovered. The viscous fluxes keep the same form from the inertial frame of reference.

2.2 Spalart-Allmaras Turbulence Model

The turbulent fluctuations are neglected when solving the Reynolds-averaged Navier-Stokes equations, but in order to model turbulent flows accurately, the effects of turbulence must be included in some way. One method is to use the Boussinesq hypothesis [12, 13] that the turbulent shear stress is linearly proportional to the mean strain rate. The constant of proportionality is known as the eddy viscosity. With this approach, the effects of turbulence can be included by adding an eddy viscosity term, μ_t, to the laminar viscosity, μ_l.

The Spalart-Allmaras [75] turbulence model is a popular and effective turbulence model utilizing this approach. The model was developed empirically and performs well over airfoils and in adverse pressure gradients. Keeping the form of Eq. 2.4, the flux vectors for the Spalart-Allmaras model can be written as

$$\boldsymbol{U} = \left[\rho\tilde{\nu}\right] \quad ; \quad \boldsymbol{F} = \left[\rho u\tilde{\nu} - \tau_{x\nu} - \rho\tilde{\nu}\dot{f}\right] \tag{2.24}$$

$$\boldsymbol{G} = \left[\rho v\tilde{\nu} - \tau_{y\nu} - \rho\tilde{\nu}\dot{g}\right] \quad ; \quad \boldsymbol{H} = \left[\rho w\tilde{\nu} - \tau_{z\nu} - \rho\tilde{\nu}\dot{h}\right] \quad ; \quad \boldsymbol{S} = \left[S_t\right] \tag{2.25}$$

where the shear stress term in the x-direction, for example, is given by

$$\tau_{x\tilde{\nu}} = \frac{1}{\sigma}\left(\mu_l + \rho\tilde{\nu}\right)\frac{\partial\tilde{\nu}}{\partial x} \tag{2.26}$$

The eddy viscosity is found using

$$\mu_t = \rho\tilde{\nu} f_{v1} \tag{2.27}$$

The source term is composed of a production, destruction, and diffusion term. Written in this order, the source term takes the form

$$\begin{aligned} S_t = c_{b1}\left(1 - f_{t2}\right)\tilde{S}\rho\tilde{\nu} - \\ \rho\left[c_{w1}f_w - \frac{c_{b1}}{\kappa^2}f_{t2}\right]\left(\frac{\tilde{\nu}}{d}\right)^2 + \frac{\rho c_{b2}}{\sigma}\left[\left(\frac{\partial\tilde{\nu}}{\partial x}\right)^2 + \left(\frac{\partial\tilde{\nu}}{\partial y}\right)^2 + \left(\frac{\partial\tilde{\nu}}{\partial z}\right)^2\right] \end{aligned} \tag{2.28}$$

The various terms and constants appearing in these equations are defined as

$$f_{v1} = \frac{\chi^3}{\chi^3 + c_{v1}^3} \ ; \quad \chi = \frac{\rho\tilde{\nu}}{\mu_l} \tag{2.29}$$

$$\tilde{S} = \Omega + \frac{\tilde{\nu}}{\kappa^2 d^2} f_{v2} \ ; \quad f_{v2} = 1 - \frac{\chi}{1 + \chi f_{v1}} \tag{2.30}$$

$$f_w = g\left(\frac{1 + c_{w3}^6}{g^6 + c_{w3}^6}\right)^{1/6} \ ; \quad g = r + c_{w2}\left(r^6 - r\right) \tag{2.31}$$

$$r = \min\left(\frac{\tilde{\nu}}{\tilde{\mathrm{S}}\kappa^2\mathrm{d}^2}, 10\right) \ ; \quad \mathrm{f_{t2}} = \mathrm{c_{t3}}\mathrm{e}^{-\mathrm{c_{t4}}\chi^2} \tag{2.32}$$

where Ω is the vorticity magnitude.

Notice the ease with which the Spalart-Allmaras turbulence model may be added to a RANS solver since only the laminar viscosity in the mass, momentum, and energy equations needs to be augmented by the eddy viscosity. Additionally, the added computational workload is reasonable since only one more transport equation is solved.

2.3 Transition Model

The Spalart-Allmaras turbulence model as just described assumes fully turbulent flow everywhere. This assumption is not valid for wind turbine flows where the boundary layer is initially laminar before becoming turbulent some distance downstream. It is possible to set a trip location along the airfoil surface, but doing so requires knowledge of the location *a priori* so this is a very limited solution. A better approach is to use a transition model that is able to predict the laminar to turbulent transition in the boundary layer using local flow quantities.

The $\gamma - \overline{\mathrm{Re}_{\theta t}}$ transition model developed by Langtry [39] works very well with the k-ω SST turbulence model. Recently, the model was adapted for the Spalart-Allmaras turbulence by Medida and Baeder [54]. In strong conservation form, the flux vectors for this model are given by

$$\boldsymbol{U} = \begin{bmatrix} \rho\gamma \\ \rho\overline{\mathrm{Re}_{\theta t}} \end{bmatrix} \quad ; \quad \boldsymbol{F} = \begin{bmatrix} \rho u\gamma - \tau_{x\gamma} - \rho\gamma\dot{f} \\ \rho u\overline{\mathrm{Re}_{\theta t}} - \tau_{xr} - \rho\overline{\mathrm{Re}_{\theta t}}\dot{f} \end{bmatrix} \tag{2.33}$$

$$\boldsymbol{G} = \begin{bmatrix} \rho v\gamma - \tau_{y\gamma} - \rho\gamma\dot{g} \\ \rho v\overline{\mathrm{Re}_{\theta t}} - \tau_{yr} - \rho\overline{\mathrm{Re}_{\theta t}}\dot{g} \end{bmatrix} \quad ; \quad \boldsymbol{H} = \begin{bmatrix} \rho w\gamma - \tau_{z\gamma} - \rho\gamma\dot{h} \\ \rho w\overline{\mathrm{Re}_{\theta t}} - \tau_{zr} - \rho\overline{\mathrm{Re}_{\theta t}}\dot{h} \end{bmatrix} \tag{2.34}$$

$$\boldsymbol{S} = \begin{bmatrix} S_\gamma \\ S_{\overline{\mathrm{Re}_{\theta t}}} \end{bmatrix} \tag{2.35}$$

The transition model contains two equations. The first equation solves for the intermittency, γ, which adjusts the production and destruction source terms in the Spalart-Allmaras model. The intermittency takes on values between 0 and 1 where 0 corresponds to laminar flow and 1 to fully turbulent flow. The source term for the intermittency equation is given as

$$S_\gamma = P_\gamma - D_\gamma + \rho\gamma\left(\frac{\partial u}{\partial x} + \frac{\partial v}{\partial y}\right) \tag{2.36}$$

where P_γ and D_γ are the intermittency production and destruction terms, respectively. These are defined as

$$P_\gamma = F_{\text{length}} c_{a1} \rho S \left(\gamma F_{\text{onset}}\right)^{0.5} \left(1.0 - c_{e1}\gamma\right) \tag{2.37}$$

$$D_\gamma = c_{a2} \rho \Omega \gamma F_{\text{turb}} \left(c_{e2}\gamma - 1.0\right) \tag{2.38}$$

with input parameters given by

$$F_{\text{onset}} = \max\left(F_{\text{onset2}} - F_{\text{onset3}}, 0.0\right) \tag{2.39}$$

$$F_{\text{onset1}} = \frac{\text{Re}_\nu}{2.193\text{Re}_{\theta c}} \tag{2.40}$$

$$F_{\text{onset2}} = \min\left(\max\left(F_{\text{onset1}}, F_{\text{onset1}}^4\right), 2.0\right) \tag{2.41}$$

$$F_{\text{onset3}} = \max\left(1.0 - \left(\frac{R_T}{2.5}\right)^3, 0.0\right) \tag{2.42}$$

$$F_{\text{turb}} = e^{-\left(\frac{R_T}{4}\right)^4} \tag{2.43}$$

$$\text{Re}_\nu = \frac{\rho d^2 S}{\mu_l}; \quad R_T = \frac{\mu_t}{\mu_l} \tag{2.44}$$

The calibration used by Medida and Baeder [54] is kept, which seems to be appropriate for airfoil problems with freestream turbulence intensities much less than 1.0%. These correlations define the critical Reynolds number, $\text{Re}_{\theta c}$, and the transition length function, F_{length}, as

$$\text{Re}_{\theta c} = \left(4.45Tu_\infty^3 - 5.7Tu_\infty^2 + 1.37Tu_\infty + 0.585\right)\overline{\text{Re}_{\theta t}} \tag{2.45}$$

$$F_{\text{length}} = 0.171Tu_\infty^2 - 0.0083Tu_\infty + 0.0306 \tag{2.46}$$

The second transport equation solves for the momentum thickness Reynolds number, $\overline{\text{Re}_{\theta t}}$, which is used to determine the location and extent of the transition from laminar to turbulent flow. Since the turbulence intensity varies inside the domain, the freestream value of the momentum thickness Reynolds number is

inappropriate. Instead, the momentum thickness transport equation is used to transport the freestream turbulence effects into the boundary layer. The source term for the momentum thickness Reynolds number is given by

$$S_{\overline{\mathrm{Re}_{\theta t}}} = P_{\theta t} + \rho \overline{\mathrm{Re}_{\theta t}} \left(\frac{\partial u}{\partial x} + \frac{\partial v}{\partial y} \right) \tag{2.47}$$

with the production term, $P_{\theta t}$, defined as

$$P_{\theta t} = c_{\theta t} \frac{\rho}{t_{\mathrm{scale}}} \left(\mathrm{Re}_{\theta t} - \overline{\mathrm{Re}_{\theta t}} \right) \left(1.0 - F_{\theta t} \right) \tag{2.48}$$

with input parameters given by

$$F_{\theta t} = \min \left(\max \left(F_{\mathrm{wake}} e^{-\left(\frac{d}{\delta}\right)^4}, 1.0 - \left(\frac{\gamma - 1/c_{e2}}{1.0 - 1/c_{e2}} \right)^2 \right), 1.0 \right) \tag{2.49}$$

$$\delta = \frac{50 \Omega d}{U} \delta_{BL}; \quad \delta_{BL} = 7.5 \theta_{BL}; \quad \theta_{BL} = \frac{\overline{\mathrm{Re}_{\theta t}} \mu_l}{\rho U} \tag{2.50}$$

$$F_{\mathrm{wake}} = \exp \left[\frac{\mathrm{Re}_{\omega}}{1.0 \text{ x } 10^5} \right]^2; \quad \mathrm{Re}_{\omega} = \frac{\rho \omega d^2}{\mu_l} \tag{2.51}$$

where ω is the turbulence dissipation rate. Since the dissipation rate is not known explicitly for the Spalart-Allmaras model like in the k-ω SST model, the approach of Medida and Baeder [54] is used to define these values. The local value of $\mathrm{Re}_{\theta t}$ in the production term must be found iteratively using the following experimental correlations

$$\mathrm{Re}_{\theta t} = \begin{cases} \left(1173.51 - 589.428 Tu + \frac{0.2196}{Tu^2}\right) F\left(\lambda_\theta\right) & Tu \leq 1.3 \\ 331.50 \left(Tu - 0.5658\right)^{-0.671} F\left(\lambda_\theta\right) & Tu > 1.3 \end{cases} \tag{2.52}$$

$$F\left(\lambda_\theta\right) = \begin{cases} 1.0 - \left(-12.968 \lambda_\theta - 123.66 \lambda_\theta^2 - 405.689 \lambda_\theta^3\right) e^{\left[-\left(\frac{Tu}{1.5}\right)^{1.5}\right]} & \lambda_\theta \leq 0 \\ 1.0 + 0.275 \left(1.0 - \exp\left[-35.0 \lambda_\theta\right]\right) e^{\left[-\frac{Tu}{0.5}\right]} & \lambda_\theta > 0 \end{cases} \tag{2.53}$$

which are functions of the freestream turbulence intensity, Tu, and the pressure gradient parameter, λ_θ. The pressure gradient parameter is defined

$$\lambda_\theta = \frac{\rho\theta^2}{\mu_l}\frac{dU}{ds} \tag{2.54}$$

where dU/ds is the streamwise acceleration.

To improve the prediction of transition induced by a laminar separation bubble, a second intermittency is defined as

$$\gamma_{\text{sep}} = \min\left(s_1 \max\left[0.0, \left(\frac{\text{Re}_\nu}{3.235\text{Re}_{\theta c}}\right) - 1.0\right] F_{\text{reattach}}, 2.0\right) F_{\theta_t} \tag{2.55}$$

where

$$F_{\text{reattach}} = \exp\left[-\left(\frac{R_T}{20}\right)^4\right] \tag{2.56}$$

and an effective intermittency for use in the Spalart-Allmaras equation becomes

$$\gamma_{\text{eff}} = \max\left(\gamma, \gamma_{\text{sep}}\right) \tag{2.57}$$

The transition model is coupled to the Spalart-Allmaras equation via the production and destruction terms. The modified terms are given by

$$\tilde{P}_\nu = \gamma_{\text{eff}} P_\nu; \quad \tilde{D}_\nu = \min\left(\max\left(\gamma, \beta\right), 1.0\right) D_\nu \tag{2.58}$$

Notice that the original production and destruction terms are recovered when the intermittency is equal to unity. The effect of the constant β is not fully understood yet so the recommended value for the S809 airfoil of 0.1 is used [54]. The other model constants are defined as

$$c_{e1} = 1.0; \quad c_{a1} = 2.0; \quad c_{e2} = 50.0; \quad c_{a2} = 0.06 \tag{2.59}$$

$$\sigma_f = 1.0; \quad c_{\theta_t} = 0.03; \quad \sigma_{\theta_t} = 2.0; \quad s_1 = 2.0 \tag{2.60}$$

2.4 Harmonic Balance Equations

Many flows of interest are temporally periodic, which allows one to represent the flow variables using a Fourier series in time with spatially varying coefficients. In the case of wind turbine aerodynamics, the unsteadiness may be due to vibrating or pitching blades or yawed (non-orthogonal) inflow. In such cases, the conservation variables may be expressed as a truncated Fourier series given by

$$\boldsymbol{U}(x,y,z,t_i) = \boldsymbol{A}_0(x,y,z) + \sum_{n=1}^{N} \left[\boldsymbol{A}_n(x,y,z)\cos(\omega n t_i) + \boldsymbol{B}_n(x,y,z)\sin(\omega n t_i)\right] \quad (2.61)$$

where ω is the fundamental excitation frequency, and $\boldsymbol{A}_0$, $\boldsymbol{A}_n$, and $\boldsymbol{B}_n$ are the Fourier coefficients of the conservation variables. The subscript i runs from 1 to $2N+1$. Note that the flow variables can be computed and stored at $2N+1$ equally spaced points over one temporal period. Following Eq. (2.61), the Fourier coefficients can be determined from the sub-time level solutions and vice versa with a discrete Fourier transform and inverse discrete Fourier transform given by

$$\boldsymbol{U}^* = \mathbf{E}\tilde{\boldsymbol{U}} \quad (2.62)$$

$$\tilde{\boldsymbol{U}} = \mathbf{E}^{-1}\boldsymbol{U}^* \quad (2.63)$$

where $\boldsymbol{U}^*$ are the conserved flow variables at each sub-time level, and $\tilde{\boldsymbol{U}}$ are the Fourier coefficients of the conserved flow variables. The terms $\mathbf{E}$ and $\mathbf{E}^{-1}$ are square matrices as the number of sub-time levels is equal to the number of Fourier coefficients. As an example, consider a solution with 2 harmonics or 5 sub-time levels. In this

case, Eq. 2.62 takes the form

$$\begin{bmatrix} \boldsymbol{U}_1 \\ \boldsymbol{U}_2 \\ \boldsymbol{U}_3 \\ \boldsymbol{U}_4 \\ \boldsymbol{U}_5 \end{bmatrix} = \begin{bmatrix} 1 & \cos\omega t_1 & \cos 2\omega t_1 & \sin\omega t_1 & \sin 2\omega t_1 \\ 1 & \cos\omega t_2 & \cos 2\omega t_2 & \sin\omega t_2 & \sin 2\omega t_2 \\ 1 & \cos\omega t_3 & \cos 2\omega t_3 & \sin\omega t_3 & \sin 2\omega t_3 \\ 1 & \cos\omega t_4 & \cos 2\omega t_4 & \sin\omega t_4 & \sin 2\omega t_4 \\ 1 & \cos\omega t_5 & \cos 2\omega t_5 & \sin\omega t_5 & \sin 2\omega t_5 \end{bmatrix} \begin{bmatrix} \boldsymbol{A}_0 \\ \boldsymbol{A}_1 \\ \boldsymbol{A}_2 \\ \boldsymbol{B}_1 \\ \boldsymbol{B}_2 \end{bmatrix} \tag{2.64}$$

The semi-discrete form of the governing equations can be written for all sub-time levels simultaneously, so that

$$\frac{\mathrm{d}}{\mathrm{d}t}(\mathcal{V}^*\boldsymbol{U}^*) + \boldsymbol{R}^* = 0 \tag{2.65}$$

where $\boldsymbol{R}^*$ is the residual vector evaluated at each sub-time level. The time derivative acting on the conserved variables can be expanded by using Eq. 2.62 to get

$$\frac{\partial \boldsymbol{U}^*}{\partial t} = \frac{\partial \mathbf{E}^{-1}}{\partial t}\tilde{\boldsymbol{U}} \tag{2.66}$$

The result can be further expanded using the definition for the Fourier coefficient vector to define the pseudo-spectral operator. This becomes

$$\frac{\partial \boldsymbol{U}^*}{\partial t} = \frac{\partial \mathbf{E}^{-1}}{\partial t}\mathbf{E}\boldsymbol{U}^* = \omega\mathbf{D}\boldsymbol{U}^* \tag{2.67}$$

Replacing the time derivative term in Eq. (2.65) with the pseudo-spectral operator, the harmonic balance equations are written in semi-discrete form as

$$\omega\mathbf{D}\left(\mathcal{V}^*\boldsymbol{U}^*\right) + \boldsymbol{R}^* = 0 \tag{2.68}$$

To solve the harmonic balance equations, a "pseudo-time" term is introduced so that the equations may be marched rapidly to a steady-state condition using a conventional

computational fluid dynamics scheme. Thus, Eq. (2.68) becomes [22]

$$\frac{\partial}{\partial \tau}(\mathcal{V}^* \boldsymbol{U}^*) + \omega \mathbf{D}\left(\mathcal{V}^* \boldsymbol{U}^*\right) + \boldsymbol{R}^* = 0 \tag{2.69}$$

where τ is a fictitious or pseudo time, used only to march Eq. (2.69) to steady-state by driving the pseudo-time term to zero. The pseudo-time harmonic balance equations are similar in form to the original time domain equations (Eqs. 2.4). Thus, existing well-developed steady CFD techniques may be used to efficiently solve the nonlinear harmonic balance equations with a comparable number of iterations required.

2.5 Structural Dynamics

In order to study the effects of aerodynamic loading on a structure, a suitable structural dynamics model is required to relate the time-varying motion of the structure to the aerodynamic forces. In the absence of mechanical damping, the vibration of a structure subject to aerodynamic excitation is described by

$$\mathbf{M}\ddot{\boldsymbol{x}} + \mathbf{K}\boldsymbol{x} = \boldsymbol{F} \tag{2.70}$$

where $\mathbf{M}$ is the structural mass matrix, $\mathbf{K}$ is the structural stiffness matrix, $\boldsymbol{x}$ is the vector of physical displacements, and $\boldsymbol{F}$ is the vector of time-varying generalized aerodynamic forces given as

$$\mathbf{M} = \begin{bmatrix} m_{11} & m_{12} & m_{13} \\ m_{21} & m_{22} & m_{23} \\ m_{31} & m_{32} & m_{33} \end{bmatrix} \quad ; \quad \mathbf{K} = \begin{bmatrix} k_{11} & k_{12} & k_{13} \\ k_{21} & k_{22} & k_{23} \\ k_{31} & k_{32} & k_{33} \end{bmatrix} \tag{2.71}$$

$$\ddot{\boldsymbol{x}} = \begin{bmatrix} \ddot{x} \\ \ddot{y} \\ \ddot{z} \end{bmatrix} \quad ; \quad \boldsymbol{x} = \begin{bmatrix} x \\ y \\ z \end{bmatrix} \quad ; \quad \boldsymbol{F} = \begin{bmatrix} F_x \\ F_y \\ F_z \end{bmatrix} \tag{2.72}$$

For a wing or turbine blade, the total aerodynamic force is defined as

$$\boldsymbol{F} = \iint_A p\hat{\boldsymbol{n}} \cdot d\boldsymbol{A} + \iint_A \boldsymbol{\tau}_w \cdot d\boldsymbol{A} \tag{2.73}$$

where $\hat{\boldsymbol{n}}$ is the unit normal wall vector and $\boldsymbol{\tau}_w$ is the shear stress along the wing or blade surface.

When a structure is perturbed from its static equilibrium position, in the absence of structural damping and external forces, the response is called the free undamped vibration. Assuming sinusoidal motion, the structural displacement and acceleration can be written

$$\boldsymbol{x} = \boldsymbol{\phi}\sin\omega t \tag{2.74}$$

$$\ddot{\boldsymbol{x}} = -\boldsymbol{\phi}\omega^2\sin\omega t \tag{2.75}$$

where $\boldsymbol{\phi}$ is the amplitude of the displacement and ω is the frequency of vibration. Substituting Eqs. 2.74 and 2.75 into Eq. 2.70, one obtains the eigenvalue problem

$$\left(\mathbf{K} - \omega^2\mathbf{M}\right)\boldsymbol{\phi} = 0 \tag{2.76}$$

It is seen here that ω^2 represents the eigenvalue and $\boldsymbol{\phi}$ the associated eigenvector. In structural dynamics terminology, each eigenvalue or frequency has an associated eigenvector or mode shape.

There are an infinite number of mode shapes, but the first few are typically sufficient in structural modeling. Letting n represent the degrees-of-freedom of the model, the structural displacements can now be written in the x-direction, for example

$$x(t) = \sum_{i=1}^{n} \phi_i(x) q_i(t) \tag{2.77}$$

where ϕ_i is the ith mode shape and q_i the ith modal displacement. The governing equation in Eq. 2.70 in terms of the mode shapes becomes

$$\mathbf{M}\mathbf{\Phi}\ddot{\boldsymbol{q}} + \mathbf{K}\mathbf{\Phi}\boldsymbol{q} = \boldsymbol{F} \tag{2.78}$$

where the modal matrix $\mathbf{\Phi}$ is defined for n mode shapes as

$$\mathbf{\Phi} = \begin{bmatrix} \phi_1(x) & \phi_2(x) & \cdots & \phi_n(x) \\ \phi_1(y) & \phi_2(y) & \cdots & \phi_n(y) \\ \phi_1(z) & \phi_2(z) & \cdots & \phi_n(z) \end{bmatrix} \tag{2.79}$$

The governing equation can be simplified using mass normalized mode shapes. The mass normalized mode shape is defined as

$$\tilde{\boldsymbol{\phi}} = \frac{\boldsymbol{\phi}}{\sqrt{\boldsymbol{\phi}^T\mathbf{M}\boldsymbol{\phi}}} \tag{2.80}$$

where the denominator on the right hand side represents the square root of the generalized mass. Rewriting the governing equation in terms of mass normalized mode shapes and premultiplying by the transpose of $\tilde{\mathbf{\Phi}}$, one gets

$$\tilde{\mathbf{\Phi}}^T\mathbf{M}\tilde{\mathbf{\Phi}}\ddot{\boldsymbol{q}} + \tilde{\mathbf{\Phi}}^T\mathbf{K}\tilde{\mathbf{\Phi}}\boldsymbol{q} = \tilde{\mathbf{\Phi}}^T\boldsymbol{F} \tag{2.81}$$

Here, the mass normalized modal matrix and its transpose are given by

$$\tilde{\mathbf{\Phi}} = \begin{bmatrix} \tilde{\phi}_1(x) & \tilde{\phi}_2(x) & \cdots & \tilde{\phi}_n(x) \\ \tilde{\phi}_1(y) & \tilde{\phi}_2(y) & \cdots & \tilde{\phi}_n(y) \\ \tilde{\phi}_1(z) & \tilde{\phi}_2(z) & \cdots & \tilde{\phi}_n(z) \end{bmatrix} \quad ; \quad \tilde{\mathbf{\Phi}}^T = \begin{bmatrix} \tilde{\phi}_1(x) & \tilde{\phi}_1(y) & \tilde{\phi}_1(z) \\ \tilde{\phi}_2(x) & \tilde{\phi}_2(y) & \tilde{\phi}_2(z) \\ \vdots & \vdots & \vdots \\ \tilde{\phi}_n(x) & \tilde{\phi}_n(y) & \tilde{\phi}_n(z) \end{bmatrix} \tag{2.82}$$

Due to the orthogonality of the eigenvectors, the matrices on the left hand side are greatly simplified. Orthogonality and mass normalized mode shapes give the following

simplifications:

$$\tilde{\phi}_i^T M_{ij} \tilde{\phi}_j = 1 \quad \text{for } i = j \tag{2.83}$$

$$\tilde{\phi}_i^T M_{ij} \tilde{\phi}_j = 0 \quad \text{for } i \neq j \tag{2.84}$$

Similar simplifications can be used for the stiffness matrix. The governing equation is now decoupled and reduced to

$$m_j \ddot{q}_j + k_j q_j = \tilde{\phi}_j^{\,T} F_j \tag{2.85}$$

Dividing by the mass, the final desired form of the governing structural dynamics equation is obtained

$$\ddot{q}_j + \omega_j^2 q_j = \frac{\tilde{\phi}_j^{\,T}}{m_j} F_j \tag{2.86}$$

Chapter 3

Numerical Approach for Flow Solver

3.1 Non-Dimensionalization

It is convenient to work with a non-dimensional form of the governing fluids equations so that key parameters such as the Reynolds number and Mach number can be varied independently of each other. Non-dimensionalization also normalizes the results so that their limits fall in a convenient range, and it allows for easier comparison with other datasets [84].

Many non-dimensional sets of variables are possible, and one based on a reference length, pressure, and temperature is considered here. Additional reference quantities may be defined in terms of these user-defined quantities, which are given as

$$\rho_{ref} = \frac{p_{ref}}{R_{gas}T_{ref}} \; ; \quad V_{ref} = \sqrt{R_{gas}T_{ref}} \; ; \quad a_{ref} = \sqrt{\gamma R_{gas}T_{ref}} \; ; \quad \omega_{ref} = \frac{V_{ref}}{L_{ref}} \tag{3.1}$$

The gas constant, R_{gas}, is also user-defined. Using overbars to denote dimensionless quantities, the normalized variables are given as

$$\bar{x} = \frac{x}{L_{ref}} \; ; \quad \bar{y} = \frac{y}{L_{ref}} \; ; \quad \bar{z} = \frac{z}{L_{ref}} \; ; \quad \bar{t} = \frac{t}{L_{ref}/V_{ref}} \tag{3.2}$$

$$\bar{u} = \frac{u}{V_{ref}} \; ; \quad \bar{v} = \frac{v}{V_{ref}} \; ; \quad \bar{w} = \frac{w}{V_{ref}} \; ; \quad \bar{\omega} = \frac{\omega}{\omega_{ref}} \tag{3.3}$$

$$\bar{\mu} = \frac{\mu}{\rho_{ref} V_{ref} L_{ref}} \; ; \quad \bar{\rho} = \frac{\rho}{\rho_{ref}} \; ; \quad \bar{p} = \frac{p}{p_{ref}} \; ; \quad \bar{T} = \frac{T}{T_{ref}} \tag{3.4}$$

This choice of non-dimensionalization affects the form of the equation of state. Substituting the above definitions into Eq. 2.14, the ideal gas law takes the form

$$\bar{p} = \bar{\rho}\bar{T} \tag{3.5}$$

For external flow problems, the free stream quantities are typically set to unity. Following the form of the ideal gas law in Eq. 3.5, the free stream quantities are given by

$$\bar{T}_\infty = \bar{p}_\infty = \bar{\rho}_\infty = 1 \; ; \quad \bar{a}_\infty = \sqrt{\gamma} \tag{3.6}$$

For viscous simulations, the Reynolds number is required to properly scale all viscous quantities. The Reynolds number based on reference values is given by

$$\mathrm{Re} = \frac{\rho_{ref} V_{ref} L_{ref}}{\mu_{ref}} \tag{3.7}$$

Since p_{ref}, T_{ref}, and R_{gas} are usually fixed for a given problem, the reference length, L_{ref}, is used to set the Reynolds number to the appropriate value.

3.2 Spatial Discretization

The governing fluids equations presented in Chapter 2 are discretized using a cell-centered finite volume approach. In this section, the grid topology and details of the cell-centered discretization are covered. A central and upwind difference method for computing the convective fluxes is included as well as a central difference method for the viscous fluxes.

3.2.1 Grid Topology

The current flow solver is written specifically for a C-grid type mesh. This mesh gets its name from the shape of the grid, which resembles a capital C. Figure 3.1 shows a 2-D diagram of a C-grid type mesh on the left hand side and the associated computational plane on the right. A C-grid is formed by lines of constant η that wrap around the airfoil in a clockwise direction. The lines run from $\eta = 0$ on the aifoil surface to $\eta = \eta_{max}$ in the far field. Lines of constant ξ emanate from the airfoil surface and wake and run from $\xi = 0$ to $\xi = \xi_{max}$.

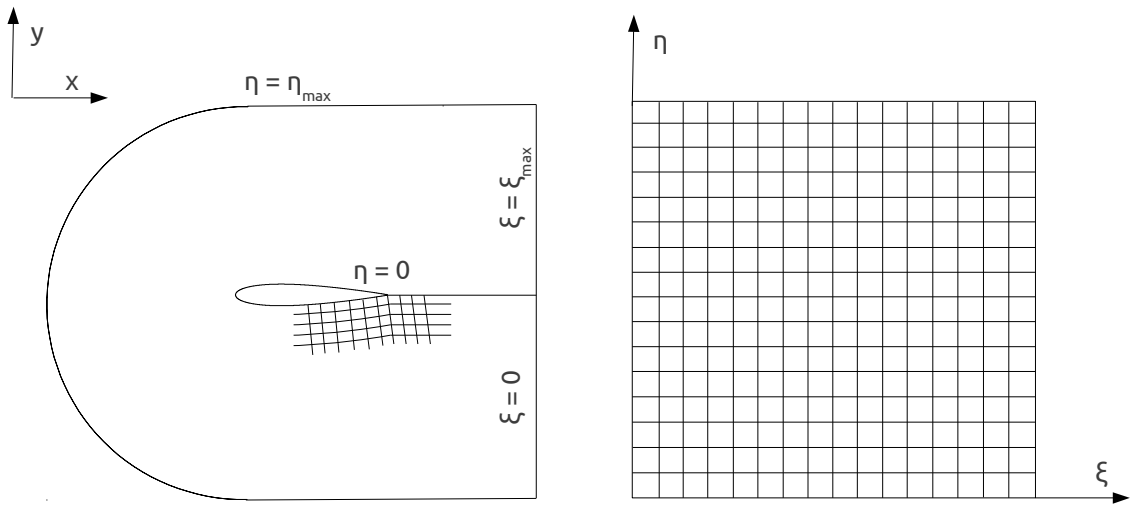

Figure 3.1: C-grid topology. **Left**: Physical plane. **Right**: Computational plane.

Each point in physical space is mapped onto the computational plane by a unique value of ξ and η such that points may be addressed as $x(\xi, \eta)$ and $y(\xi, \eta)$. If ξ is defined as the i-direction and η as the j-direction, then cells neighboring a particular control volume are easily addressed by adding or subtracting one from the current cell address. This feature is very useful for programming and defining fluxes at cell faces. The line connecting the airfoil trailing edge and far field is known as a coordinate cut. In addition to the airfoil surface and far field, this boundary must also receive special attention. This topic is discussed further in section 3.4.

For 3-D cases, the solver is written for C-H type grids. These grids are formed with a single C-grid in each k-plane, where ζ is the k-direction. Points in this case are addressed as $x(\xi, \eta, \zeta)$, $y(\xi, \eta, \zeta)$, and $z(\xi, \eta, \zeta)$. For flows about fixed wings, the C-grid in each k-plane is similar to that shown in Fig. 3.1. For rotating flows, each k-plane is wrapped around the center of rotation so that each plane takes on a cylindrical shape. Examples of these grids appear in Chapters 5 and 7.

3.2.2 Cell-Centered Approach

With a cell-centered discretization, the control volumes coincide with the grid cells. The values of the flow variables are stored at the centroids of the control volumes, and the fluxes are computed at the faces of the control volumes. This situation is depicted in Fig. 3.2. The alternative approach is a cell-vertex scheme where the flow variables are stored at the nodes of the grid, and control volumes are defined that do not coincide with the mesh. Both approaches have advantages and disadvantages. For example, the cell-centered scheme is better near sharp corners and branch cuts, but the cell-vertex scheme has higher accuracy on unrefined grids. The cell-centered scheme is used here since accuracy is negligible compared to cell-vertex schemes on smooth grids and better documentation seems to be more available in literature on cell-centered schemes.

A few geometric quantities associated with the control volume must be defined. The volume of the cell in 2-D is easily computed with

$$\mathcal{V}_{i,j} = \frac{1}{2}\left[\left(x_A - x_C\right)\left(y_B - y_D\right) + \left(x_D - x_B\right)\left(y_A - y_C\right)\right] \tag{3.8}$$

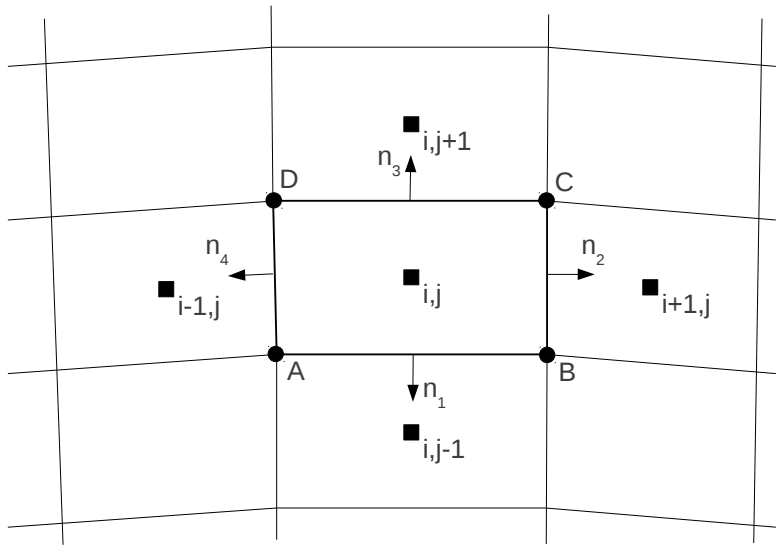

Figure 3.2: Cell-centered discretization

Each face of the control volume has a face vector $\boldsymbol{S}$ and unit normal $\hat{\mathbf{n}}$ that may be defined on Face 1, for example, by

$$S_{x,1} = y_B - y_A \ ; \quad S_{y,1} = x_A - x_B \tag{3.9}$$

$$\hat{n}_{x,1} = \frac{S_{x,1}}{||\boldsymbol{S}_1||} \ ; \quad \hat{n}_{y,1} = \frac{S_{y,1}}{||\boldsymbol{S}_1||} \tag{3.10}$$

where $||\boldsymbol{S}_1||$ is the magnitude of the face vector. The volumes and face vectors are more complicated in 3-D, and formulas for these quantities may be found in Appendix A.

3.2.3 Convective Fluxes

Two methods are described here to compute the convective fluxes. The first method is a central scheme with artificial dissipation known as the JST scheme. It is named for the authors of the original paper - Jameson, Schmidt, and Turkel [37]. The second method is the flux difference splitting scheme of Roe [68]. Details, advantages, and disadvantages of each method are provided in the next two sections. The central

scheme was typically used in this work during code development due to its simple programming and computational efficiency. The Roe scheme was used in final results for its better accuracy near flow gradients.

Central Scheme

The central scheme of Jameson et al. [37] became very popular due to its easy implementation and low computational cost compared to other flux discretizations [11]. The idea behind the scheme is to compute the convective flux at each face of a control volume using the average of the flow variables on either side of the face. Mathematically, this may be written for the $i+1/2, j, k$ face as

$$(\boldsymbol{F_c}\Delta S)_{i+1/2,j,k} \approx \boldsymbol{F_c}\left(\boldsymbol{U}_{i+1/2,j,k}\right)\Delta S_{i+1/2,j,k} \tag{3.11}$$

where

$$\boldsymbol{U}_{i+1/2,j,k} = \frac{1}{2}\left(\boldsymbol{U}_{i,j,k} + \boldsymbol{U}_{i+1,j,k}\right) \tag{3.12}$$

Two major disadvantages of the central scheme are even-odd decoupling of the solution and oscillations near discontinuities such as shock waves. Artificial dissipation is added to the scheme to alleviate these problems. With the addition of the artificial dissipation, the convective flux in Eq. 3.11 becomes

$$(\boldsymbol{F_c}\Delta S)_{i+1/2,j,k} \approx \boldsymbol{F_c}\left(\boldsymbol{U}_{i+1/2,j,k}\right)\Delta S_{i+1/2,j,k} - \boldsymbol{D}_{i+1/2,j,k} \tag{3.13}$$

where $D_{i+1/2,j,k}$ is the artificial dissipation flux at the cell face. The artificial dissipation is constructed from a blending of second and fourth order differences, which take the form

$$\begin{aligned}\boldsymbol{D}_{i+1/2,j,k} = \lambda_{i+1/2,j,k}\Big[&\epsilon^{(2)}_{i+1/2,j,k}\left(\boldsymbol{U}_{i+1,j,k} - \boldsymbol{U}_{i,j,k}\right)\\ &-\epsilon^{(4)}_{i+1/2,j,k}\left(\boldsymbol{U}_{i+2,j,k} - 3\boldsymbol{U}_{i+1,j,k} + 3\boldsymbol{U}_{i,j,k} - \boldsymbol{U}_{i-1,j,k}\right)\Big]\end{aligned} \tag{3.14}$$

The dissipation is scaled by the sum of the spectral radii in each coordinate direction at the cell face, or

$$\lambda_{i+1/2,j,k} = \lambda^{i}_{i+1/2,j,k} + \lambda^{j}_{i+1/2,j,k} + \lambda^{k}_{i+1/2,j,k} \tag{3.15}$$

The spectral radius at the cell face in a single coordinate direction is taken as the average of the spectral radii of the two cells adjacent to the face. The spectral radius in a coordinate direction is determined from the convective flux Jacobian. For example, in the i or ξ direction, the spectral radius is given by

$$\lambda^{i}_{i,j,k} = (|V| + c)\,\Delta S \tag{3.16}$$

The coefficients in Eq. 3.14 are used to adjust the numerical dissipation depending on the local flow conditions. In smooth regions of the flow, the fourth-order difference terms associated with $\epsilon^{(4)}$ are active to damp the oscillations arising due to the central difference scheme. Near strong discontinuities, the fourth-order difference terms are reduced, and the second-order difference terms associated with $\epsilon^{(2)}$ are increased. A pressure-based switch is used to adjust these terms accordingly, which is written

$$\nu_{i,j,k} = \frac{|p_{i-1,j,k} - 2p_{i,j,k} + p_{i+1,j,k}|}{p_{i-1,j,k} + 2p_{i,j,k} + p_{i+1,j,k}} \tag{3.17}$$

The second- and fourth-order coefficients are defined as

$$\epsilon^{(2)}_{i+1/2,j,k} = \kappa^{(2)} \max\left(\nu_{i,j,k}, \nu_{i+1,j,k}\right) \tag{3.18}$$

$$\epsilon^{(4)}_{i+1/2,j,k} = \max\left[0, \left(\kappa^{(4)} - \epsilon^{(2)}_{i+1/2,j,k}\right)\right] \tag{3.19}$$

The constants in Eqs. 3.18 and 3.19 are typically in the range $0.25 < k^{(2)} < 0.50$ and $0.008 < k^{(4)} < 0.032$.

For viscous solutions where high aspect ratio cells are needed to resolve the boundary layer, the above scaling factor creates too much artificial dissipation. The

modified scaling factor of Martinelli [51] is used instead for viscous cases with the modified spectral radii defined according to

$$\hat{\lambda}^i_{i,j,k} = \phi_{i,j,k}\lambda^i_{i,j,k} \tag{3.20}$$

where

$$\phi_{i,j,k} = 1 + \left(\frac{\lambda^j_{i,j,k}}{\lambda^i_{i,j,k}}\right)^{\zeta} \tag{3.21}$$

The exponent ζ is usually between 1/2 and 2/3. The artificial dissipation in the wall normal direction of the boundary layer can be reduced further while maintaining stability since the flow contains enough physical viscosity in this region. Following the approach mentioned by Swanson and Turkel [80], the artificial dissipation is scaled as

$$\hat{D}_{i,j+1/2,k} = \frac{M_{i,j,k}}{M_\infty}\boldsymbol{D}_{i,j+1/2,k} \tag{3.22}$$

Upwind Scheme

The basic concept behind flux-difference splitting schemes is to solve the shock tube problem at each face of the control volume. The exact solution for this problem requires solving a nonlinear system of equations. To reduce the computational effort, Roe [68] solved a linear approximation to the problem. His approach became popular due to its better resolution of boundary layers and shocks compared to the central scheme from Section 3.2.3, but implementation is more tedious and the computational workload is greater.

To see how Roe's scheme is formed, one may start with a linear approximation to the one-dimensional shock tube (also known as Riemann) problem, which is given as

$$\frac{\partial \boldsymbol{U}}{\partial t} + \mathbf{A}_{Roe}\frac{\partial \boldsymbol{U}}{\partial x} = 0 \tag{3.23}$$

where $\mathbf{A}_{Roe}$ is the Roe-averaged matrix. This matrix is the same as the convective flux Jacobian, but averaged values of the flow variables at the interface are used in

place of the normal flow variables. These Roe-averaged variables must satisfy special conditions that will not be presented here, but the variables are defined as

$$\tilde{\rho} = \sqrt{\rho_L \rho_R} \; ; \quad \tilde{u} = \frac{u_L\sqrt{\rho_L} + u_R\sqrt{\rho_R}}{\sqrt{\rho_L} + \sqrt{\rho_R}} \tag{3.24}$$

$$\tilde{v} = \frac{v_L\sqrt{\rho_L} + v_R\sqrt{\rho_R}}{\sqrt{\rho_L} + \sqrt{\rho_R}} \; ; \quad \tilde{w} = \frac{w_L\sqrt{\rho_L} + w_R\sqrt{\rho_R}}{\sqrt{\rho_L} + \sqrt{\rho_R}} \tag{3.25}$$

$$\tilde{H} = \frac{H_L\sqrt{\rho_L} + H_R\sqrt{\rho_R}}{\sqrt{\rho_L} + \sqrt{\rho_R}} \; ; \quad \tilde{c} = \sqrt{(\gamma - 1)\left(\tilde{H} - \tilde{q}^2/2\right)} \tag{3.26}$$

$$\tilde{V} = \tilde{u}n_x + \tilde{v}n_y + \tilde{w}n_z \; ; \quad \tilde{q}^2 = \tilde{u}^2 + \tilde{v}^2 + \tilde{w}^2 \tag{3.27}$$

Returning to the 1-D problem, if the Roe-averaged matrix is diagnolized and inserted into Eq. 3.23, one obtains

$$\frac{\partial \boldsymbol{U}}{\partial t} + \mathbf{T}\boldsymbol{\Lambda}\mathbf{T}^{-1}\frac{\partial \boldsymbol{U}}{\partial x} = 0 \tag{3.28}$$

where $\mathbf{T}$ and $\mathbf{T}^{-1}$ are the matrices of right and left eigenvectors, respectively, and $\boldsymbol{\Lambda}$ is the matrix of eigenvalues all obtained using the Roe-averaged matrix. Defining a vector $\boldsymbol{W} = \mathbf{T}^{-1}\boldsymbol{U}$, Eq. 3.28 may now be written in a linear form, which is given as

$$\frac{\partial \boldsymbol{W}}{\partial t} + \bar{\Lambda}\frac{\partial \boldsymbol{W}}{\partial x} = 0 \tag{3.29}$$

The value of W_k is constant along characteristics defined by λ_k until a wave associated with another eigenvalue of the system is crossed where W_k experiences a jump in value. Since $\mathbf{A}_{Roe}$ is a constant matrix, the conservative variables and fluxes also follow this behavior so that the flux changes may be written

$$(F_c)_k = (F_c)_1 + \sum_{j=2}^{k} \delta\,(F_c)_j \tag{3.30}$$

where the summation terms are the incremental jumps associated with crossing each wave of the system. Now writing the flux changes for the entire system of equations and using the left and right states, the fluxes are related by

$$\boldsymbol{F}_c\left(\boldsymbol{U}_R\right) = \boldsymbol{F}_c\left(\boldsymbol{U}_L\right) + \mathbf{A}_{Roe}\left(\boldsymbol{U}_R - \boldsymbol{U}_L\right) \tag{3.31}$$

If the Roe matrix is split according to the diagonalization from before so that the flux is decomposed into contributions from negative and positive waves at the face of the control volume, two equally valid expressions for the flux are

$$\left(\boldsymbol{F}_c\right)_{i+1/2,j,k} = \boldsymbol{F}_c\left(\boldsymbol{U}_L\right) + \mathbf{A}_{Roe}^{-}\left(\boldsymbol{U}_R - \boldsymbol{U}_L\right) \tag{3.32}$$

$$\left(\boldsymbol{F}_c\right)_{i+1/2,j,k} = \boldsymbol{F}_c\left(\boldsymbol{U}_R\right) - \mathbf{A}_{Roe}^{+}\left(\boldsymbol{U}_R - \boldsymbol{U}_L\right) \tag{3.33}$$

The flux is usually written as an average of Eqs. 3.32 and 3.33. The final expression for the convective flux at the face of the control volume is given as

$$\left(\boldsymbol{F}_c\right)_{i+1/2,j,k} = \frac{1}{2}\left[\boldsymbol{F}_c\left(\boldsymbol{U}_R\right) + \boldsymbol{F}_c\left(\boldsymbol{U}_L\right) - \left|\mathbf{A}_{Roe}\right|\left(\boldsymbol{U}_R - \boldsymbol{U}_L\right)\right] \tag{3.34}$$

The final term in Eq. 3.34 may be evaluated as

$$\left|\mathbf{A}_{Roe}\right|\left(\boldsymbol{U}_R - \boldsymbol{U}_L\right) = \left|\Delta\boldsymbol{F}_1\right| + \left|\Delta\boldsymbol{F}_{2,3,4}\right| + \left|\Delta\boldsymbol{F}_5\right| \tag{3.35}$$

where

$$\left|\Delta\boldsymbol{F}_1\right| = \left|\tilde{V} - \tilde{c}\right|\left(\frac{\Delta p - \tilde{\rho}\tilde{c}\Delta V}{2\tilde{c}^2}\right)\begin{bmatrix} 1 \\ \tilde{u} - \tilde{c}n_x \\ \tilde{v} - \tilde{c}n_y \\ \tilde{w} - \tilde{c}n_z \\ \tilde{H} - \tilde{c}\tilde{V} \end{bmatrix} \tag{3.36}$$

$$|\Delta \boldsymbol{F}_{2,3,4}| = |\tilde{V}| \left(\Delta\rho - \frac{\Delta p}{\tilde{c}^2} \right) \begin{bmatrix} 1 \\ \tilde{u} \\ \tilde{v} \\ \tilde{w} \\ \tilde{q}^2/2 \end{bmatrix} + \tilde{\rho} \begin{bmatrix} 0 \\ \Delta u - \Delta V n_x \\ \Delta v - \Delta V n_y \\ \Delta w - \Delta V n_z \\ \tilde{u}\Delta u + \tilde{v}\Delta v + \tilde{w}\Delta w + \tilde{V}\Delta V \end{bmatrix} \tag{3.37}$$

$$|\Delta \boldsymbol{F}_5| = |\tilde{V} + \tilde{c}| \left(\frac{\Delta p + \tilde{\rho}\tilde{c}\Delta V}{2\tilde{c}^2} \right) \begin{bmatrix} 1 \\ \tilde{u} + \tilde{c}n_x \\ \tilde{v} + \tilde{c}n_y \\ \tilde{w} + \tilde{c}n_z \\ \tilde{H} + \tilde{c}\tilde{V} \end{bmatrix} \tag{3.38}$$

The Roe scheme as just described is only first-order accurate in the characteristic coordinate. Second-order accuracy is achieved using the Monotone Upstream-Centered Schemes for Conservation Laws (MUSCL) approach of van Leer [95]. In order to prevent oscillations near strong flow gradients, limiters must be used with second-order upwind spatial discretizations. The purpose of limiters is to restrict the interpolation of flow variables to the control volume faces such that the scheme remains total variation diminishing (TVD). The limited MUSCL scheme may be written according to Spekreijse [76] as

$$U_R = U_{i+1,j,k} - \frac{1}{2}\Psi_R \left(U_{i+2,j,k} - U_{i+1,j,k} \right) \tag{3.39}$$

$$U_L = U_{i,j,k} + \frac{1}{2}\Psi_R \left(U_{i,j,k} - U_{i-1,j,k} \right) \tag{3.40}$$

The Roe scheme can be given a second-order upwind bias using the van Albada [92] limiter, which is given by

$$\Psi = \frac{r^2 + r}{1 + r^2} \tag{3.41}$$

The right and left states in Eqs. 3.39 and 3.40 now become

$$U_R = U_{i+1,j,k} - \frac{1}{2}\delta_R \tag{3.42}$$

$$U_L = U_{i,j,k} + \frac{1}{2}\delta_L \tag{3.43}$$

where

$$\delta = \frac{a\left(b^2+\epsilon\right) + b\left(a^2+\epsilon\right)}{a^2+b^2+2\epsilon} \tag{3.44}$$

and

$$a_R = U_{i+2,j,k} - U_{i+1,j,k}\ ; \quad b_R = U_{i+1,j,k} - U_{i,j,k} \tag{3.45}$$

$$a_L = U_{i+1,j,k} - U_{i,j,k}\ ; \quad b_L = U_{i,j,k} - U_{i-1,j,k} \tag{3.46}$$

The limiter changes the scheme to first-order near strong discontinuities to preserve monotonicity. In smooth regions, the limiter is turned off so that the solution is unaffected. The parameter in Eq. 3.44 is used to prevent the limiter from incorrectly turning on in a smooth region of the flow near small oscillations [98].

3.2.4 Viscous Fluxes

The viscous fluxes are evaluated with central differences no matter the scheme used for the convective fluxes. The viscous flux terms contain derivatives that must be evaluated at the cell faces [11]. As in the JST scheme, the required flow variables are averaged at the face of the control volume. In the 2-D code, the derivatives are evaluated using Green's theorem. Green's theorem provides a relationship between the volume integral of the first derivative of a variable and the surface integral of the same variable. The derivative of u in the x-direction, for example, is approximated as

$$\frac{\partial u}{\partial x} = \frac{1}{\mathcal{V}'}\iint_{\mathcal{V}'} \frac{\partial u}{\partial x}\, dxdy = \frac{1}{\mathcal{V}'}\int_{\partial\mathcal{V}'} u\ dy \approx \frac{1}{\mathcal{V}'}\sum_{m=1}^{N_F} u_m S'_{x,m} \tag{3.47}$$

where $\mathcal{V}'$ is the volume of the auxiliary cell and N_F is the number of faces of the auxiliary cell. The situation is depicted in Fig. 3.3 for the flux across the $i+1/2$ face.

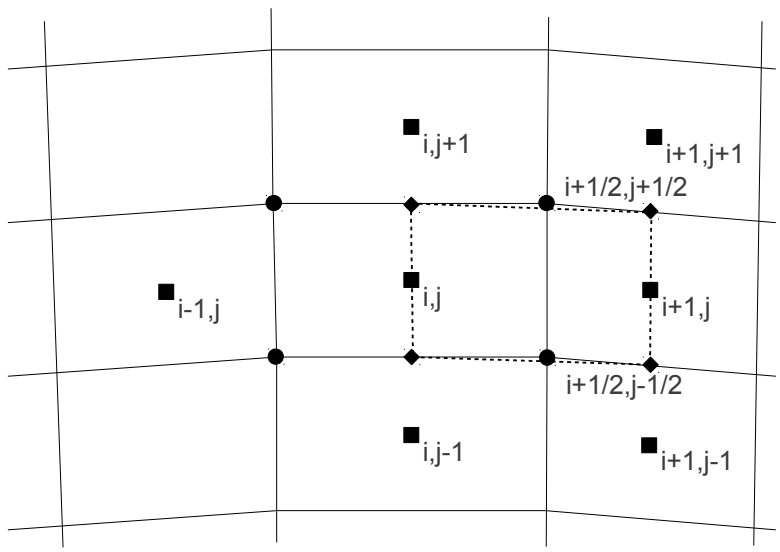

Figure 3.3: Viscous flux auxiliary cell

To use Eq. 3.47, the value of the flow variable must be known at the center of each face of the auxiliary cell. The values at i, j and $i+1, j$ are known directly. The values at $i+1/2, j+1/2$ and $i+1/2, j-1/2$ are taken as the average of the four surrounding cells. The value of u at $i+1/2, j+1/2$, for example, is taken as

$$u_{i+1/2,j+1/2} = \frac{1}{4}\left(u_{i,j} + u_{i+1,j} + u_{i,j+1} + u_{i+1,j+1}\right) \tag{3.48}$$

Viscous fluxes computed with the above approach are second order accurate on smooth grids [79]. Use of Green's theorem is less accurate on non-uniform grids. Closer inspection of Fig. 3.3 reveals the reason. Since the grid is non-uniform, the auxiliary cell does not perfectly enclose the face. Thus, as grid quality deteriorates, derivatives found using Green's theorem become more approximate.

Green's theorem can be used in 3-D, but defining auxiliary cells and appropriate values at the auxiliary cell faces becomes more cumbersome. An alternate approach

for calculating derivatives is the use of coordinate transformations. This approach is also more efficient for calculating derivatives at the cell centers, which are needed for turbulence and transition model source terms. Recalling that $x = x(\xi, \eta)$ and $y = y(\xi, \eta)$, the derivatives of u in the x- and y-directions in 2-D may be written in terms of ξ and η using the chain rule

$$\frac{\partial u}{\partial x} = \frac{\partial \xi}{\partial x}\frac{\partial u}{\partial \xi} + \frac{\partial \eta}{\partial x}\frac{\partial u}{\partial \eta} \tag{3.49}$$

$$\frac{\partial u}{\partial y} = \frac{\partial \xi}{\partial y}\frac{\partial u}{\partial \xi} + \frac{\partial \eta}{\partial y}\frac{\partial u}{\partial \eta} \tag{3.50}$$

The metric terms in Eqs. 3.49-3.50 are defined

$$\frac{\partial \xi}{\partial x} = J\frac{\partial y}{\partial \eta}\ ;\quad \frac{\partial \eta}{\partial x} = -J\frac{\partial y}{\partial \xi}\ ;\quad \frac{\partial \xi}{\partial y} = -J\frac{\partial x}{\partial \eta}\ ;\quad \frac{\partial \eta}{\partial y} = J\frac{\partial x}{\partial \xi} \tag{3.51}$$

where J is the coordinate transformation Jacobian. The inverse of the determinant of J is defined

$$J^{-1} = \frac{\partial x}{\partial \xi}\frac{\partial y}{\partial \eta} - \frac{\partial x}{\partial \eta}\frac{\partial y}{\partial \xi} \tag{3.52}$$

The gradient terms appearing in Eqs. 3.51-3.52 are approximated using second order accurate central finite differences. Figure 3.4 defines required terms for computing the derivative at a cell center in 2-D. The ξ-direction derivatives at i, j, for example, are approximated

$$\left(\frac{\partial u}{\partial \xi}\right)_{i,j} = \frac{\frac{1}{2}\left[(u_{i,j} + u_{i+1,j}) - (u_{i,j} + u_{i-1,j})\right]}{(i+1/2) - (i-1/2)} = \frac{1}{2}\left(u_{i+1,j} - u_{i-1,j}\right) \tag{3.53}$$

$$\left(\frac{\partial x}{\partial \xi}\right)_{i,j} = \frac{\frac{1}{2}\left[(x_{i,j} + x_{i+1,j}) - (x_{i,j} + x_{i-1,j})\right]}{(i+1/2) - (i-1/2)} = \frac{1}{2}\left(x_{i+1,j} - x_{i-1,j}\right) \tag{3.54}$$

$$\left(\frac{\partial y}{\partial \xi}\right)_{i,j} = \frac{\frac{1}{2}\left[(y_{i,j} + y_{i+1,j}) - (y_{i,j} + y_{i-1,j})\right]}{(i+1/2) - (i-1/2)} = \frac{1}{2}\left(y_{i+1,j} - y_{i-1,j}\right) \tag{3.55}$$

A similar approach can be used to compute the gradient terms at the cell faces in lieu of Green's theorem. Both methods are valid, and Swanson and Turkel [81] note

that no significant differences are observed between results found using either method. The full 3-D metric terms and transformation Jacobian are available elsewhere [11].

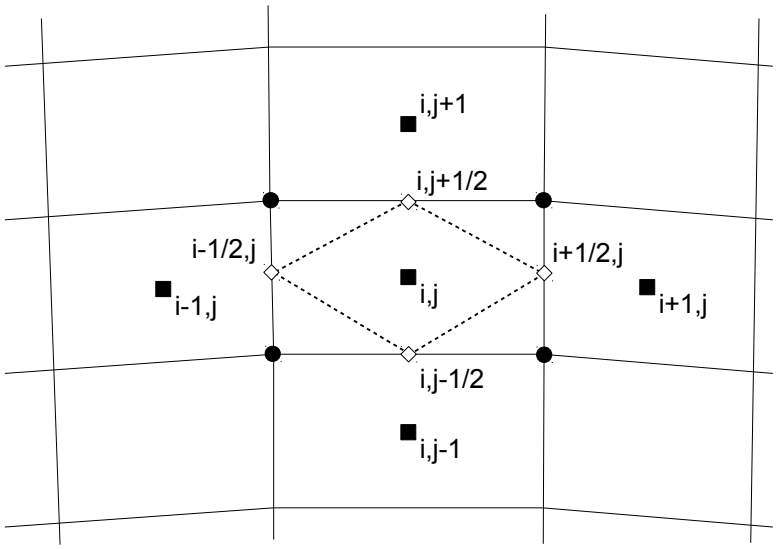

Figure 3.4: Viscous flux auxiliary cell

3.3 Temporal Discretization

The discretized equations can be marched forward in time using either an explicit or implicit time integration method. The explicit method presented here is a widely used, hybrid Runge-Kutta scheme that has been optimized for efficiency and stability. The major drawback of this method like any explicit time integration method is the restriction placed on the maximum allowable time step for stability [20]. The implicit method described below is known as lower-upper symmetric Gauss-Seidel or LU-SGS. Implicit methods do not suffer from time step restrictions, but simplifications are necessary to allow inversion of the implicit operator using iterative methods. These simplifications place limits on the time step.

3.3.1 Runge-Kutta Scheme

For an explicit scheme, the solution at the next time step $(t + \Delta t)$ is computed from the known solution and corresponding residual at the current time level. Denoting the current time level n, an explicit scheme takes the form

$$\boldsymbol{U}^n_{i,j,k} = -\frac{\Delta t_{i,j,k}}{\mathcal{V}_{i,j,k}} \boldsymbol{R}^n_{i,j,k} \tag{3.56}$$

where $\boldsymbol{R}^n_{i,j,k}$ is the residual at the current time level. Many methods are available to solve the above equation, but Runge-Kutta schemes have become the most common.

Jameson et al. [37] presented an explicit Runge-Kutta or multistage scheme for use with their central spatial discretization of the Euler equations. Since memory requirements were more restrictive 30 years ago, the scheme stored only the zeroth solution and final residual. Stage coefficients were introduced to improve stability and increase the maximum allowable time step.

It is possible to reduce the computational workload by only computing the viscous and artificial dissipation fluxes at certain stages. The dissipation terms from different stages can be blended for stages in which the dissipation is not computed. One of the most popular hybrid schemes is known as the (5,3)-scheme, which is given as

$$\boldsymbol{U}^{(0)}_{i,j,k} = \boldsymbol{U}^n_{i,j,k} \tag{3.57}$$

$$\boldsymbol{U}^{(1)}_{i,j,k} = \boldsymbol{U}^{(0)}_{i,j,k} - \alpha_1 \frac{\Delta t_{i,j,k}}{\mathcal{V}_{i,j,k}} \left[\boldsymbol{R}^{(0)}_c - \boldsymbol{R}^{(0)}_d \right]_{i,j,k} \tag{3.58}$$

$$\boldsymbol{U}^{(2)}_{i,j,k} = \boldsymbol{U}^{(0)}_{i,j,k} - \alpha_2 \frac{\Delta t_{i,j,k}}{\mathcal{V}_{i,j,k}} \left[\boldsymbol{R}^{(1)}_c - \boldsymbol{R}^{(0)}_d \right]_{i,j,k} \tag{3.59}$$

$$\boldsymbol{U}^{(3)}_{i,j,k} = \boldsymbol{U}^{(0)}_{i,j,k} - \alpha_3 \frac{\Delta t_{i,j,k}}{\mathcal{V}_{i,j,k}} \left[\boldsymbol{R}^{(2)}_c - \boldsymbol{R}^{(2,0)}_d \right]_{i,j,k} \tag{3.60}$$

$$\boldsymbol{U}^{(4)}_{i,j,k} = \boldsymbol{U}^{(0)}_{i,j,k} - \alpha_4 \frac{\Delta t_{i,j,k}}{\mathcal{V}_{i,j,k}} \left[\boldsymbol{R}^{(3)}_c - \boldsymbol{R}^{(2,0)}_d \right]_{i,j,k} \tag{3.61}$$

$$\boldsymbol{U}^{n+1}_{i,j,k} = \boldsymbol{U}^{(0)}_{i,j,k} - \alpha_5 \frac{\Delta t_{i,j,k}}{\mathcal{V}_{i,j,k}} \left[\boldsymbol{R}^{(4)}_c - \boldsymbol{R}^{(4,2)}_d \right]_{i,j,k} \tag{3.62}$$

$$\tag{3.63}$$

where

$$\boldsymbol{R}_d^{(2,0)} = \beta_3 \boldsymbol{R}_d^{(2)} + (1 - \beta_3)\, \boldsymbol{R}_d^{(0)} \tag{3.64}$$

$$\boldsymbol{R}_d^{(4,2)} = \beta_5 \boldsymbol{R}_d^{(4)} + (1 - \beta_5)\, \boldsymbol{R}_d^{(2,0)} \tag{3.65}$$

The name (5,3)-scheme is given to this particular method since it is a 5-stage Runge-Kutta integration with the dissipation calculated during three of the stages. A closely related approach is to calculate the viscous fluxes at the first stage only to further reduce the computational workload.

The stage and blending coefficients for the (5-3)-scheme are given in Table 3.1 for central and upwind discretizations. It should also be noted that the maximum stable CFL number for the central scheme in this approach is 3.5 [82], and for the upwind scheme, it is 2.0 [83].

Table 3.1: Coefficients for Hybrid Multistage Runge-Kutta Scheme

	Central		**Upwind**	
Stage	α	β	α	β
1	0.2500	1.0000	0.2742	1.0000
2	0.1667	0.0000	0.2067	0.0000
3	0.3750	0.5600	0.5020	0.5600
4	0.5000	0.0000	0.5142	0.0000
5	1.0000	0.4400	1.0000	0.4400

The maximum stable time step is easily determined on structured meshes. For a given cell, the inviscid time step is defined

$$\Delta t_{i,j,k} = \mathrm{CFL} \frac{\mathcal{V}_{\mathrm{i,j,k}}}{(\lambda_{\mathrm{i}} + \lambda_{\mathrm{j}} + \lambda_{\mathrm{k}})_{\mathrm{i,j,k}}} \tag{3.66}$$

where λ_i is the spectral radius of the convective flux Jacobian in the ξ-direction and similarly for λ_j and λ_k. For viscous flows, the viscous spectral radii must be included

so the time step becomes

$$\Delta t_{i,j,k} = \mathrm{CFL}\frac{\mathcal{V}_{i,j,k}}{(\lambda_i + \lambda_j + \lambda_k)_{i,j,k} + 4\left((\lambda_v)_i + (\lambda_v)_j + (\lambda_v)_k\right)_{i,j,k}} \tag{3.67}$$

where the viscous spectral radius in the ξ-direction, for example, is given by

$$(\lambda_v)_i = \max\left(\frac{4}{3\rho}, \frac{\gamma}{\rho}\right)\left(\frac{\mu_L}{Pr_L} + \frac{\mu_T}{\mathrm{Pr}_T}\right)\frac{\Delta S_i}{\mathcal{V}_{i,j,k}} \tag{3.68}$$

and Pr_L and Pr_T are the laminar and turbulent Prandtl numbers, respectively.

The source terms in the transition model increase the stiffness of the governing equations significantly. For an explicit scheme, the time step must be drastically reduced in order to keep the scheme stable, which will increase the steady state computation time considerably. The time step restriction can be relaxed if a matrix time step is used rather than a single time step for all equations. This approach has been used for to stabilize explicit schemes with two equation turbulence models with stiff source terms [47, 56]. To develop the idea, the residual term in the explicit scheme in Eq. 3.56 is written in full form to give

$$\boldsymbol{U}^n_{i,j,k} = -\frac{\Delta t_{i,j,k}}{\mathcal{V}_{i,j,k}}\left[\left(\boldsymbol{F}^n_c - \boldsymbol{F}^n_v\right)_{i,j,k}\Delta S - \mathcal{V}_{i,j,k}\boldsymbol{S}^{n+1}_{i,j,k}\right] \tag{3.69}$$

The source term is unknown at time level $n+1$ so it must be linearized about the current time level. Retaining first order terms, the linearized source term is written

$$\boldsymbol{S}^{n+1}_{i,j,k} \approx \boldsymbol{S}^n_{i,j,k} + \frac{\partial \boldsymbol{S}}{\partial \boldsymbol{U}}\Delta \boldsymbol{U}^n_{i,j,k} \tag{3.70}$$

Replacing the source term in Eq. 3.69 with the linearization of Eq. 3.70, the new explicit scheme becomes

$$\left[\frac{\mathbf{I}}{\Delta t_{i,j,k}} - \left(\frac{\partial \boldsymbol{S}}{\partial \boldsymbol{U}}\right)_{i,j,k}\right]\Delta \boldsymbol{U}^n_{i,j,k} = -\frac{1}{\mathcal{V}_{i,j,k}}\boldsymbol{R}^n_{i,j,k} \tag{3.71}$$

The effective time step is now given by the term in brackets on the left hand side of Eq. 3.71. The new form allows the governing equations to be integrated in time at the maximum stable time step for each equation.

3.3.2 Lower-Upper Symmetric Gauss-Seidel Scheme (LU-SGS)

For an implicit scheme, the solution at the next time step $(t + \Delta t)$ is computed from the known solution at the current time level n and the unknown residual at the $n+1$ time level. A popular implicit form is given by

$$\boldsymbol{U}^{n}_{i,j,k} = -\frac{\Delta t_{i,j,k}}{\mathcal{V}_{i,j,k}} \boldsymbol{R}^{n+1}_{i,j,k} \tag{3.72}$$

where $\boldsymbol{R}^{n+1}_{i,j,k}$ is the residual at the next time level. The unknown residual at the $n+1$ time level can be linearized about the current time level as was done with the source term in the previous section. Thus, a first order approximation for the residual at the next time level takes the form

$$\boldsymbol{R}^{n+1}_{i,j,k} \approx \boldsymbol{R}^{n}_{i,j,k} + \frac{\partial \boldsymbol{R}}{\partial \boldsymbol{U}} \Delta \boldsymbol{U}^{n}_{i,j,k} \tag{3.73}$$

Substituting the linearized residual into Eq. 3.72, the implicit scheme becomes

$$\left[\frac{\mathcal{V}_{i,j,k}}{\Delta t_{i,j,k}} + \left(\frac{\partial \boldsymbol{R}}{\partial \boldsymbol{U}} \right)_{i,j,k} \right] \Delta \boldsymbol{U}^{n}_{i,j,k} = -\boldsymbol{R}^{n}_{i,j,k} \tag{3.74}$$

The term on the left hand side of Eq. 3.74 is known as the implicit operator. The term on the right hand side is known as the explicit operator. The implicit operator is a sparse matrix with dimensions equal to the number of control volumes in the domain times the number of conservation variables in each control volume. To solve the system in Eq. 3.74, the implicit operator needs to be inverted, which can be done via matrix inversion or factorization. Due to the size of the implicit operator, direct

inversion is not practical so factorization is the preferred method. With factorization, the implicit operator is approximated by factors that can be solved more easily with iterative methods. Since the spatial accuracy of the solution is governed by the explicit operator only, the implicit operator can be approximated in any number of ways without affecting the steady-state solution. However, each approximation of the implicit operator degrades the stability and efficiency of the scheme.

Yoon and Jameson [104] developed what became known as the Lower-Upper Symmetric Gauss-Seidel (LU-SGS) method to solve the Euler equations implicitly. The implicit operator is factored so that the implicit scheme in Eq. 3.74 becomes

$$(\mathbf{D}+\mathbf{L})\,\mathbf{D}^{-1}\,(\mathbf{D}+\mathbf{U})\,\Delta\boldsymbol{U}^{n}_{i,j,k} = -\boldsymbol{R}^{n}_{i,j,k} \tag{3.75}$$

where $\mathbf{L}$ and $\mathbf{U}$ are the terms in the lower and upper triangular matrices of the implicit operator and $\mathbf{D}$ contains the diagonal terms. The system can be inverted in a forward and backward sweep, which are defined as

$$(\mathbf{D}+\mathbf{L})\,\Delta\boldsymbol{U}^{(1)} = -\boldsymbol{R}^{n}_{i,j,k} \tag{3.76}$$

$$(\mathbf{D}+\mathbf{U})\,\Delta\boldsymbol{U}^{n} = \mathbf{D}\Delta\boldsymbol{U}^{(1)} \tag{3.77}$$

The convective fluxes in the implicit operator are approximated using a first order accurate upwind extrapolation from neighboring cells. The flux Jacobian is split into positive and negative parts at each cell face of the control volume as shown in Fig. 3.5 for a 2-D case. The positive and negative Jacobians are formed using the positive and negative eigenvalues of the convective flux as in flux-vector splitting schemes. Thus, the operators in Eq. 3.75 are constructed from the positive and negative convective flux Jacobians, the viscous flux Jacobians, and the source term Jacobian. An excellent reference for constructing these terms is a DLR report by Blazek [10]. On structured

grids, the operators are expressed as

$$\mathbf{L} = \left(\mathbf{A}^{+} + \mathbf{A}_{v}\right)_{i-1,j,k} \Delta S_{i-1/2,j,k} \; + \; \left(\mathbf{A}^{+} + \mathbf{A}_{v}\right)_{i,j-1,k} \Delta S_{i,j-1/2,k} \; + \\ \left(\mathbf{A}^{+} + \mathbf{A}_{v}\right)_{i,j,k-1} \Delta S_{i,j,k-1/2} \tag{3.78}$$

$$\mathbf{U} = \left(\mathbf{A}^{-} - \mathbf{A}_{v}\right)_{i-1,j,k} \Delta S_{i-1/2,j,k} \; + \; \left(\mathbf{A}^{-} - \mathbf{A}_{v}\right)_{i,j-1,k} \Delta S_{i,j-1/2,k} \; + \\ \left(\mathbf{A}^{-} - \mathbf{A}_{v}\right)_{i,j,k-1} \Delta S_{i,j,k-1/2} \tag{3.79}$$

$$\mathbf{D} = \frac{\mathcal{V}_{i,j,k}}{\Delta t_{i,j,k}} \mathbf{I} + \left(\mathbf{A}^{-} - \mathbf{A}_{v}\right)_{i,j,k} \Delta S_{i-1/2,j,k} + \left(\mathbf{A}^{-} - \mathbf{A}_{v}\right)_{i,j,k} \Delta S_{i,j-1/2,k} + \\ \left(\mathbf{A}^{-} - \mathbf{A}_{v}\right)_{i,j,k} \Delta S_{i,j,k-1/2} + \left(\mathbf{A}^{+} + \mathbf{A}_{v}\right)_{i,j,k} \Delta S_{i+1/2,j,k} + \\ \left(\mathbf{A}^{+} + \mathbf{A}_{v}\right)_{i,j,k} \Delta S_{i,j+1/2,k} + \left(\mathbf{A}^{+} + \mathbf{A}_{v}\right)_{i,j,k} \Delta S_{i,j,k+1/2} - \left(\frac{\partial(\mathcal{V}\boldsymbol{S})}{\partial \boldsymbol{U}}\right)_{i,j,k} \tag{3.80}$$

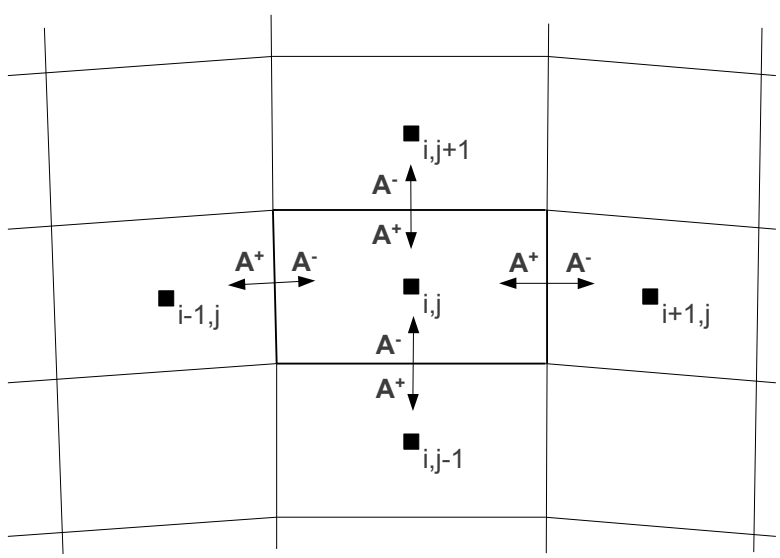

Figure 3.5: Split flux Jacobian definitions for LU-SGS operators in cell i, j

Fortunately, approximations for these Jacobians are possible to avoid excessive programming and computational time. Yoon and Jameson [104] approximate the

split convective Jacobians using

$$\mathbf{A}^{\pm}\Delta S = \frac{1}{2}\left(\mathbf{A}_c\Delta S \pm \omega\Lambda_c\mathbf{I}\right) \tag{3.81}$$

where ω is an overrelaxation parameter between 1 and 2. Higher values provide more stability, and lower numbers increase the convergence rate. The convective flux Jacobian, $\mathbf{A}_c$, in 2-D is defined

$$\mathbf{A}_c = \begin{bmatrix} -V_t & n_x & n_y & 0 \\ n_x\phi - uV & V - V_t - (\gamma-2)n_x u & n_y u - (\gamma-1)n_x v & (\gamma-1)n_x \\ n_y\phi - vV & n_x v - (\gamma-1)n_y u & V - V_t - (\gamma-2)n_y v & (\gamma-1)n_y \\ V(\phi - a_1) & n_x a_1 - (\gamma-1)uV & n_y a_1 - (\gamma-1)vV & \gamma V - V_t \end{bmatrix} \tag{3.82}$$

where

$$a_1 = \gamma E - \phi \ ; \quad V = n_x u + n_y v \ ; \quad \phi = \frac{1}{2}(\gamma-1)(u^2+v^2) \tag{3.83}$$

and V_t is the contravariant velocity of the cell face for a moving grid. The 3-D convective flux Jacobian takes a similar form and can be found in a paper by Pulliam and Steger [65]. The viscous flux Jacobians may be replaced by the viscous spectral radius as suggested by Sharov and Nakahashi [71]. Finally, only the diagonal terms from the source Jacobians are retained. These are found numerically using the formula

$$\frac{\partial S_i}{\partial U_i} = \frac{S_i(U_i+\epsilon) - S_i(U_i)}{\epsilon} \tag{3.84}$$

where the perturbation parameter is typically in the range $1.0^{-5} < \epsilon < 1.0^{-10}$.

In the LU-SGS method, the forward and backward sweeps are carried out along diagonal $i+j = const.$ lines in 2-D and $i+j+k = const.$ planes in 3-D. By sweeping in this manner, the off-diagonal terms in the $\mathbf{L}$ and $\mathbf{U}$ operators are known from an earlier part of the sweep. Returing to Eqs. 3.76 and 3.77, the LU-SGS scheme is

implemented according to

$$\mathbf{D}\Delta\boldsymbol{U}^{(1)}_{i,j,k} = -\boldsymbol{R}^{n}_{i,j,k} - \mathbf{L}\Delta\boldsymbol{U}^{(1)} \tag{3.85}$$

$$\mathbf{D}\Delta\boldsymbol{U}^{n}_{i,j,k} = \mathbf{D}\Delta\boldsymbol{U}^{(1)}_{i,j,k} - \mathbf{U}\Delta\boldsymbol{U}^{n} \tag{3.86}$$

where $\Delta\boldsymbol{U}^{(1)}$ and $\Delta\boldsymbol{U}^{n}$ are the calculated updates to the flow variables known from previous parts of the sweep. Since $\mathbf{D}$ is now only a diagonal matrix, the inversion of the $\mathbf{D}$ operator requires little computational work. Although a key feature of implicit time integration is unconditional stability, due to the approximations to the implicit operator, an upper limit on the CFL number now exists. Further, the approximations reduce the efficiency of the scheme so that the optimum CFL number is not necessarily the largest stable CFL number.

3.4 Discrete Boundary Conditions

3.4.1 Solid Wall

The boundary conditions at a solid wall are different for inviscid and viscous flows. For an inviscid flow, the velocity normal to the wall must be zero since the fluid is not allowed to penetrate the wall. In the case of a moving wall, the normal velocity of the fluid at the wall must equal the normal velocity of the wall. The convective fluxes at the wall reduce to only the pressure term in the momentum equations. The control volume faces on a solid surface can be treated differently to meet this requirement, or ghost cells can be judiciously chosen to meet the requirement without requiring a separate loop for wall fluxes. The second approach is used here.

The density and pressure across the wall are kept constant. This is easily accomplished with ghost cells. The density, for example, is prescribed in the first

two rows of ghost cells as

$$\rho_0 = \rho_1 \tag{3.87}$$

$$\rho_{-1} = \rho_2 \tag{3.88}$$

where the cell indexes are defined according to Fig. 3.6.

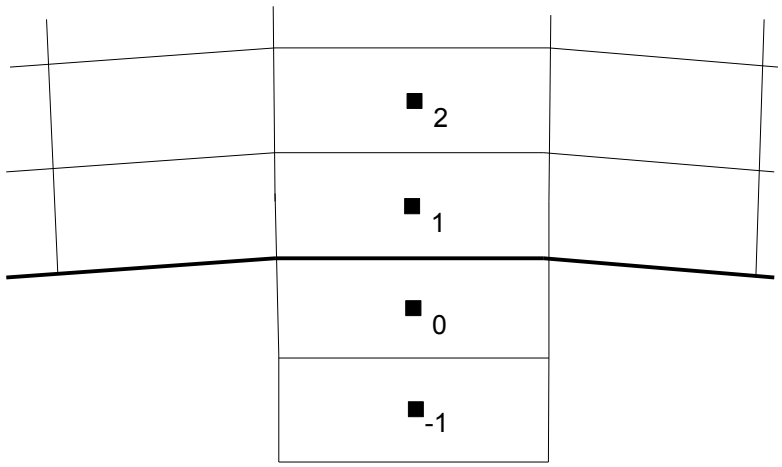

Figure 3.6: Wall adjacent and ghost cells at a solid boundary

The velocity ghost cells are more complicated. To determine the appropriate ghost cell values, the conserved values at the wall are first determined by extrapolation from the domain interior. For inviscid flows, the wall values are extrapolated as

$$\boldsymbol{U}_w = \frac{3}{2}\boldsymbol{U}_1 - \frac{1}{2}\boldsymbol{U}_2 \tag{3.89}$$

The normal velocity at the wall is easily determined with the unit normal vector at the wall. For a moving wall, the normal motion of the wall should be included so that the normal velocity can be written

$$V_{\text{normal}} = \left(u_w - \dot{f}\right)\eta_x + \left(v_w - \dot{g}\right)\eta_y + \left(w_w - \dot{h}\right)\eta_z \tag{3.90}$$

where $\dot{f}$, $\dot{g}$, and $\dot{h}$ are the Cartesian components of the wall motion. When the rotating frame of reference is used, the normal wall velocity is augmented according to

$$V_{\text{normal}} = \left(u_w - \dot{f} - \Omega z\right)\eta_x + \left(v_w - \dot{g}\right)\eta_y + \left(w_w - \dot{h} + \Omega x\right)\eta_z \tag{3.91}$$

The velocity in the first ghost cell can be related to the wall velocity and the first cell in the domain by taking the velocity at the wall as an average of the two, or equivalently

$$\boldsymbol{V}_0 = 2\boldsymbol{V}_w - \boldsymbol{V}_1 \tag{3.92}$$

The normal velocity at the wall must be removed from the wall velocity in order to satisfy the no penetration condition. The wall velocity is effectively the value extrapolated from the domain less the normal velocity component. Thus, the velocity components in the first row of ghost cells become

$$u_0 = 2\left(u_w - \eta_x V_{\text{normal}}\right) - u_1 \tag{3.93}$$

$$v_0 = 2\left(v_w - \eta_y V_{\text{normal}}\right) - v_1 \tag{3.94}$$

$$w_0 = 2\left(w_w - \eta_z V_{\text{normal}}\right) - w_1 \tag{3.95}$$

Applying the same approach for the second row of ghost cells, the velocity components are given by

$$u_{-1} = 2\left(u_w - \eta_x V_{\text{normal}}\right) - u_2 \tag{3.96}$$

$$v_{-1} = 2\left(v_w - \eta_y V_{\text{normal}}\right) - v_2 \tag{3.97}$$

$$w_{-1} = 2\left(w_w - \eta_z V_{\text{normal}}\right) - w_2 \tag{3.98}$$

For viscous flows, the no-slip condition is applied at solid surfaces, which means that the velocity at the wall must be zero. For a moving surface, the velocity should be that of the moving surface. The density is set the same as for the inviscid case. The energy condition at the wall is found by applying the adiabatic wall condition.

Since the wall is adiabatic, there is a zero temperature gradient normal to the wall, or $\frac{\partial T}{\partial \eta} = 0$. This implies that $T_0 = T_1$. Using the ideal gas law, the total energy in the first ghost cell becomes

$$(\rho E)_0 = \frac{p_0}{\gamma - 1} + \frac{1}{2}\left[(\rho u)_0^2 + (\rho v)_0^2 + (\rho w)_0^2\right]/\rho_0 \tag{3.99}$$

The velocity is less complicated than the inviscid case since the wall value now must either be zero on stationary grids or the value of the wall motion for moving grids. As before, the grid motion component must be augmented when using a rotating frame of reference. Using Eq. 3.92, the velocity components in the first and second rows of ghost cells are written as

$$u_0 = 2\left(\dot{f} - \Omega z\right) - u_1 \tag{3.100}$$

$$v_0 = 2\dot{g} - v_1 \tag{3.101}$$

$$w_0 = 2\left(\dot{h} + \Omega x\right) - w_1 \tag{3.102}$$

$$u_{-1} = 2\left(\dot{f} - \Omega z\right) - u_2 \tag{3.103}$$

$$v_{-1} = 2\dot{g} - v_2 \tag{3.104}$$

$$w_{-1} = 2\left(\dot{h} + \Omega x\right) - w_2 \tag{3.105}$$

The Spalart-Allmaras working variable, intermittency, and momentum thickness Reynolds number are all set to zero at a solid wall so they may be set according to

$$\tilde{\nu}_0 = -\tilde{\nu}_1 \tag{3.106}$$

$$\gamma_0 = -\gamma_1 \tag{3.107}$$

$$\left(\overline{\mathrm{Re}_{\theta t}}\right)_0 = -\left(\overline{\mathrm{Re}_{\theta t}}\right)_1 \tag{3.108}$$

Similar relationships are used to set the second row of ghost cells.

3.4.2 Far Field

Far field boundary conditions are often treated using characteristic variables since the governing equations are dominated by hyperbolic propagation [32, 17, 81]. One-dimensional flow is typically analyzed with results that are easily extended to higher dimensions. The eigenvalues of the convective flux Jacobian are given as

$$\lambda = \begin{bmatrix} \lambda_1 \\ \lambda_2 \\ \lambda_3 \end{bmatrix} = \begin{bmatrix} u - c \\ u \\ u + c \end{bmatrix} \tag{3.109}$$

The eigenvalues represent acoustic and entropy waves. For a boundary node subject to subsonic inflow, the situation is depicted in Fig. 3.7. The left running acoustic wave leaves the domain, and the right running acoustic wave and an entropy wave enter the domain. The situation is reversed for subsonic outflow. For supersonic inflow, all waves enter the domain, and for supersonic outflow, all waves exit the domain.

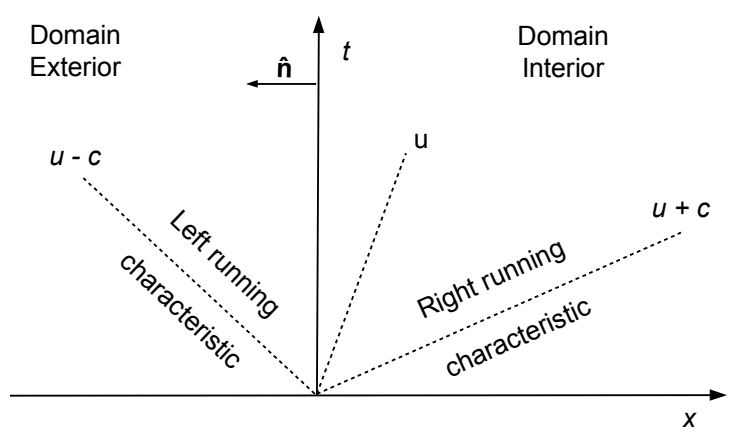

Figure 3.7: Characteristics at subsonic inflow boundary

Characteristic equations may be defined from the left eigenvectors of the eigenvalues in Eq. 3.109 as

$$dp + \rho c du = 0 \tag{3.110}$$

$$dp - c^2 d\rho = 0 \tag{3.111}$$

$$dp - \rho c du = 0 \tag{3.112}$$

The Riemann invariants are recovered by integrating Eqs. 3.110 and 3.112

$$R^+ = u + \int \frac{dp}{\rho c} \tag{3.113}$$

$$R^- = u - \int \frac{dp}{\rho c} \tag{3.114}$$

The expressions are simplified using $\rho = \gamma p/c^2$ and $p = k_1 c^{2\gamma/\gamma-1}$ for a calorically perfect gas so that the Riemann invariants become

$$R^+ = u + \frac{2c}{\gamma - 1} \tag{3.115}$$

$$R^- = u - \frac{2c}{\gamma - 1} \tag{3.116}$$

Combining the two equations, expressions for the velocity and speed of sound at the domain boundary are now determined as

$$u = \frac{1}{2}\left(R^+ + R^-\right) \tag{3.117}$$

$$c = \frac{\gamma - 1}{4}\left(R^+ + R^-\right) \tag{3.118}$$

The remaining characteristic equation, Eq. 3.111, is integrated directly to give

$$\frac{p}{\rho^\gamma} = constant \tag{3.119}$$

Table 3.2: Far Field Boundary Conditions

Case	Condition	R^+	R^-	s	v or w
1	subsonic inflow	free stream	extrapolated	free stream	free stream
2	subsonic outflow	extrapolated	free stream	extrapolated	extrapolated
3	supersonic inflow	free stream	free stream	free stream	free stream
4	supersonic outflow	extrapolated	extrapolated	extrapolated	extrapolated

Equation 3.119 implies that entropy is constant along the characteristic line. For convenience, entropy is defined using Eq. 3.119, which has the same functional dependence as the actual entropy relation

$$\frac{p}{\rho^\gamma} = k_1 e^{s/c_v} \tag{3.120}$$

For one-dimensional flow, Eqs. 3.117-3.119 may be used to define the flow conditions at the far field boundary. For 2-D and 3-D flow, the new coordinate directions add tangential velocity components to the solution. The tangential velocity is constant across the Riemann invariant waves so this condition can be added to Eqs. 3.117-3.119 as the far field boundary conditions. All flow conditions can be determined from these relations at the boundary.

Recall that for one-dimensional subsonic inflow, two waves enter the domain and one exits. If each wave is thought to carry one piece of information about a conserved or primitive variable, then for this case two free stream variables should be specified that determine the solution inside the domain. The variable exiting the domain changes as the solution in the domain changes. Thus, the third variable is extrapolated at each time step from the domain interior. For 2-D or 3-D flow, the tangential velocity follows the constant entropy wave with respect to entering and exiting the domain. Table 3.2 is constructed to show the free stream and extrapolated boundary conditions for each of four possible conditions at the boundary.

3.4.3 Coordinate Cut

Structured grids contain an artificial boundary or cut where the grid connects to itself (see Fig. 3.1). This boundary is easily handled using ghost cells. The cells on either side of the cut correspond to real cells in the domain. Ghost cells are defined on both sides of the cut with values set equal to the corresponding cells in the domain. For a cell-centered scheme, no further attention is required at a coordinate cut.

3.4.4 Periodic Boundary

For rotating flows, periodic boundary conditions are utilized to decrease the computational grid size to that spanning a single blade. Scalar quantities such as density and pressure are matched at periodic sides of the domain. Vector quantities such as velocity are transformed via the rotation matrix at periodic boundaries. For rotation about the y-axis, the rotation matrix is given by

$$\mathbf{R} = \begin{bmatrix} \cos\phi & 0 & \sin\phi \\ 0 & 1 & 0 \\ -\sin\phi & 0 & \cos\phi \end{bmatrix} \tag{3.121}$$

where ϕ is the angle between the edges of the two periodic boundaries. Thus, the transformed velocity at periodic edge B is related to periodic edge A according to

$$\boldsymbol{V}_B = \mathbf{R}\boldsymbol{V}_A \tag{3.122}$$

3.5 Convergence Acceleration Techniques

Four techniques to accelerate steady-state convergence are presented in this section. Local time stepping, multigrid, and low speed preconditioning are applicable to explicit and implicit time integration. Residual smoothing is only applicable to explicit time integration.

3.5.1 Local Time Stepping

Convergence to steady-state may be accelerated by using the largest perimissible time step for each control volume rather than a global time step. This approach destroys the time accuracy of the transient solution, but since the harmonic balance method relies only on steady-state solutions to reconstruct the unsteady periodic solution, it is not necessary to preserve time accuracy.

3.5.2 Residual Smoothing

Residual smoothing was conceived as a way to increase the maximum CFL number by giving an implicit flavor to an explicit scheme. The idea was first explored by Jameson and Baker [36]. They proposed replacing the residual at each point by a weighted average of residuals from neighboring points. The most popular method became known as implicit residual smoothing. In the i-direction, the formula is written

$$-\epsilon^i \boldsymbol{R}^*_{i-1,j,k} + \left(1 + 2\epsilon^i\right) \boldsymbol{R}^*_{i,j,k} - \epsilon^i \boldsymbol{R}^*_{i+1,j,k} = \boldsymbol{R}_{i,j,k} \tag{3.123}$$

where $\boldsymbol{R}^*_{i,j,k}$ is the smoothed residual. Similar equations are written for the j- and k-directions. Equation 3.123 forms an implicit system of equations that must be inverted numerically. The smoothing coefficients ϵ^i, ϵ^j, and ϵ^k are defined as functions of the spectral radii of the convective flux Jacobians and the viscous spectral radii. Various formulations are provided in Turkel et al. [90].

3.5.3 Multigrid

Multigrid greatly reduces computation time by solving the governing equations on successively coarser grids. The solution on the fine grid is updated by coarse grid approximations. Multigrid was originally developed by Achi Brandt for elliptic partial differential equations [14]. However, Jameson was the first to apply the method to the Euler equations [35]. Multigrid has since been applied to the Navier-Stokes equations

by many authors. The idea behind multigrid is that coarse grid corrections can be used to drive the fine grid solution faster to steady-state. The coarser grids allow larger time steps due to the larger control volumes and also require less work since there are fewer cells to compute the solution. Moreover, low frequency errors on the fine grid that hinder convergence become high frequency errors on coarse grids that can be quickly damped.

A simple multigrid cycle is illustrated in (Fig. 3.8). A series of successively coarser grids are created by skipping every other node in each coordinate direction on each grid. The finest grid is designated as h. The next three grids are $2h$, $4h$, and $8h$ with increasing coarseness. This three level multigrid cycle is known as a V-cycle owing to the shape of Fig. 3.8.

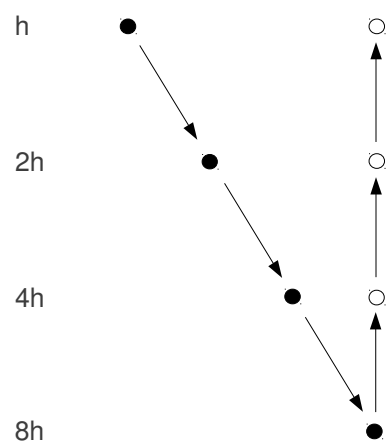

Figure 3.8: Multigrid V-cycle. Symbols designate: • solve equations and restrict solution and ∘ prolongate corrections.

The multigrid cycle starts by transferring the fine grid solution and residual to the next coarser grid. An interpolation operator is used to control the solution transfer. This operation may be written as

$$\boldsymbol{U}_{2h}^{(0)} = \hat{I}_h^{2h} \boldsymbol{U}_h^{n+1} \tag{3.124}$$

where $\hat{I}_h^{2h}$ is the interpolation operator. For a cell-centered scheme, the solution on the coarse grid is simply a volume weighted interpolation of the fine grid cells comprising a coarse grid cell. In 2-D, the solution interpolation becomes

$$\left(\boldsymbol{U}_{2h}^{(0)}\right)_{i,j} = \frac{(\boldsymbol{U}_h^{n+1})_{i,j}\mathcal{V}_{i,j} + (\boldsymbol{U}_h^{n+1})_{i+1,j}\mathcal{V}_{i+1,j} + (\boldsymbol{U}_h^{n+1})_{i,j+1}\mathcal{V}_{i,j+1}}{\mathcal{V}_{i,j} + \mathcal{V}_{i+1,j} + \mathcal{V}_{i,j+1} + \mathcal{V}_{i+1,j+1}} + \frac{(\boldsymbol{U}_h^{n+1})_{i+1,j+1}\mathcal{V}_{i+1,j+1}}{\mathcal{V}_{i,j} + \mathcal{V}_{i+1,j} + \mathcal{V}_{i,j+1} + \mathcal{V}_{i+1,j+1}} \tag{3.125}$$

The fine grid residual is sent to the coarse grid via a restriction operator, I_h^{2h}. For a cell-centered scheme, the restriction is just a summation of the residuals from the fine grid cells comprising a coarse grid cell. The idea is depicted in Fig. 3.9. In mathematical form, the restriction operator is written as

$$\left(I_h^{2h}\boldsymbol{R}_h^{n+1}\right)_{i,j} = \left(\boldsymbol{R}_h^{n+1}\right)_{i,j} + \left(\boldsymbol{R}_h^{n+1}\right)_{i+1,j} + \left(\boldsymbol{R}_h^{n+1}\right)_{i,j+1} + \left(\boldsymbol{R}_h^{n+1}\right)_{i+1,j+1} \tag{3.126}$$

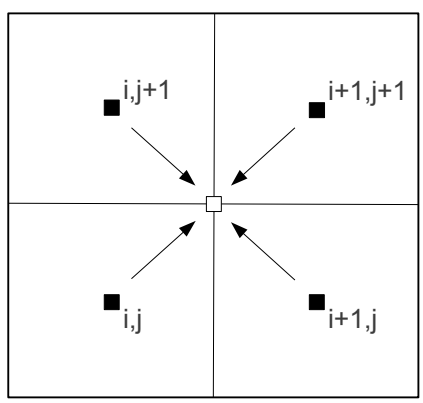

Figure 3.9: Restriction of residual to coarse grid.

To retain the accuracy of the fine grid solution on a coarse grid, a forcing function is used, which is the difference between the fine grid residual and the residual computed on the coarse grid from the initial approximation, $\boldsymbol{U}_{2h}^{(0)}$. The forcing function takes

the form

$$(\boldsymbol{Q}_F)_{2h} = I_h^{2h} \boldsymbol{R}_h^{n+1} - \boldsymbol{R}_{2h}^{(0)} \tag{3.127}$$

where $\boldsymbol{R}_{2h}^{(0)}$ is the residual on the coarse grid from the initial coarse grid approximation. Care must be taken when defining the forcing function on successively coarser grids since the accuracy from the finest grid must remain unchanged. This is accomplished by retaining the forcing function from the previous grid. The forcing function on the $4h$ grid, for example, is written as

$$(\boldsymbol{Q}_F)_{4h} = I_{2h}^{4h} \left[\boldsymbol{R}_{2h}^{n+1} + (\boldsymbol{Q}_F)_{2h} \right] - \boldsymbol{R}_{4h}^{(0)} \tag{3.128}$$

The solution on a coarse grid can be obtained using the same time integration scheme as on the fine grid. However, the coarse grid residual is formed from the usual convective and viscous fluxes and the forcing function. Thus, the residual on the coarse grid is given by

$$(\boldsymbol{R}_F)_{2h} = \boldsymbol{R}_{2h} + (\boldsymbol{Q}_F) \tag{3.129}$$

Using the multistage scheme from before, the coarse grid solution can be obtained from

$$\boldsymbol{U}_{2h}^{(k)} = \boldsymbol{U}_{2h}^{(0)} - \alpha_k \frac{\Delta t_{2h}}{\mathcal{V}_{2h}} \left[\boldsymbol{R}_{2h}^{(k-1)} + (\boldsymbol{Q}_F)_{2h} \right] \tag{3.130}$$

where $1 < k < m$ and m is the number of stages in the scheme. Since the final accuracy of the solution is unaffected by the accuracy of the solution on coarse grids, lower order schemes are typically used on coarse grids for computational efficiency.

The correction on the coarse grid is the difference between the solution obtained on the coarse grid and the initial approximation, or

$$\delta \boldsymbol{U}_{2h} = \boldsymbol{U}_{2h}^{n+1} - \boldsymbol{U}_h^{(0)} \tag{3.131}$$

The coarse grid correction is interpolated to the next finer grid using

$$\boldsymbol{U}_h^+ = \boldsymbol{U}_h^{n+1} + I_{2h}^h \delta \boldsymbol{U}_{2h} \tag{3.132}$$

where I_{2h}^h is the prolongation operator. Prolongation can be accomplished in a few ways for a cell-centered scheme, but a simple zeroth order prolongation is achieved if the coarse grid residual is sent to the constituent fine grid cells. In 2-D, the solution on the fine grid in cell $i+1, j$ becomes

$$\left(\boldsymbol{U}_h^+\right)_{i+1,j} = \left(\boldsymbol{U}_h^{n+1}\right)_{i+1,j} + \left(\delta \boldsymbol{U}_{2h}\right)_{i,j} \tag{3.133}$$

The fine grid cells defined by i, j, $i, j{+}1$, and $i{+}1, j{+}1$ have a similar form. Figure 3.10 shows this simple prolongation.

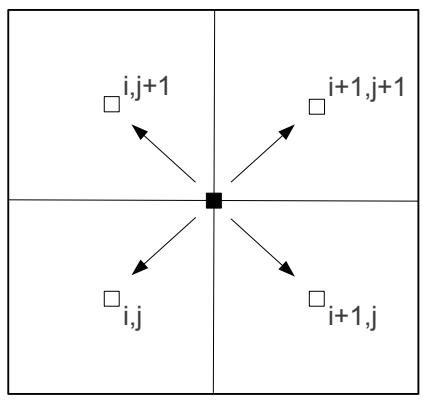

Figure 3.10: Zeroth order prolongation of coarse grid correction to finer grid.

3.5.4 Low Speed Preconditioning

The governing equations become stiff as the Mach number tends towards zero and density becomes constant. The reason is that the convective waves, traveling at speed u, are much slower than the acoustic waves, traveling at $u + c$. This disparity leads

to slower convergence rates for incompressible flows and even decreased accuracy for flows as the Mach number becomes less than 0.1.

The time derivatives in the governing equations can be multiplied by a preconditioning matrix to remove the stiffness from the system. This preconditioning matrix changes the eigenvalues of the system so that the acoustic wave speeds are more on the order of the convective wave speeds. A variety of preconditioning matrices are presented in the literature, including those of Turkel [87, 89], Choi and Merkle [19], van Leer and Lee [96], and Weiss and Smith [99]. All have had varying degrees of success along with limitations, and thus, no single preconditioner has turned into an accepted CFD standard.

To motivate the development of the preconditioning matrix, consider the 2-D Euler equations. Using primitive variables, these are written as

$$\frac{\partial \boldsymbol{U}_0}{\partial t} + \frac{\partial \boldsymbol{F}_0}{\partial x} + \frac{\partial \boldsymbol{G}_0}{\partial y} = 0 \tag{3.134}$$

where

$$\boldsymbol{U}_0 = \begin{bmatrix} p \\ u \\ v \\ S \end{bmatrix} \quad ; \quad \boldsymbol{F}_0 = \begin{bmatrix} u\left(p + \rho c^2\right) \\ u^2 + p/\rho \\ uv \\ uS \end{bmatrix} \quad ; \quad \boldsymbol{G}_0 = \begin{bmatrix} v\left(p + \rho c^2\right) \\ v^2 + p/\rho \\ uv \\ vS \end{bmatrix} \tag{3.135}$$

The dependent variables are chosen as the non-conservative set $\boldsymbol{U}_0$ to simplify the derivation. A matrix transformation will be applied later to switch back to conservative variables. The Euler equations may be recast in quasi-linear form by using the flux Jacobian matrices, or

$$\frac{\partial \boldsymbol{U}_0}{\partial t} + \mathbf{A}_0 \frac{\partial \boldsymbol{U}_0}{\partial x} + \mathbf{B}_0 \frac{\partial \boldsymbol{U}_0}{\partial y} = 0 \tag{3.136}$$

where

$$\mathbf{A}_0 = \begin{bmatrix} u & \rho c^2 & 0 & 0 \\ 1/\rho & u & 0 & 0 \\ 0 & 0 & u & 0 \\ 0 & 0 & 0 & u \end{bmatrix} \quad ; \quad \mathbf{B}_0 = \begin{bmatrix} v & 0 & \rho c^2 & 0 \\ 0 & v & 0 & 0 \\ 1/\rho & 0 & v & 0 \\ 0 & 0 & 0 & v \end{bmatrix} \tag{3.137}$$

The preconditioner, $\mathbf{P}^{-1}$, is applied to the time dependent terms to scale the acoustic wave speeds to the convective wave speeds. Applied to the quasi-linear form in Eq. 3.136, the preconditioned equations become

$$\mathbf{P}_0^{-1}\frac{\partial \boldsymbol{U}_0}{\partial t} + \mathbf{A}_0\frac{\partial \boldsymbol{U}_0}{\partial x} + \mathbf{B}_0\frac{\partial \boldsymbol{U}_0}{\partial y} = 0 \tag{3.138}$$

Equivalently, the inverse of the preconditioner can multiply the flux Jacobian matrices so that

$$\frac{\partial \boldsymbol{U}_0}{\partial t} + \mathbf{P}_0\mathbf{A}_0\frac{\partial \boldsymbol{U}_0}{\partial x} + \mathbf{P}_0\mathbf{B}_0\frac{\partial \boldsymbol{U}_0}{\partial y} = 0 \tag{3.139}$$

where Turkel's preconditioner is given by

$$\mathbf{P}_0^{-1} = \begin{bmatrix} c^2/\beta^2 & 0 & 0 & 0 \\ 0 & 1 & 0 & 0 \\ 0 & 0 & 1 & 0 \\ 0 & 0 & 0 & 1 \end{bmatrix} \quad ; \quad \mathbf{P}_0 = \begin{bmatrix} \beta^2/c^2 & 0 & 0 & 0 \\ 0 & 1 & 0 & 0 \\ 0 & 0 & 1 & 0 \\ 0 & 0 & 0 & 1 \end{bmatrix} \tag{3.140}$$

and the preconditioning parameter is defined by

$$\beta^2 = \min\left[\max\left(K_1\left(u^2+v^2\right)\left(1+\frac{1-M_0^2}{M_0^4}M^2\right), K_2\left(u_\infty^2+v_\infty^2\right)\right), c^2\right] \tag{3.141}$$

Here, M_0 is some cutoff Mach number where preconditioning should be turned off. This number should be near unity to avoid difficulties near shocks. The parameters K_1 and K_2 are free parameters. K_1 is typically in the range of 1.0-1.1, and K_2 is usually less than 1.0 for inviscid flows and may be as high as 5.0 for viscous flows.

Due to preconditioning, the eigenvalues of the system are now a function of $\mathbf{P}_0\mathbf{A}_0$ and $\mathbf{P}_0\mathbf{B}_0$ instead of $\mathbf{A}_0$ and $\mathbf{B}_0$, and thus, the characteristics of the system are changed. The eigenvalues for the matrix $\mathbf{P}_0\mathbf{A}_0$ are given by

$$\lambda_0 = \lambda_1 = u \tag{3.142}$$

$$\lambda_2 = \frac{1}{2}\left[zu - \sqrt{z^2u^2 + 4\beta^2\left(1 - \frac{u^2}{c^2}\right)}\right] \tag{3.143}$$

$$\lambda_3 = \frac{1}{2}\left[zu + \sqrt{z^2u^2 + 4\beta^2\left(1 - \frac{u^2}{c^2}\right)}\right] \tag{3.144}$$

where

$$z = 1 - \alpha + \frac{\beta^2}{c^2} \tag{3.145}$$

The eigenvalues for $\mathbf{P}_0\mathbf{B}_0$ take a similar form. An important observation is that the two acoustic eigenvalues are of the form $u' \pm c'$, which reduces to the familiar $u \pm c$ when $\beta^2 = c^2$. Taking $\beta^2 = c^2$ corresponds to the case of no preconditioning, and thus, preconditioning scales the acoustic waves while maintaining their form. It is also noted that the eigenvalues are invariant under variable transformations so that the eigenvalues remain the same for the conservation form of the Euler equations or other primitive formulations. To convert the preconditioner to conservative form, the transformations in Turkel et al. [91, 89] may be used so that

$$\mathbf{P}_c = \frac{\partial \boldsymbol{U}_c}{\partial \boldsymbol{U}_0}\mathbf{P}_0\frac{\partial \boldsymbol{U}_0}{\partial \boldsymbol{U}_c} \tag{3.146}$$

where the subscript c is added to reinforce a conservative variable formulation.

One of the major challenges in low speed preconditioning is correctly scaling the artificial dissipation. It is known that the artificial dissipation scales poorly as the Mach number goes to zero in the non-preconditioned system. Turkel et al. [88] showed that a necessary condition for convergence, as the Mach number approaches zero, is

that the dissipation scale in the x-direction according to

$$\boldsymbol{U}_x^{-1}\left|\boldsymbol{U}_x A\right| \sim \begin{pmatrix} O\left(1/M^2\right) & O\left(1/M\right) & O\left(1/M\right) & O\left(1\right) \\ O\left(1/M\right) & O\left(1\right) & O\left(1\right) & O\left(1\right) \\ O\left(1/M\right) & O\left(1\right) & O\left(1\right) & O\left(1\right) \\ O\left(1\right) & O\left(1\right) & O\left(1\right) & O\left(1\right) \end{pmatrix} \tag{3.147}$$

Similar scaling is needed in all other directions. Since the artificial dissipation is based on the eigenvalues of the convective flux Jacobians, it must be modified to reflect the new eigenvalues of the preconditioned system. In a general form, the preconditioned artificial dissipation can be represented for the JST flux as

$$\boldsymbol{D}_{i+1/2,j} = \mathbf{P}^{-1}|\sigma(\mathbf{PA})|_{i+1/2,j} \tag{3.148}$$

where σ is the spectral radius of the preconditioned system. For the Roe flux, the dissipation becomes

$$|\mathbf{A}_{Roe}|_{i+1/2,j} = \mathbf{P}^{-1}|\mathbf{PA}_{Roe}|_{i+1/2,j} \tag{3.149}$$

A particularly useful resource for programming the preconditioned Roe flux is given by Guillard and Viozat [29].

Chapter 4

Numerical Approach for Structural Solver

4.1 Conversion to Frequency Domain

The governing structural dynamics equation is also non-dimensionalized. Caution must be exercised in using a non-dimensional form compatible with the flow solver since the generalized force from the flow solver is used as an input into the structural model. One possible non-dimensionalization is [34]

$$\phi^{T*} = \phi^T \ ; \quad F^* = \frac{F}{\rho_\infty U_\infty^2 L_{ref}^2} \ ; \quad m_j^* = \frac{m_j}{\bar{m}} \tag{4.1}$$

$$t^* = t\omega_\alpha \ ; \quad q^* = \frac{q}{L_{ref}} \tag{4.2}$$

Inserting these relationships into Eq. 2.86, the governing equation becomes

$$L_{ref}\omega_\alpha^2 \frac{d^2 q_j^*}{dt^{*2}} + L_{ref}\omega_j^2 q_j^* = \frac{\phi_j^{T*}}{m_j^* \bar{m}} F_j^* \rho_\infty U_\infty^2 L_{ref} \tag{4.3}$$

Using the definitions of reduced mass, $\mu = \bar{m}/\rho_\infty \bar{V}$, and reduced velocity, $V_f = U_\infty/\sqrt{\mu}\omega_\alpha b_s$, the desired form of the governing equation is

$$\frac{d^2 q_j^*}{dt^{*2}} + \frac{1}{V_f^2}\left(\frac{\omega_j}{\omega_\alpha}\right)^2 q_j^* = \frac{\phi_j^{T*}}{m_j^*} F_j^* \frac{b_s^2 L_{ref}}{\bar{V}} \tag{4.4}$$

The harmonic balance approach employed in the flow solver enables direct determination of the unsteady aerodynamic force in the governing structural equation. Thus, it is convenient to work directly with the structural dynamics equation written in the frequency domain. To begin, harmonically varying excitations of the modal displacements are assumed. In non-dimensional form, these excitations appear as

$$q_j^* = \xi_j e^{i\frac{\omega}{\omega_\alpha}t^*} \tag{4.5}$$

Since ξ is already dimensionless, the * is omitted for brevity. It should also be noted that ξ is complex. The aerodynamic loading must also be converted to the frequency domain, and it takes a similar form according to

$$F_j^* = \bar{F}_j^* e^{i\frac{\omega}{\omega_\alpha}t^*} \tag{4.6}$$

Substituting these relationships into Eq. 4.4 and simplifying, the governing equation becomes

$$\frac{m_j^* \bar{V}}{b_s^2 L_{ref}}\left[-\mu\bar{\omega}^2\delta_{ij} + \frac{1}{V_f^2}\left(\frac{\omega_j}{\omega_\alpha}\right)^2\right]\xi_j = C_{Q_j} \tag{4.7}$$

where

$$C_{Q_j} = \frac{1}{\rho_\infty U_\infty^2 L_{ref}^2}\left(\iint_A \bar{p}_1 \phi_j^* \hat{\mathbf{n}} \cdot d\mathbf{A} + \iint_A \bar{\tau}_1 \phi_j^* \cdot d\mathbf{A}\right)$$

Here, C_Q is defined as the non-dimensional generalized force, and $\bar{p}_1$ and $\bar{\tau}_1$ are the first harmonics of the unsteady pressure and shear stress, respectively. Defining $k_w = \bar{V}/b_s^2 c_r \bar{m}$ and letting $L_{ref} = c_r$, the final form of the governing structural equation is

recovered

$$k_w m_j \left[-\mu\bar{\omega}^2\delta_{ij} + \frac{1}{V_f^2}\left(\frac{\omega_j}{\omega_\alpha}\right)^2 \right] \xi_j = C_{Q_j} \tag{4.8}$$

4.2 Aeroelastic Solution Technique

In this work, the flutter onset point is considered. The flutter solution corresponds to small amplitude harmonic motions that are neutrally stable. Because of the small amplitude assumption, the generalized aerodynamic forces can be determined through a linear analysis that requires the use of only a single harmonic for the CFD solutions [60]. In the case of a linear approximation the generalized force vector C_{Q_j} can be written as

$$C_{Q_j} = G_{ij}(\bar{\omega})\xi_j \tag{4.9}$$

where $G_{ij}(\bar{\omega})$ is the matrix of aerodynamic transfer functions[59]. If two structural mode shapes are included in an analysis, then G_{ij} would be written as

$$\mathbf{G} = \begin{bmatrix} G_{11} & G_{12} \\ G_{21} & G_{22} \end{bmatrix} \tag{4.10}$$

The elements in G_{ij} can be thought of as sensitivities of each mode shape to an excitation of a given mode shape. For example, G_{12} represents the sensitivity of first mode shape to an excitation of the second mode shape. Inserting Eq. (4.9) into Eq. (4.8) one gets

$$\left[k_w m_j \left(-\bar{\omega}^2\mu\delta_{ij} + \frac{1}{V_f^2}\left(\frac{\omega_j}{\omega_\alpha}\right)^2 \right) - G_{ij}(\bar{\omega}) \right] \xi_j = 0 \tag{4.11}$$

The flutter condition is obtained when the determinant of the matrix in the equation above is zero. To determine the flutter condition (if one exists), one can vary the value of $\bar{\omega}$, which is positive and purely real, and determine the value of V_f

that would satisfy

$$\left| k_w m_j \left(-\bar{\omega}^2 \mu \delta_{ij} + \frac{1}{V_f^2} \left(\frac{\omega_j}{\omega_\alpha} \right)^2 \right) - G_{ij}(\bar{\omega}) \right| = 0 \tag{4.12}$$

The flutter frequency and the corresponding flutter speed, V_f, is determined when V_f also becomes purely real.

Chapter 5

Validation Studies

Validation of the flow solver and aeroelastic solver are considered in this chapter. The chapter begins with validation of the 2-D flow solver. A steady flat plate and a steady Aerospatiale-A airfoil case are used to inspect the turbulence and transition modeling. An oscillating NACA 64A010 airfoil is examined to validate the harmonic balance implementation. The 3-D flow solver is validated with the steady ONERA M6 wing. The Caradonna-Tung rotor in hover is used to validate the rotating frame of reference 3-D flow solver, and a cylinder in crossflow is used to check the harmonic balance implementation in 3-D. Finally, the aeroelastic solver is validated in 3-D by studying the AGARD 445.6 wing.

5.1 Steady Flat Plate

The turbulent flat plate problem is used to verify the flow solver by comparison with results from CFL3D. CFL3D is a structured, cell-centered solver developed at NASA Langley Research Center in the 1980s. In the present case, turbulent flow is simulated along a flat plate with length $L = 2$ and Mach number $M = 0.2$. Although this could be classified as an incompressible problem, compressibility effects are included. The Reynolds number based on length is Re = 5 million at $x = 1$ and Re = 10 million at $x = 2$. It is also noted that at the far field, $\tilde{\nu} = 3\nu_\infty$ is used, where ν_∞ is the far field

kinematic viscosity. The CFL3D results presented here use a rectangular 545 x 385 grid with the plate adjacent to the bottom of the domain.

A C-grid with 577 x 257 nodes is used with the current solver (Fig. 5.1). The grid extends over 1 plate length in all directions. The grid spacing at the wall is $y^+ = 0.1$ which is the same as the CFL3D grid. However, this grid only contains 256 nodes on the upper plate surface compared to 449 in the CFL3D grid. As the results will indicate, this resolution is sufficient.

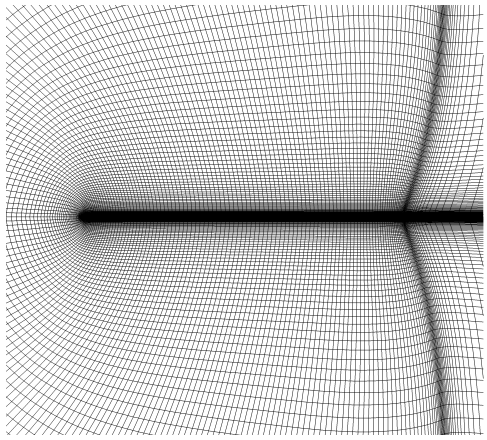

Figure 5.1: 577 x 257 flat plate C-grid.

The boundary layer quantities are of particular interest since it is here that the effects of turbulence are significant. The skin friction along the upper surface of the flat plate is compared for the two solvers in Fig. 5.2. As can be seen, the solutions only differ significantly near the leading and trailing edges. The more pronounced singular behavior in the current results are believed to stem from the difficulty in creating a C-grid type mesh around a flat plate with vanishing thickness.

Turbulence related quantities at $x = 0.97$ are also compared in Fig. 5.2. The ratio of the eddy viscosity to the free stream viscosity, μ_T/μ_∞, for the two solvers are nearly the same with a small disagreement towards the edge of the boundary layer. The grid used in the current study becomes much coarser than the CFL3D grid in this region, and it is almost certainly the reason for the disagreement. The law of the

wall and velocity profile in the boundary layer from CFL3D and the current solver are nearly identical.

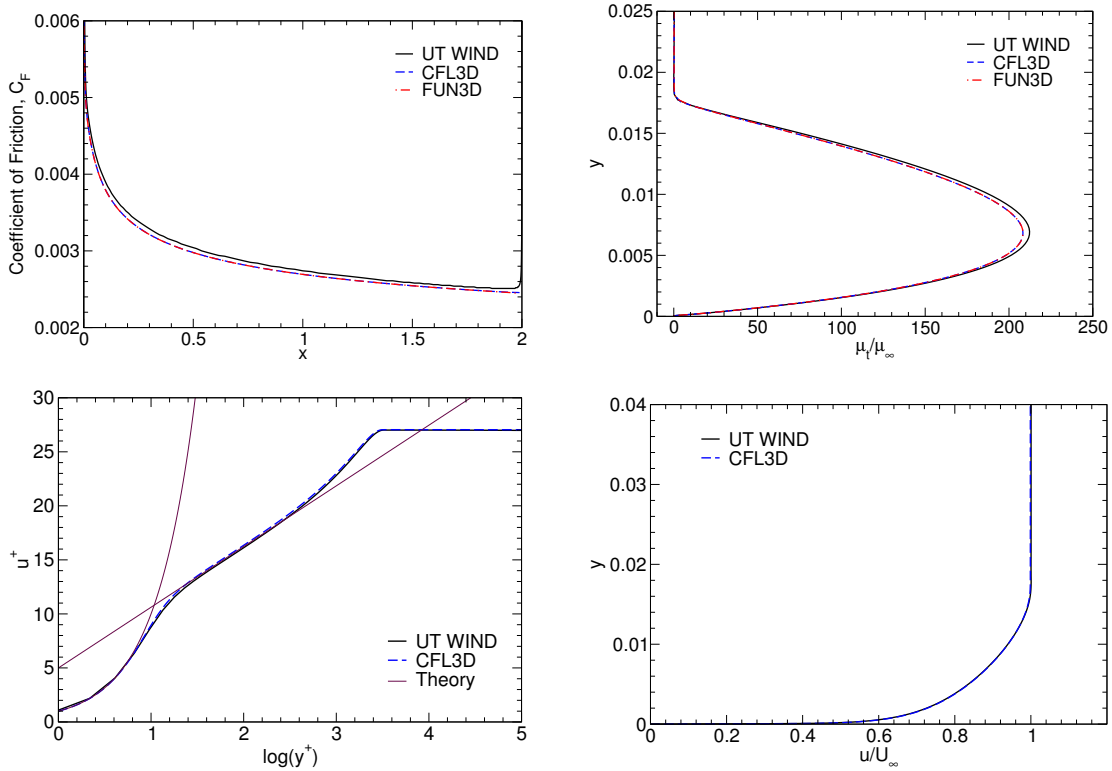

Figure 5.2: Boundary layer quantities for a flat plate with Re = 5 million at $x = 1$ and $M = 0.2$. **Top Left**: Skin friction along the upper surface. **Top Right**: Ratio of eddy viscosity to free stream viscosity at $x = 0.97$. **Bottom Left**: Law of the wall at $x = 0.97$. **Bottom Right**: Velocity profile at $x = 0.97$.

The predicted non-dimensional eddy viscosity along the entire plate is also compared for the two solvers. Referring to Fig. 5.3, the two solvers produce very similar contours along the plate surface. The results of this section confirm the correct implementation of the Spalart-Allmaras turbulence model in the flow solver.

5.2 Steady Aerospatiale-A Airfoil

The Aerospatiale-A airfoil has been used as a benchmark in the development of the $\gamma-\overline{\mathrm{Re}_{\theta t}}$ transition model since it requires the prediction of separation-induced transition

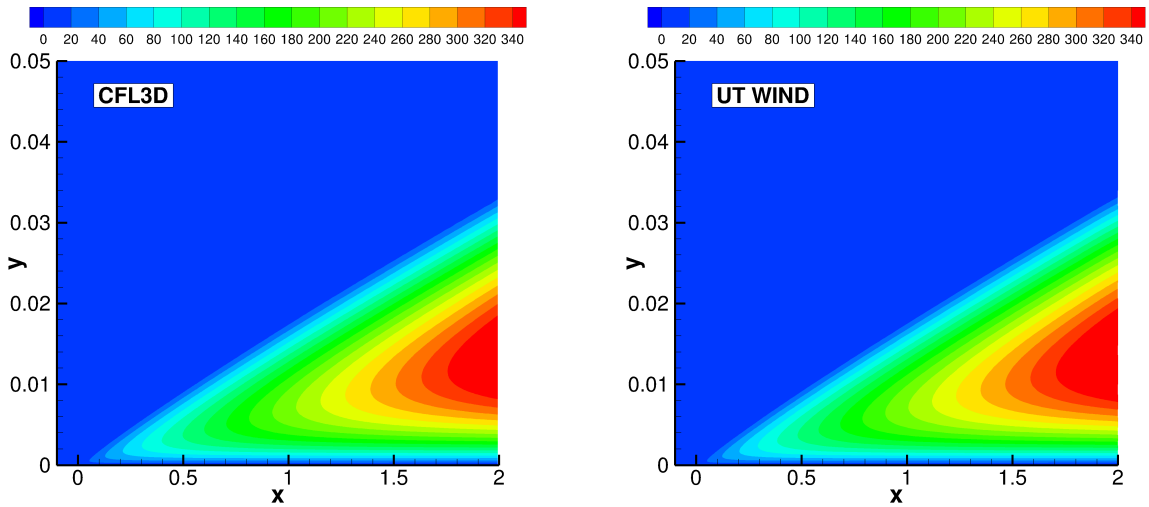

Figure 5.3: Ratio of the turbulent eddy viscosity to the free stream viscosity for a flat plate with Re = 5 million at $x = 1$. **Left:** CFL3D. **Right:** Current solver.

[39, 54]. The free stream Mach number is taken to be 0.15, the Reynolds number 2.1 million, and the angle of attack 13.1°. The grid used for this case is the 321 x 129 C-grid shown in Fig. 5.4 with a wall spacing of $y^+ = 0.1$. The turbulence intensity is taken to be 0.05%, which was also used by Medida and Baeder [54]. This is a typical value in a low-turbulence wind tunnel such as that used for this experimental dataset.

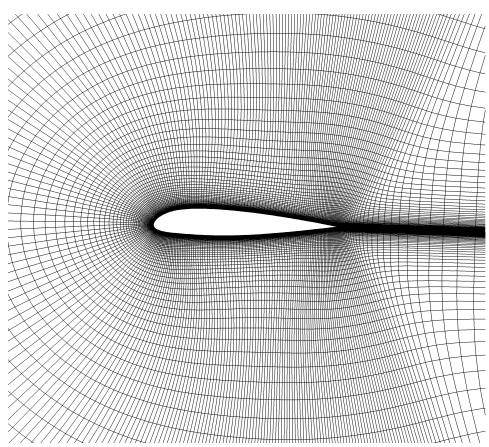

Figure 5.4: 321 x 129 Aerospatiale-A C-grid.

The intermittency, γ, controls the production of turbulent kinetic energy in order to properly initiate transition. The momentum thickness Reynolds number, $\overline{\mathrm{Re}_{\theta t}}$,

determines the onset and extent of the transition. Contour plots of the intermittency and momentum thickness Reynolds number are given in Fig. 5.5. An increase in intermittency is evident near 12% chord at the location of the separation-induced transition. The momentum thickness Reynolds number is expected to decrease in high pressure gradient zones. Indeed, the momentum thickness Reynolds number is lower on the upper surface of the airfoil where the pressure gradient is larger. These results follow those of Medida and Baeder [54]. Further validation of the transition model is provided in Chapter 6 for the S809 airfoil.

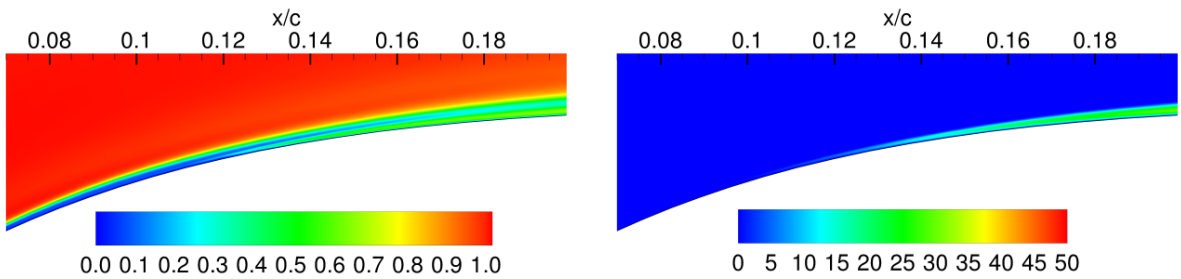

Figure 5.5: Boundary layer transition along upper surface of Aerospatiale-A airfoil showing increase in intermittency and corresponding increase in eddy viscosity. **Left**: Intermittency, γ. **Right**: Non-dimensional eddy viscosity, μ_T/μ_∞.

5.3 Pitching NACA 64A010 Airfoil

Comparison with experiment for a simple oscillating airfoil is used to validate the harmonic balance solver. For this, the experimental data of Davis [21] for a NACA 64a010 airfoil pitching about the quarter chord is used. This case has become a standard test case for frequency domain solver validation [53, 28]. The airfoil is set at a zero mean angle of attack with a pitching amplitude of 1.01 degrees. The Reynolds number is 12.56 million, and the Mach number is 0.796. The airfoil oscillates at a reduced frequency of 0.202. The computational grids for inviscid and turbulent results are shown in Fig. 5.6.

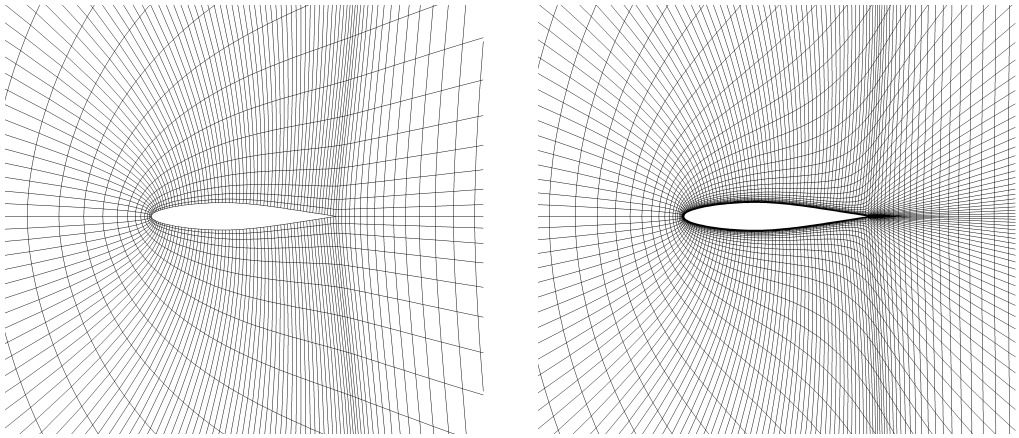

Figure 5.6: NACA 64A010 C-grid. **Left**: 193 x 33 inviscid grid. **Right**: 225 x 65 viscous grid.

Results were obtained using 1 and 3 harmonics for both inviscid and turbulent conditions. In Fig. 5.7, the instantaneous lift and moment coefficients for a complete cycle are shown. The solver is able to predict the lift coefficient fairly well throughout the entire cycle. The moment coefficient is not captured quite as well, but such behavior matches what is observed by McMullen et al. [53] and Gopinath and Jameson [28]. The effect of viscosity is also evident in the results, and the viscous terms here provide better agreement with experimental data.

Mode convergence is achieved in harmonic balance solvers when additional harmonics do not have an effect on the solution. The inviscid and turbulent results both exhibit mode convergence with 1 to 3 harmonics as the lift and moment coefficients for 3 harmonics are very close to their 1 harmonic counterparts. This is not surprising given the linearity of this particular case with such a small oscillation amplitude.

The workload for each sub-time level is approximately equivalent to the workload for a single steady state solution. Thus, the unsteady solution is predicted at a much reduced workload compared to a time accurate unsteady analysis, which requires a converged solution at each physical time step during the cycle. Unsteady solutions

are reconstructed in this case with the computational cost of only about 3 to 7 steady-state solutions.

The convergence histories for the two inviscid and turbulent solutions are shown in Fig. 5.8. The turbulent solutions are slowed due to the extra effort required to resolve the viscous boundary layers. However, the convergence histories for the two inviscid cases and two turbulent cases are very similar, which indicates that while additional harmonics increase the overall computational time, the rate of convergence is unaffected.

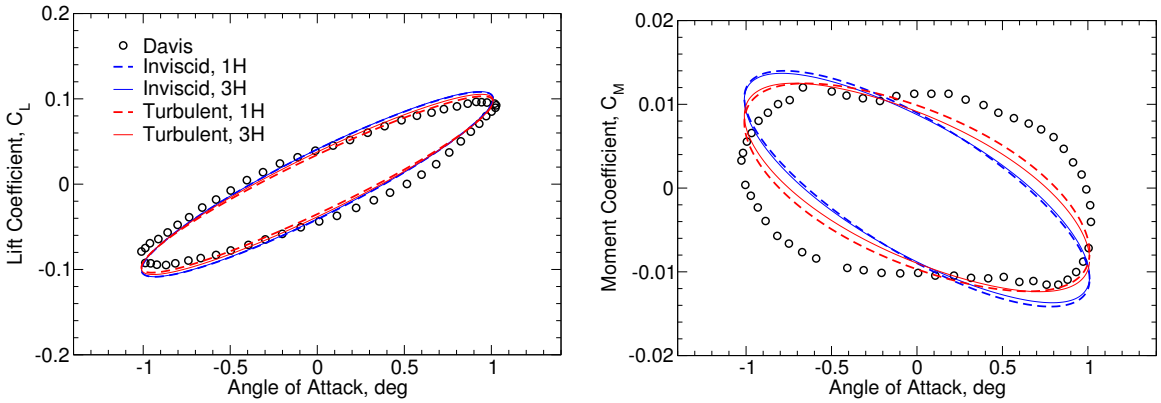

Figure 5.7: Pitching NACA 64A010 airfoil force coefficients. **Left:** Lift coefficient. **Right:** Moment coefficient.

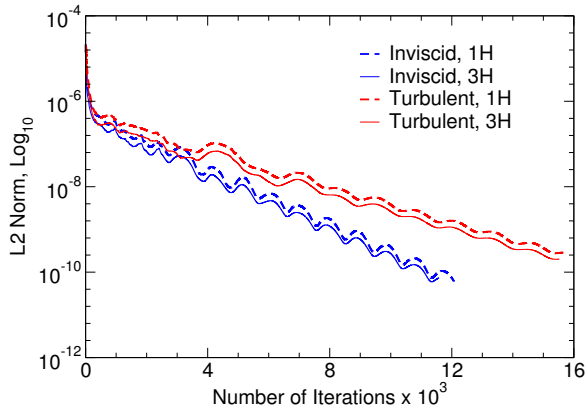

Figure 5.8: Convergence history for pitching NACA 64A010 airfoil.

5.4 Steady ONERA M6 Wing

Transonic flow over the ONERA M6 wing is considered in this section to validate the steady 3D Navier-Stokes solver. Because this case exhibits features such as locally supersonic flow and lambda shock waves [6], it has become a standard CFD case for code validation. The M6 wing is a swept, semi-span wing with no structural twist based on the symmetric ONERA D airfoil section. The experimental data of Schmitt and Charpin [70] and the CFD results from NASA WIND [72] are used for comparison. The particular case under consideration here is for a Mach number of 0.8395, 3.06° angle of attack, and a Reynolds number of 11.72 million based on the mean aerodynamic chord. Inviscid and turbulent results from the current solver are presented. For the inviscid results, the 193 x 33 x 33 C-H grid shown in Fig. 5.9 was used. For the turbulent results, a 257 x 49 x 49 C-H grid was used with a grid spacing near the wall corresponding to $y^+ = 3$.

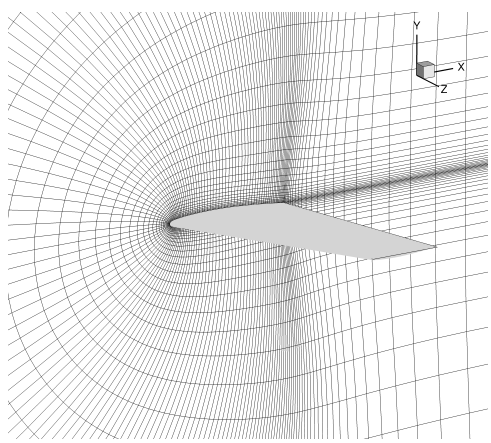

Figure 5.9: Inviscid ONERA M6 wing C-H grid (193 x 33 x 33).

The coefficient of pressure is shown for six spanwise locations along the wing in Fig. 5.10. The overall agreement between the experimental and NASA WIND results with the current inviscid and turbulent results is very good. The only major disagreement is at the double shock at 80% span, and in fact, most CFD solutions found in the literature cannot capture the double shock at this location [24, 85]. Pressure contours on the wing surface and symmetry plane for the current results are

shown in Fig. 5.11. The classically observed lambda-shock formation is evident in both the inviscid and turbulent results.

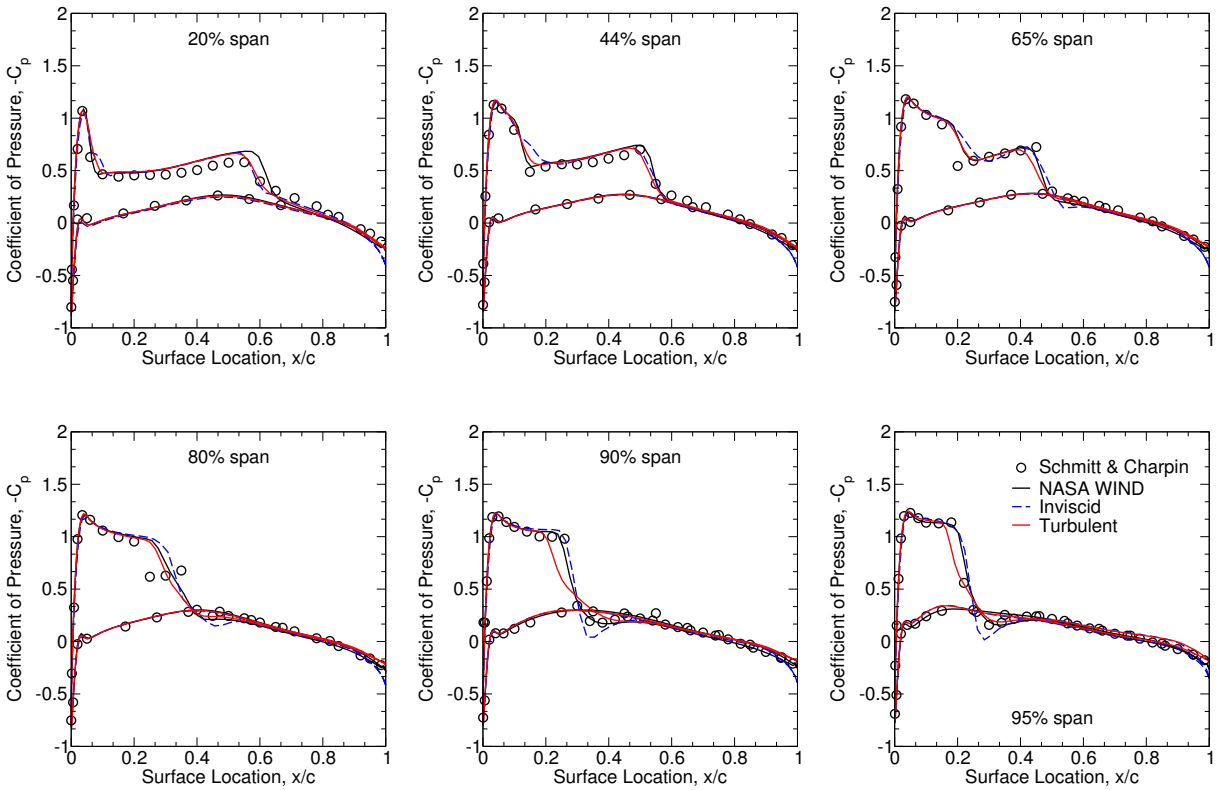

Figure 5.10: Coefficient of pressure distribution for ONERA M6 wing. **Top Left:** 20% span. **Top Middle:** 44% span. **Top Right:** 65% span. **Bottom Left:** 80% span. **Bottom Middle:** 90% span. **Bottom Right:** 95% span.

5.5 Caradonna-Tung Rotor

Flow around a helicopter rotor in hover is considered in this section to validate the relative frame of reference component in the flow solver. Caradonna and Tung [16] conducted a series of experiments for a two-bladed rotor with two untapered rectangular blades for varying collective pitch angles and rotational speeds. The blades have an aspect ratio of 6 and a NACA 0012 airfoil profile. For the cases considered here, the collective pitch angle is $\theta_c = 8.0°$ with tip Mach numbers of

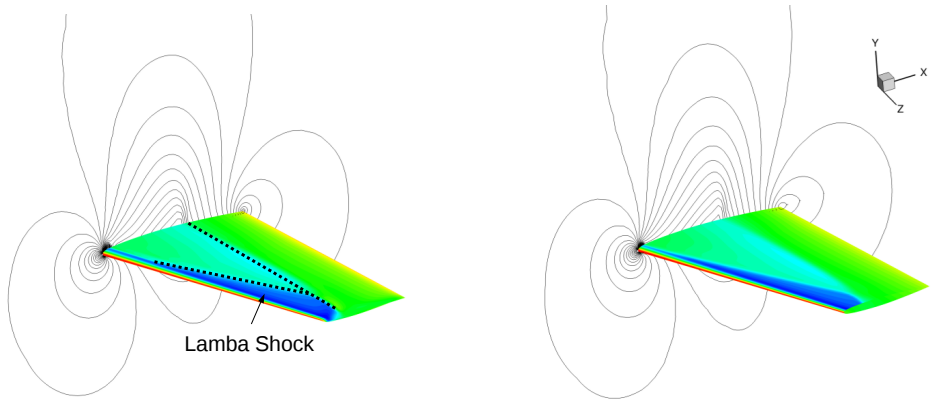

Figure 5.11: Contours of pressure on ONERA M6 wing and symmetry plane. **Left:** Inviscid. **Right:** Turbulent.

0.439 and 0.877. A C-H grid, shown in Fig. 5.12, with a maximum spacing near the wall of $y^+ = 0.4$ was used for the results provided herein. The top, bottom, and outboard boundaries were placed 2 blade spans away from the surface. The grid contained 17 nodes on the blade in the spanwise direction. Using periodic boundary conditions, the grid spanned only a single blade sector.

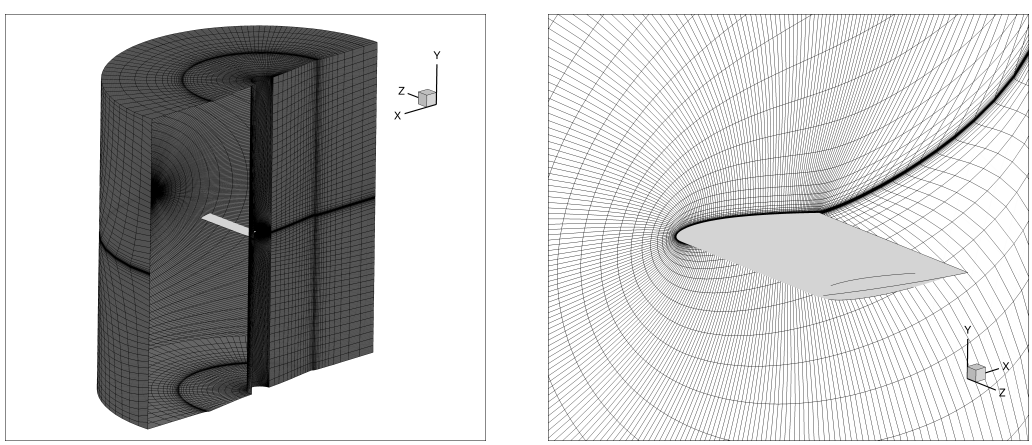

Figure 5.12: Viscous Caradonna-Tung C-H grid (257 x 65 x 33).

To assess the performance of the solver, the surface pressure is compared with experiment at 5 different spanwise locations for a tip Mach number of 0.439. As can be seen in Fig. 5.13, the flow remains subsonic throughout the entire blade span

as expected. The solver matches the experimental data very well, especially at more outboard locations. The surface pressure for Mach 0.877 is shown in Fig. 5.14. Here, it is seen that flow becomes transonic near 80% span. The solver matches experimental data well again with the exception of the vicinity near the shock. Finally, contours of computed static pressure are shown in Fig. 5.15 for Mach 0.877. The formation of the strong shock is clearly evident at the outboard stations.

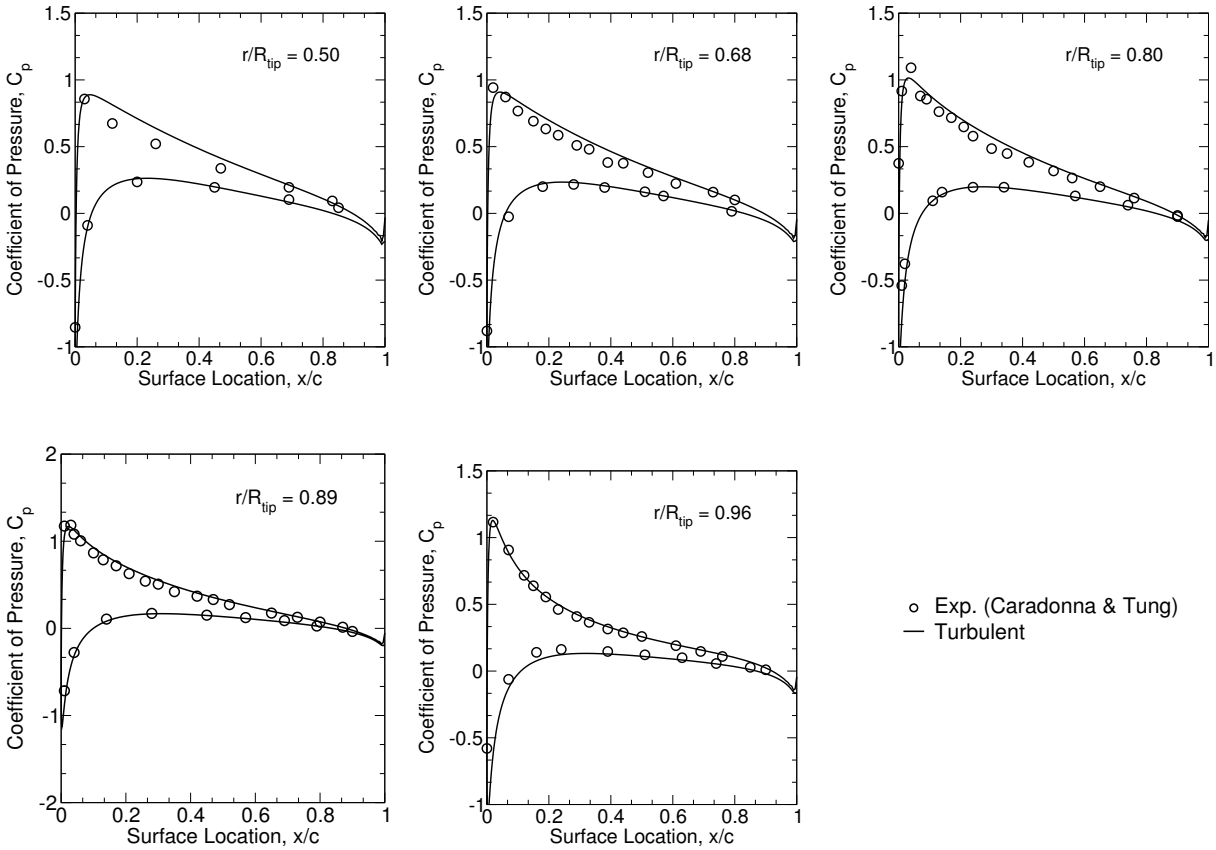

Figure 5.13: Coefficient of pressure distribution for Caradonna-Tung rotor in hover with tip Mach number of 0.439.

5.6 Vortex-Shedding Cylinder in Cross Flow

The harmonic balance implementation of the solver was validated with the classic problem of a cylinder in cross flow. The features of this flow are strongly dictated by

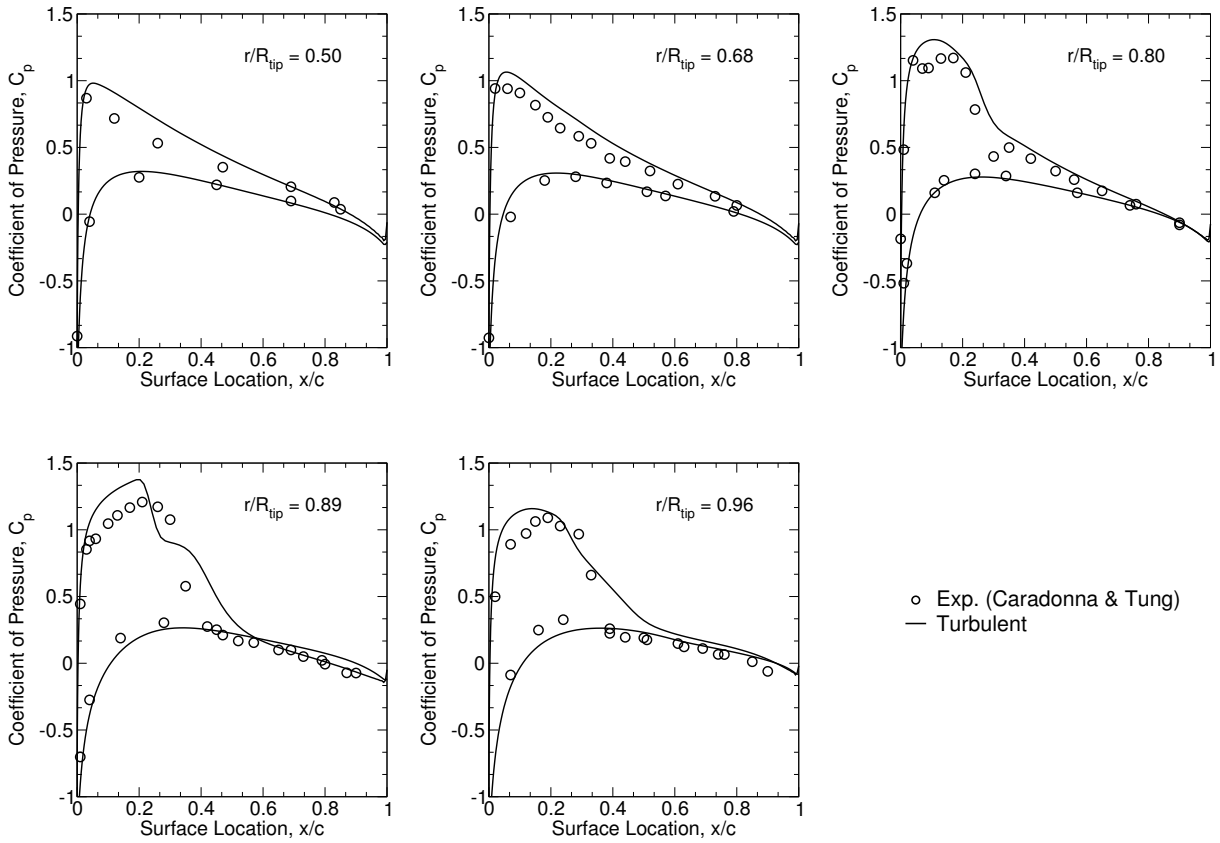

Figure 5.14: Coefficient of pressure distribution for Caradonna-Tung rotor in hover with tip Mach number of 0.877.

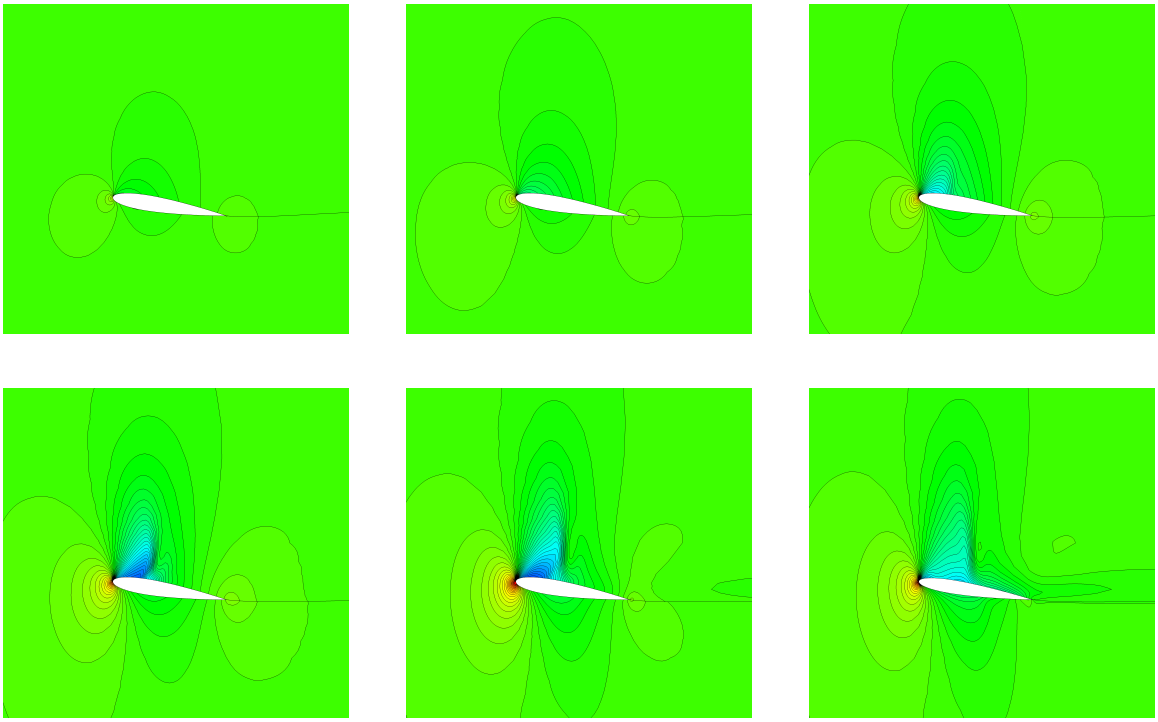

Figure 5.15: Contours of static pressure for Caradonna-Tung rotor in hover with tip Mach number of 0.877. **Top Left:** 50% span. **Top Middle:** 65% span. **Top Right:** 77% span. **Bottom Left:** 87% span. **Bottom Middle:** 97% span. **Bottom Right:** 100% span.

the Reynolds number. For $40 < \mathrm{Re} < 150$, the laminar boundary layer begins to shed from the top and bottom of the cylinder at alternating intervals. This phenomenon is known as the von Kármán vortex street. A Reynolds number of 100 is considered here so that the flow is in the laminar regime.

The unsteady but periodic nature of this flow makes it ideal for harmonic balance modeling. However, the frequency of the vortex shedding must be known *a priori* in order to use the method. This data is readily available over a wide range of Reynolds numbers from experiments, but a better approach is to use a frequency search procedure[53, 23]. An O-grid, shown in Fig. 5.16, with 257 nodes in the wrap around direction and 129 nodes in the wall normal direction was used. The solver was specially modified to accommodate an O-grid in this case since a highly quality grid in the boundary layer near the coordinate cut of a cylinder is nearly impossible with a C-grid. Symmetry boundary conditions were used at both edges of the domain to simulate an infinite span cylinder.

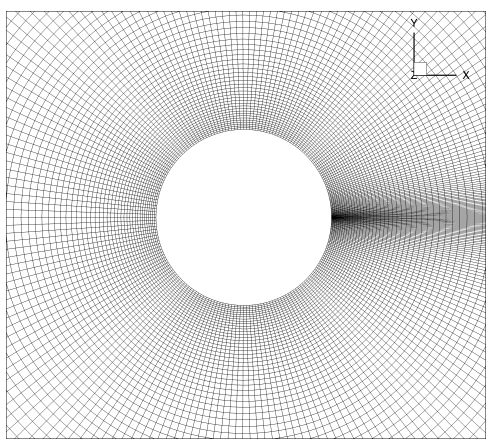

Figure 5.16: Infinite span cylinder O-grid (257 x 129).

The Strouhal number is used to characterize the vortex shedding frequency. Many experiments appear in the literature documenting the relationship between the Strouhal and Reynolds numbers. For example, Williamson measured Strouhal number for Reynolds numbers ranging from 40 to 200 [101]. For a Reynolds number of 100, the Strouhal number is experimentally determined to be approximately 0.16, which

was successfully predicted by the frequency finding procedure. The unsteady lift coefficient (Fig. 5.17) can also be used to determine the Strouhal number. Applying a fast Fourier transform (FFT) to the unsteady lift data, the Strouhal number is given by the peak in the frequency data (see Fig. 5.17).

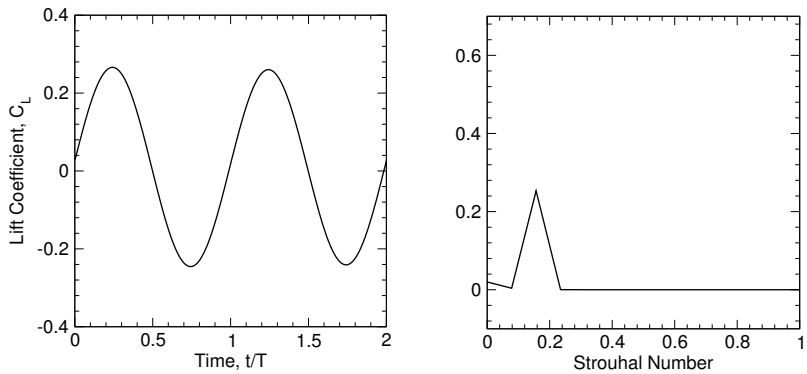

Figure 5.17: Lift coefficient for Re = 100. **Left:** Temporal lift coefficient. **Right:** FFT of temporal lift coefficient.

Vorticity contours capture the vortex street effect as shown at 6 different snapshots throughout one shedding cycle in Fig. 5.18. The vorticity shedding is evident from the contour plots where shed vortices are shown alternating from the top and bottom of the cylinder.

5.7 AGARD 445.6 Wing

In this section, flutter of the AGARD 445.6 wing [103, 102] is examined. This is a standard aeroelastic benchmark coming from a series of flutter tests carried out at NASA Langley's transonic wind tunnel. The name for this set of cases, 445.6, describes the geometry of the problem. The first 4 indicates the airfoil profile, which is the NACA 65A004. This is a very thin profile having a nose radius of 0.1% chord. The 45 points to the sweep angle along the quarter chord line of 45°. The remaining .6 indicates a taper ratio of 0.66. The configuration considered in this paper is referred to as the Weakened 3 model. This model has a semi-span of 0.762 m, root chord of

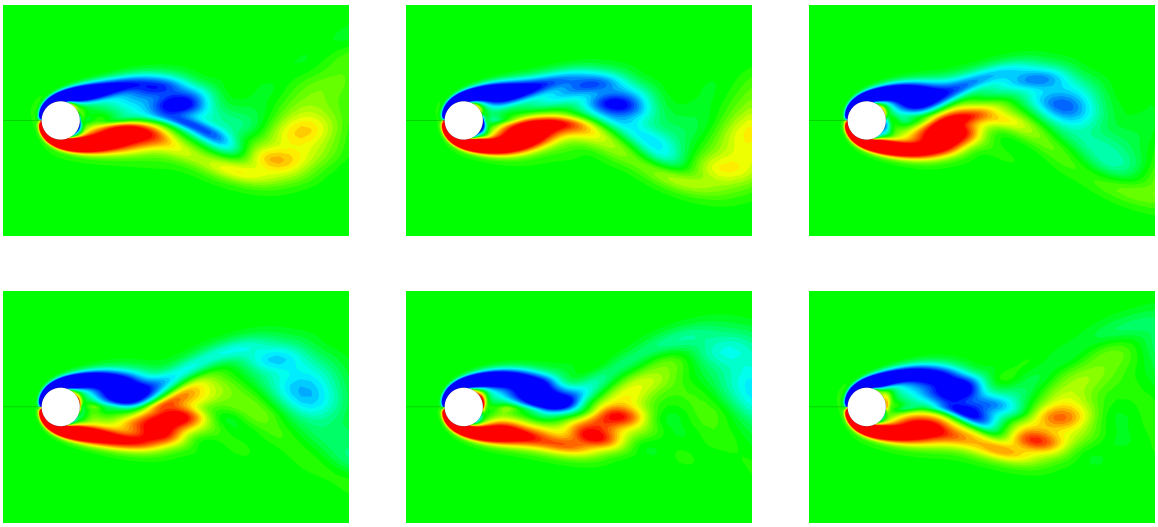

Figure 5.18: Contours of vorticity through one cycle of vortex shedding with Re = 100.

0.559 m, and an aspect ratio of 1.65. Structural properties and modal data are also given in the referenced reports.

For the Weakened 3 model, Yates [102] provides experimentally determined mode shapes for the first six modes. The first two bending and torsional modes are shown mapped onto a computational grid in Fig. 5.19. The experimental modes are mapped to the CFD grid using a polynomial fit of the displacements as a function of node location. Lee-Rausch and Batina [45] showed flutter in this case is almost entirely dependent upon the interactions of the first bending and first torsional mode shapes alone. Many others have also demonstrated accurate flutter predictions with these modes alone. Thus, only these two mode shapes are considered in the following analysis.

Generalized aerodynamic forces for small amplitude motions (1.0×10^{-4}) of the first two modes are computed on an inviscid and viscous grid to carry out flutter analyses in both inviscid and turbulent flow fields. The inviscid grid consists of 193 nodes in the wrap-around direction and 33 nodes in the wall normal direction. In the spanwise direction, the grid contains 17 nodes on the wing and 17 nodes extending to

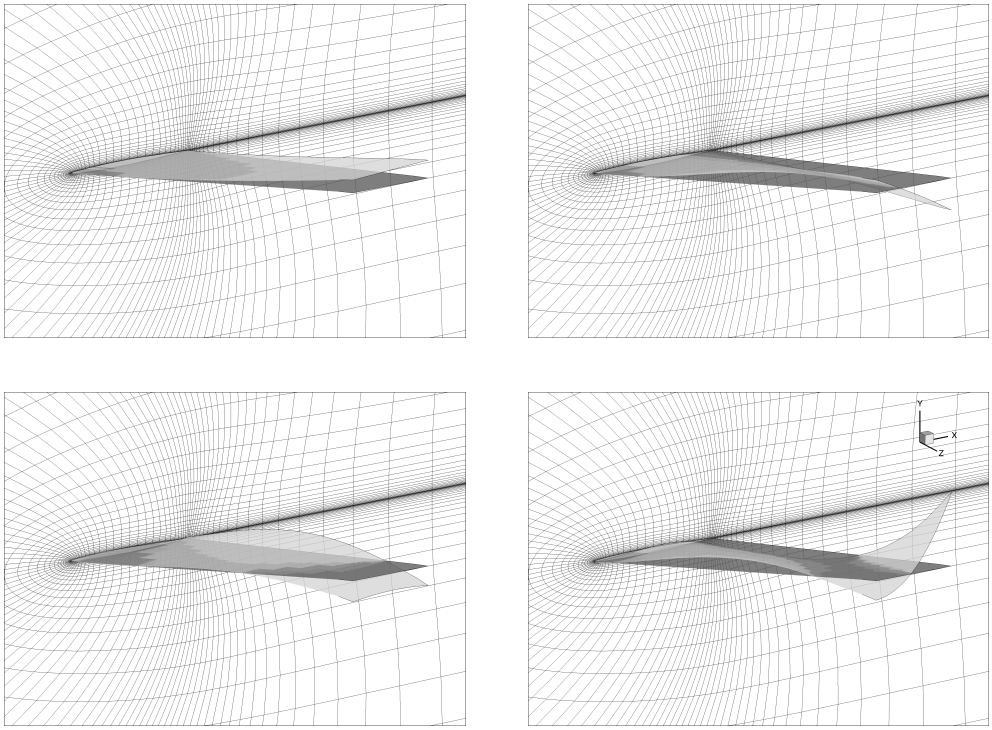

Figure 5.19: Measured mode shapes for AGARD 445.6 Weakened configuration. **Top Left:** Mode one (first bending) 9.6 Hz. **Top Right:** Second Mode (first twisting) 38.2 Hz. **Bottom Left:** Third mode (second bending) 48.4 Hz. **Bottom Right:** Fourth mode (second twisting) 91.5 Hz.

Table 5.1: Sample AGARD 445.6 Turbulent Flutter Calculation, $M_\infty = 0.960$

$\bar{\omega}$	V_f	Determinant
0.08250	$0.3055 + 5.022\times10^{-4}\ i$	$-1.324\times10^{-2} + 4.303\times10^{-3}\ i$
0.08247	$0.3058 - 7.744\times10^{-6}\ i$	$2.045\times10^{-4} - 7.154\times10^{-5}\ i$
0.08240	$0.3065 - 1.281\times10^{-3}\ i$	$3.532\times10^{-2} - 9.618\times10^{-3}\ i$

the far field. The viscous grid contains 257 x 97 nodes in the wrap-around and wall normal directions with the same distribution in the spanwise direction as the inviscid grid. The approximate grid spacing at the solid wall is $y^+ = 0.2$.

Flutter is predicted by substituting the generalized aerodynamic forces into Eq. 4.12. These forces are determined by using an excitation of one mode and computing the associated generalized forces for all modes individually due to this excitation. The constant k_w is set to 1.596 to match the model properties, and m_j is set to unity due to the use of mass normalized mode shapes. For $M_\infty = 0.960$, a sample calculation is provided in Table 5.1. The reduced frequency, $\bar{\omega}$, is varied until the reduced velocity, V_f, becomes purely real. In practice, the reduced frequency is determined when the imaginary part of V_f changes sign. Notice the imaginary part of V_f changes sign between $\bar{\omega} = 0.08250$ and $\bar{\omega} = 0.08247$. The sign change indicates V_f has a purely real value between these two frequencies, and the magnitudes of the respective imaginary parts (5.022×10^{-4} and 7.744×10^{-6}) indicate that the flutter frequency is very close to $\bar{\omega} = 0.08247$.

With this approach, the predicted flutter velocity and frequency ratio using inviscid and turbulent aerodynamic data are plotted in Fig. 5.20. The experimental results of Yates [103] and the inviscid predictions of Lee-Rausch and Batina [44] are also included. Only the subsonic cases are considered in the present effort. The experimental data, predictions of Lee-Rausch and Batina, and the current predictions are all fairly close near the upper subsonic limit. The three sets of data begin to diverge as the Mach number decreases. This is a common trend from other published AGARD 445.6 predictions. There is almost no difference between the current inviscid

and turbulent predictions as far as frequency ratio, but the turbulent predictions are much closer to the experimental data at higher Mach numbers. For example, at Mach 0.960, the turbulent flutter velocity is within 1% of the experimental data while the inviscid flutter velocity is only within 10%. While it might be possible to improve the current predictions by generating mode shapes from a custom structural model, the results shown here are sufficient in validating the aeroelastic model.

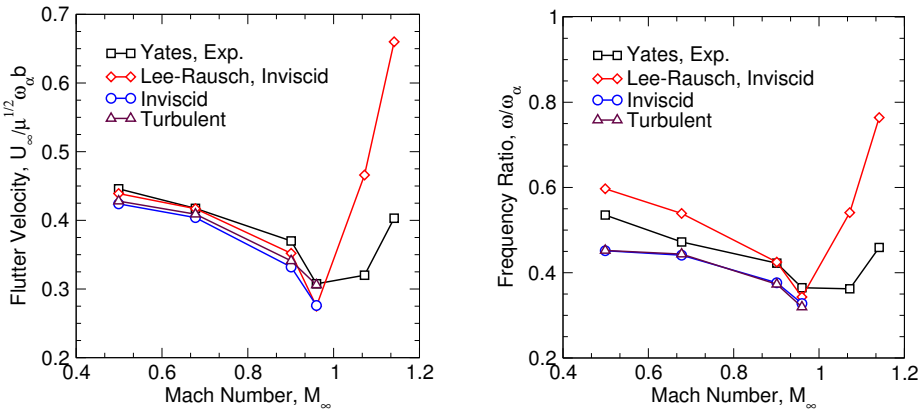

Figure 5.20: Inviscid and viscous predictions for AGARD 445.6 wing. **Left:** Flutter velocity. **Right:** Frequency ratio.

Chapter 6

Pitching S809 Airfoil

This chapter investigates the impact of transition modeling on static and dynamic stall predictions of the S809 airfoil. The first part of the chapter examines steady flow about an S809 airfoil to both validate the transition model and demonstrate the need for transition modeling in wind turbine flows. The second part of the chapter gives a comparison between fully turbulent and transition solutions for a pitching S809 airfoil.

6.1 Steady Results

To validate the transition model and assess its ability, a series of steady S809 airfoil simulations are performed. For these simulations, the Reynolds number is 1 million and the free stream turbulence intensity is set to 0.05%. The angle of attack is varied between -12 and 30 degrees. Two experimental data sets are used for comparison. The first set of data are from wind tunnel tests at the Delft University of Technology and are reported in Somers [74]. The second set of data are from wind tunnel tests at the Ohio State University [66]. The C-grid shown in Fig. 6.1 was used for all steady and unsteady simulations. This grid contains 449 x 129 nodes in the wrap around and normal directions with a near wall spacing of $y^+ = 0.1$. The grid extends approximately 50 chord lengths in all directions. To check grid independence, the grid

resolution was doubled for steady runs at 3, 9, and 18 degrees angle of attack both with and without transition modeling. The maximum observed variation in the lift coefficient was 2%, and the maximum observed variation in the moment coefficient was 3%.

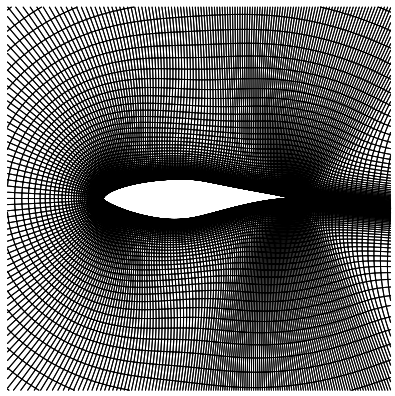

Figure 6.1: S809 C-grid, 449 x 129 nodes.

It is difficult to predict stall and post stall behavior of the S809 airfoil using a RANS-based solver. The static force coefficients in Fig. 6.2 emphasize the necessity of a transition model to modify the boundary layer turbulence in order to accurately model the S809 airfoil when the flow is separated. Only pressure contributions for drag are reported in the experiment. For consistency, only pressure contributions are used in the CFD results for drag. In the post stall region, the lift is largely over-predicted without the transition model, but reasonable agreement is found with the aid of the transition model. The success of the transition model in this region is due to an increase in eddy viscosity in the separation zone compared to the fully turbulent model. The second lift curve beginning around 20° degrees is predicted prematurely by the transition model and late by the fully turbulent model. The delayed separation in the fully turbulent case and the premature second lift increase with the transition model will have a noticeable effect in the dynamic stall cases in the proceeding section. Returning to Fig. 6.2, the drag is increased when compared to the fully turbulent simulation in the post stall region owing to the earlier onset of separation with the transition model. For attached flows, it appears that transition

modeling is not necessary in terms of force coefficient accuracy, but as will be seen momentarily, the solutions are still very different due to the boundary layer not being assumed fully turbulent.

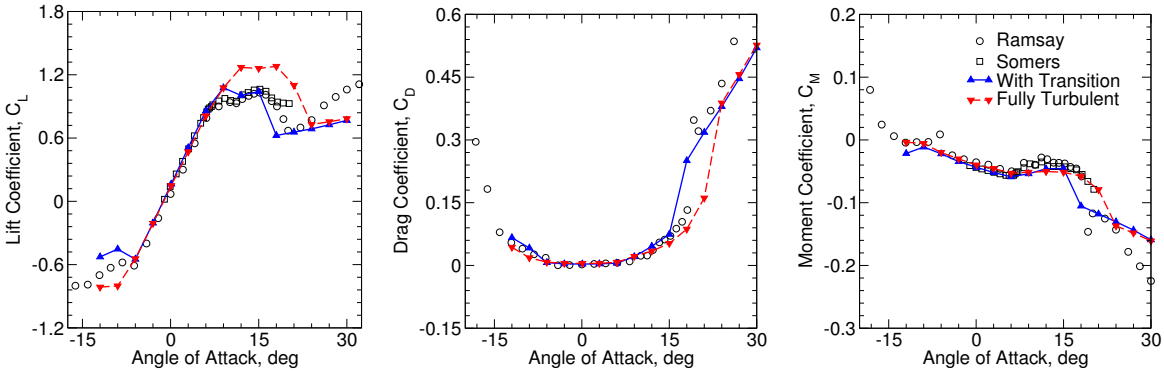

Figure 6.2: Steady force coefficients. **Left:** Lift. **Middle:** Drag. **Right:** Moment.

To examine the effect of the transition model more closely, the pressure coefficients at 4.1° and 12.2° are given in Fig. 6.3 with and without transition. When the flow is attached, the disagreement between the two predictions is small, but a critical flow feature is only captured with the transition model. Near the mid-chord on the upper and lower surfaces, the fully turbulent boundary layer remains attached, and the transition model predicts the laminar separation bubble and turbulent reattachment. This bump in the pressure distribution indicated on the lower surface in Fig. 6.3 is indicative of such behavior [40]. When the flow is separated, the power of the transition model is easier to see. The pressure coefficient closely matches experimental data with the transition model on the suction surface while the fully turbulent simulation does not.

The turbulent eddy viscosity and intermittency for these two cases provide further insight. Referring to Fig. 6.4, the turbulent eddy viscosity is reduced with the transition model when compared to the fully turbulent simulation at 4.1°. Such a reduction in eddy viscosity reflects the mostly laminar behavior of the actual flow for this case. When the angle of attack is increased to 12.2°, the transition model serves to increase the turbulent eddy viscosity as shown in Fig. 6.5. The fully

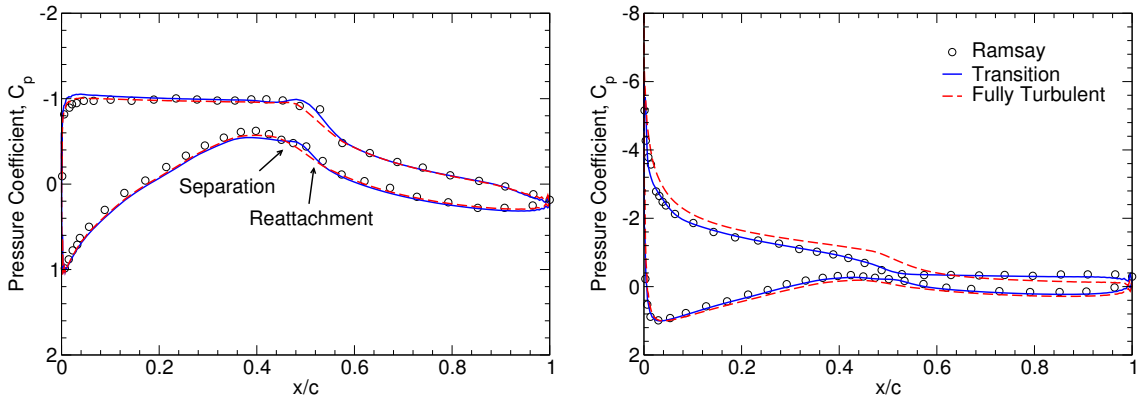

Figure 6.3: Coefficients of pressure. **Left:** 4.1°. **Right:** 12.2°.

turbulent simulation under-predicts the separation for this case, which is reflected by the insufficient eddy viscosity in the separation zone.

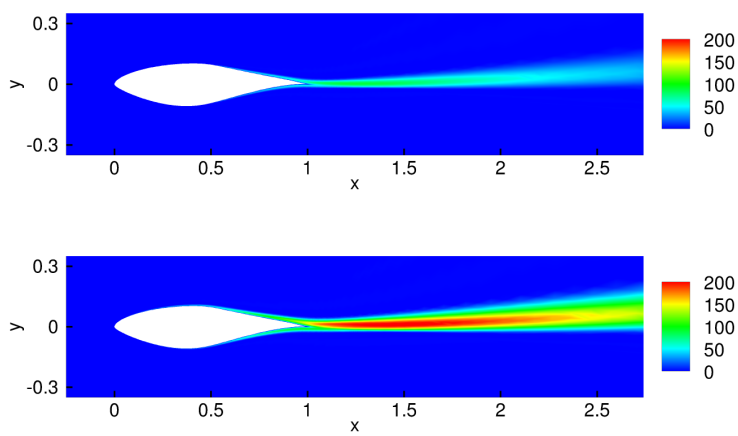

Figure 6.4: Non-dimensional eddy viscosity contours at 4.1°. **Top:** With transition model. **Bottom:** Fully turbulent.

The intermittency adjusts the eddy viscosity predicted by the fully turbulent Spalart-Allmaras model. When the value is one, the eddy viscosity is unaltered. As the intermittency goes to zero, the eddy viscosity production is decreased to reflect the laminar nature of the flow in that region. For attached flow, Fig. 6.6 shows that the intermittency slowly increases from 0 near the airfoil surface to 1 near the edge of the boundary layer. The boundary layer steadily grows moving downstream from the leading edge of the airfoil. When the flow is separated, the intermittency grows

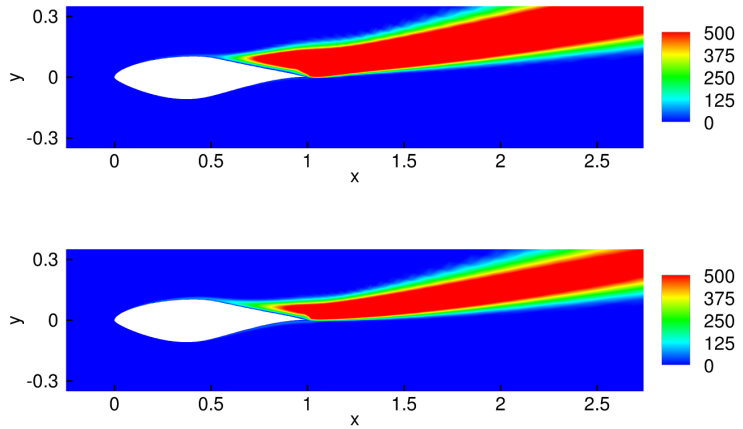

Figure 6.5: Non-dimensional eddy viscosity contours at 12.2°. **Top:** With transition model. **Bottom:** Fully turbulent.

more rapidly before the flow detaches. In the separation wake, the eddy viscosity is kept near fully turbulent levels.

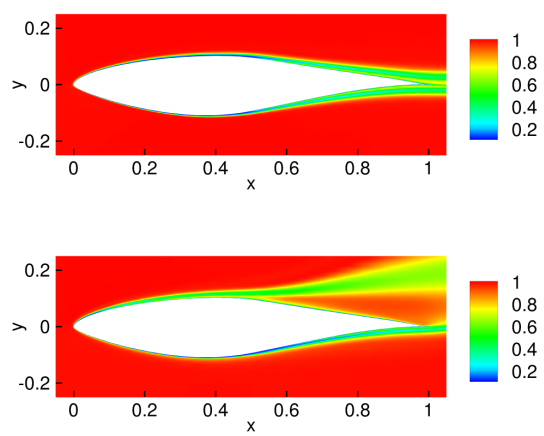

Figure 6.6: Transition model intermittency contours. **Top:** 4.1°. **Bottom:** 12.2°.

The convergence rates for these two cases are shown in Fig. 6.7. The convergence rates with and without the transition model follow the same basic shape, indicating that the inclusion of the transition model has little effect on the global convergence properties of the solution.

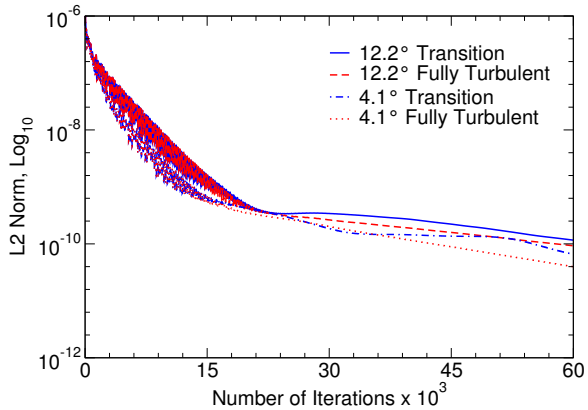

Figure 6.7: Steady convergence rates. L2 norm computed from residuals from Navier-Stokes and Spalart-Allmaras equations.

6.2 Unsteady Results

Given the necessity of the transition model to predict static stall, we now focus on dynamic stall predictions with and without the transition model. Dynamic stall is characterized by vortex shedding near the leading edge of the airfoil that produces a pressure wave along the surface of the airfoil as the disturbance travels downstream [46]. Compared to the static stall case, when the airfoil is pitching up, stall is delayed to higher angles of attack whereas when the airfoil is pitching down, stall is delayed to lower angles of attack. Such behavior gives rise to hysteresis in the force coefficient plots over an oscillation cycle.

In addition to the steady data presented earlier, Ramsay [66] also conducted a series of oscillating S809 airfoil tests where mean angle of attack, oscillation amplitude, reduced frequency, and Reynolds number were varied. Predictions for some of these cases are presented in this section with and without the transition model using the harmonic balance solver. The cases are summarized in Table 1. For clarity, only the average values from three pitching cycles are presented from the experimental data. Since the reported experimental data is given at different angles of attack during each cycle, the angles of attack from the first cycle are kept, and data is interpolated to

Table 6.1: Unsteady S809 Airfoil Simulation Matrix

Case Number	Mean Angle of Attack, α	Oscillation Amplitude	Reduced Frequency, κ	Reynolds Number
1	8.0^o	5.5^o	0.026	1.01 million
2	8.0^o	5.5^o	0.077	1.00 million
3	20.0^o	5.5^o	0.025	1.00 million
4	8.0^o	10.0^o	0.077	0.98 million

these angles in the remaining two cycles. Error bars corresponding to the maximum and minimum values at each angle over the three cycles are included.

In harmonic balance solvers, mode convergence is achieved when the solution does not change with the addition of more harmonics in the solution. The lift coefficient plots for Case 1 shown in Fig. 6.8 reveal that more harmonics are necessary for mode convergence when the transition model is used. This is not surprising given the added complexity of the solution when dynamic stall occurs, and only the transition model predicts close to an appropriate level of stall. Mode convergence occurs with three to five harmonics without transition and seven to nine harmonics with transition. Since each additional harmonic means solving for two more sub-time levels, the transition model adds approximately the cost of four steady-state solutions compared to the fully turbulent solution. It was found that 7 harmonics with the transition model and 5 harmonics for fully turbulent solutions were sufficient for the other three cases considered in this dissertation.

For the first case, the necessity of the transition model is evident from the lift coefficient plots in Fig. 6.8. Without the transition model, dynamic stall only very weakly occurs. The transition model offers an accurate prediction of the lift throughout the entire cycle. The drag coefficients are shown in Fig. 6.9 for the fully turbulent and transition models. Despite the large under-prediction in lift, the fully turbulent model offers a reasonable prediction in drag. The transition model appears to capture the behavior of the experimental data, but it does overshoot the experimental values at higher angles of attack. The transition model again shows

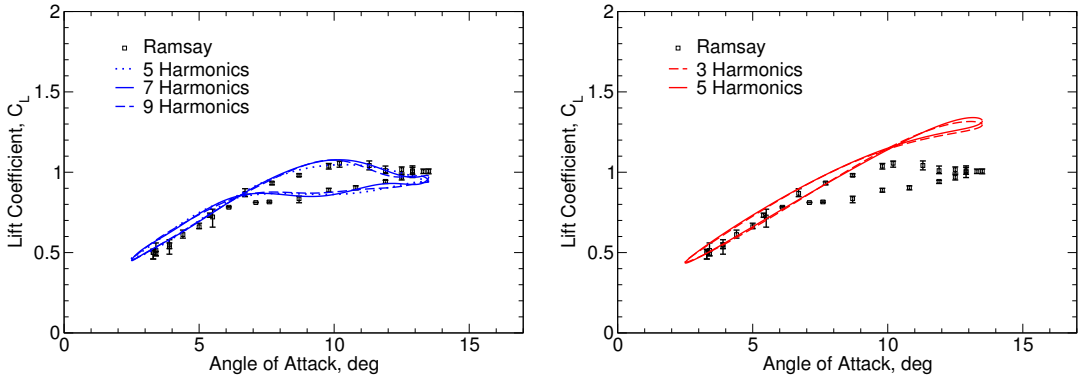

Figure 6.8: Case 1 lift coefficients. Mean angle of attack is 8.0°, oscillation amplitude is 5.5°, reduced frequency is 0.026, and Reynolds number is 1.01 million. **Left:** With transition model. **Right:** Fully turbulent.

improvement in moment coefficient (Fig. 6.10) predictions in the dynamically stalled portion of the cycle. While the solution does not quite match the experimental values, the features in the experimental data are reproduced well with the transition model. The fully turbulent solution does not capture such behavior.

Contours of velocity magnitude with and without transition are shown in Figs. 6.11 and 6.12 at 10° during the upstroke and downstoke. The wake is much larger with the transition model in both the upstroke and downstroke, which reflects the deeper stall of the airfoil. The fully turbulent model is only approaching the onset of dynamic stall at this angle of attack. The contours of vorticity and streamlines in Figs. 6.13 and 6.14 at angles of attack throughout the cycle provide greater insight. During the upstroke, the experimental data indicates that dynamic stall has occurred at 10° angle of attack as does the transition model. Only the streamlines from the transition model exhibit a recirculation zone indicative of separated flow. The fully turbulent solution does not predict dynamic stall until a higher angle of attack. Both solutions exhibit recirculation at the maximum angle of attack, but only the transition model predicts a sufficiently large recirculation zone. During the downstroke, only the transition model shows any appreciable recirculation. Again, the transition model is necessary to provide sufficient flow separation to match the experimentally observed dynamic

stall. The increased vorticity at higher angles of attack for the transition model is also apparent in Figs. 6.13 and 6.14.

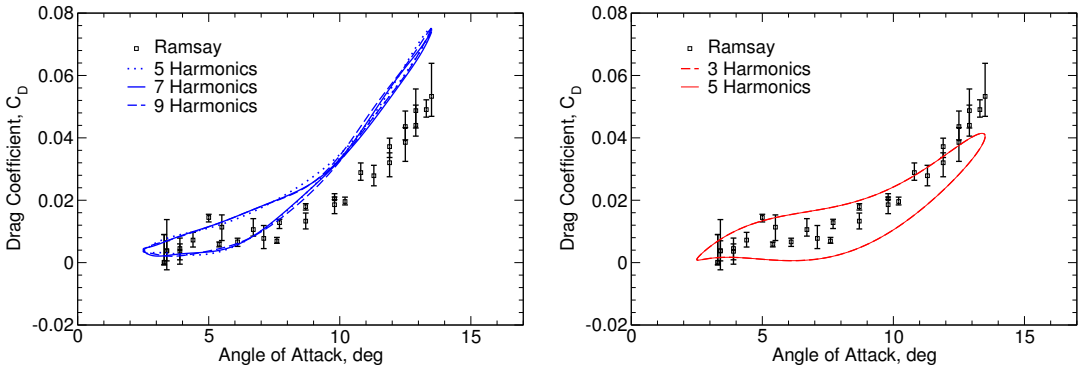

Figure 6.9: Case 1 drag coefficients. Mean angle of attack is 8.0°, oscillation amplitude is 5.5°, reduced frequency is 0.026, and Reynolds number is 1.01 million. **Left:** With transition model. **Right:** Fully turbulent.

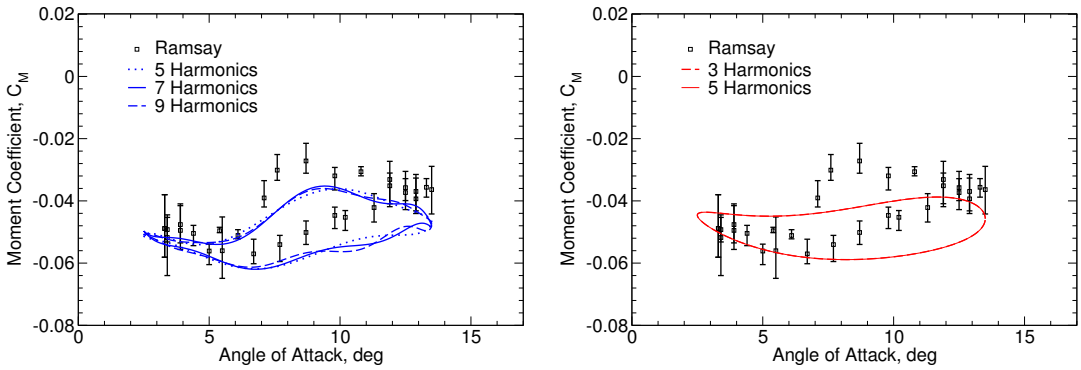

Figure 6.10: Case 1 moment coefficients. Mean angle of attack is 8.0°, oscillation amplitude is 5.5°, reduced frequency is 0.026, and Reynolds number is 1.01 million. **Left:** With transition model. **Right:** Fully turbulent.

Case 2 is the same as Case 1 except that the reduced frequency is increased approximately threefold. The faster pitching delays dynamic stall to higher angles of attack in the upstroke and increases it to lower angles during the downstroke. This provides for a more dramatic hysteresis effect in the force data. The force coefficients in Fig. 6.15 show a similar performance to Case 1. The fully turbulent model is still inadequate in terms of predicting dynamic stall. The transition model enjoys the same success as before and nicely captures the increased hysteresis effect. The drag

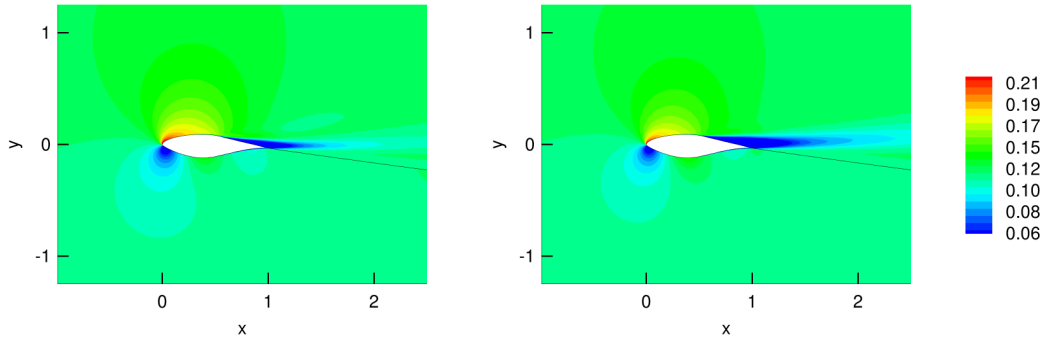

Figure 6.11: Case 1 contours of velocity magnitude at 10° angle of attack with transition. **Left:** Upstroke. **Right:** Downstroke.

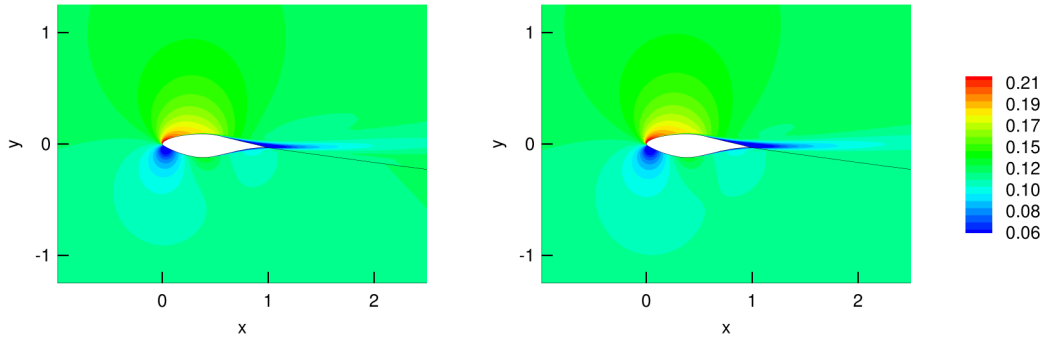

Figure 6.12: Case 1 fully turbulent contours of velocity magnitude at 10° angle of attack. **Left:** Upstroke. **Right:** Downstroke.

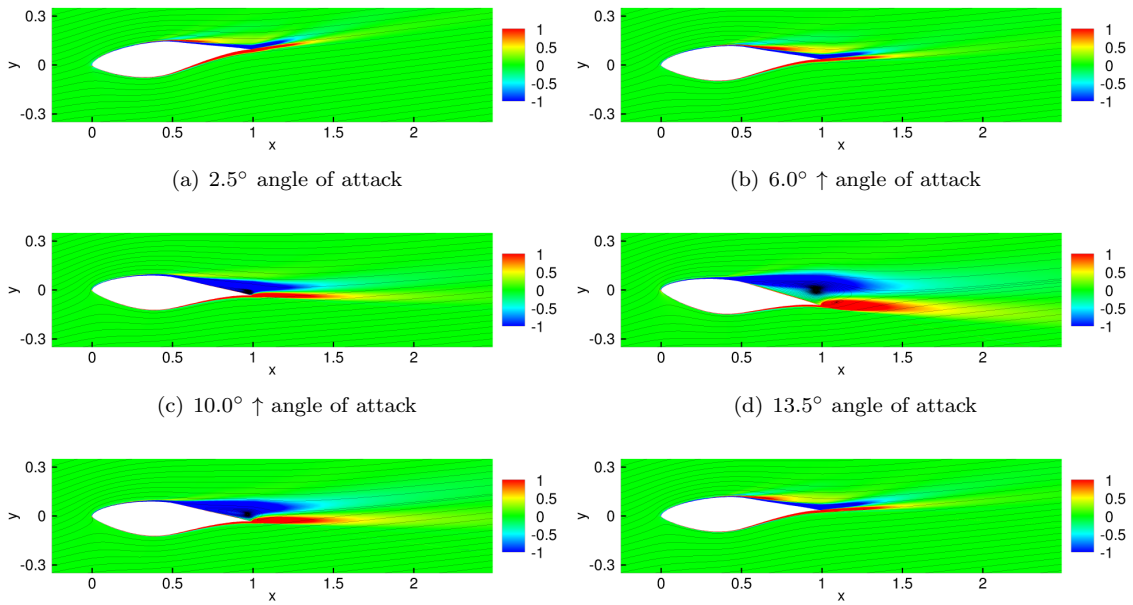

(a) 2.5° angle of attack

(b) 6.0° ↑ angle of attack

(c) 10.0° ↑ angle of attack

(d) 13.5° angle of attack

(e) 10.0° ↓ angle of attack

(f) 6.0° ↓ angle of attack

Figure 6.13: Case 1 contours of vorticity and streamlines throughout a complete cycle with transition. Arrows indicate either upstroke or downstroke portion of the cycle.

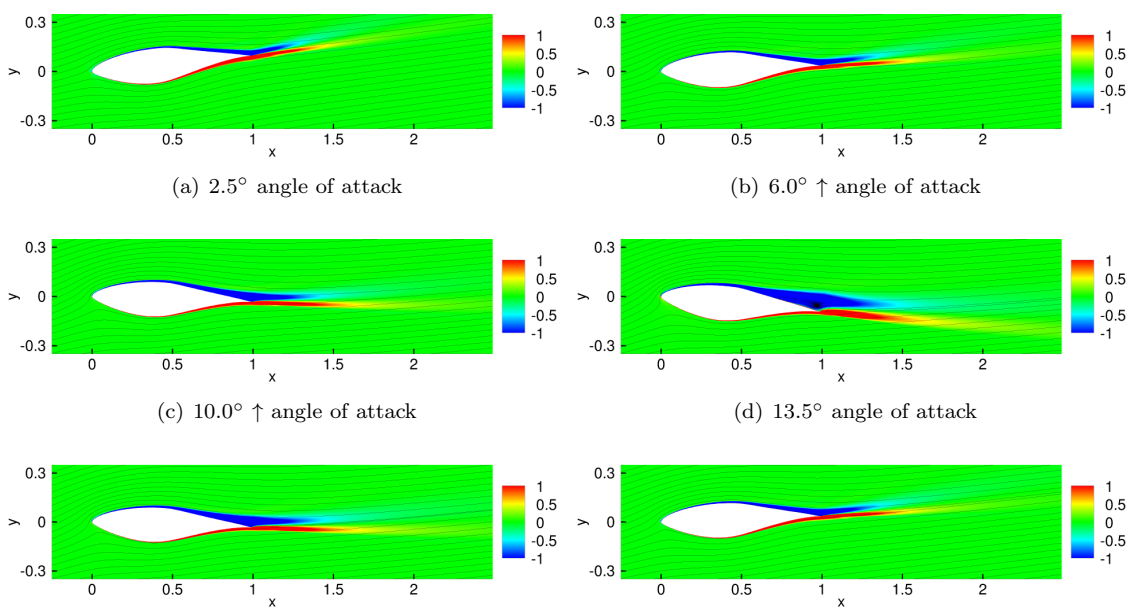

(a) 2.5° angle of attack

(b) 6.0° ↑ angle of attack

(c) 10.0° ↑ angle of attack

(d) 13.5° angle of attack

(e) 10.0° ↓ angle of attack

(f) 6.0° ↓ angle of attack

Figure 6.14: Case 1 fully turbulent contours of vorticity and streamlines throughout a complete cycle. Arrows indicate either upstroke or downstroke portion of the cycle.

and moment coefficients are also similar to Case 1. Neither model matches the drag well throughout the entire cycle. With the moment coefficient, the transition model again captures the behavior in the experimental data albeit with a small offset.

In comparison to Case 1, the vorticity contour and streamline plots with transition in Fig. 6.16 highlight the delay in onset of dynamic stall. The vorticity is reduced and the recirculation zone is no longer present at 10° during the upstroke. During the downstroke at 10°, the vorticity and recirculation is similar to Case 1, but the leading edge vorticity now has more separation along the latter portion of the airfoil.

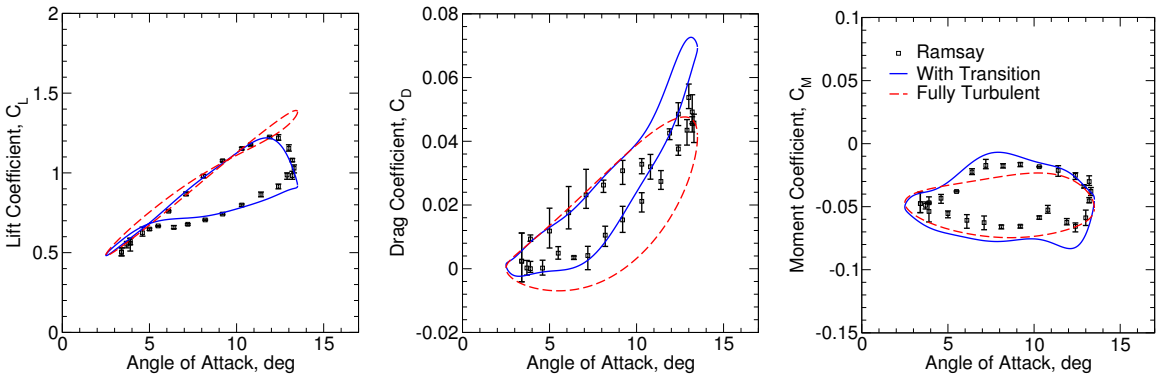

Figure 6.15: Case 2 force coefficients. The transition model solution contains 7 harmonics, and the fully turbulent solution contains 5 harmonics. Mean angle of attack is 8.0°, oscillation amplitude is 5.5°, reduced frequency is 0.077, and Reynolds number is 1.00 million. **Left:** Lift. **Middle:** Drag. **Right:** Moment.

Case 3 is well into the massively separated regime centered at 20° angle of attack. At large angles of attack, the steady solutions with and without transition start to merge. Referring back to Fig. 6.2, the lift, drag, and moment coefficients predicted by the transition and fully turbulent models begin to agree at the highest angles of attack considered. The same is true for the unsteady solutions. The force coefficients in Fig. 6.17 begin to match at the higher angles of attack in the cycle. Neither model is capable of predicting the behavior exhibited by the experimental data around 23°. The fully turbulent solution matches experimental data better than the transition model solution at the lower angles of attack.

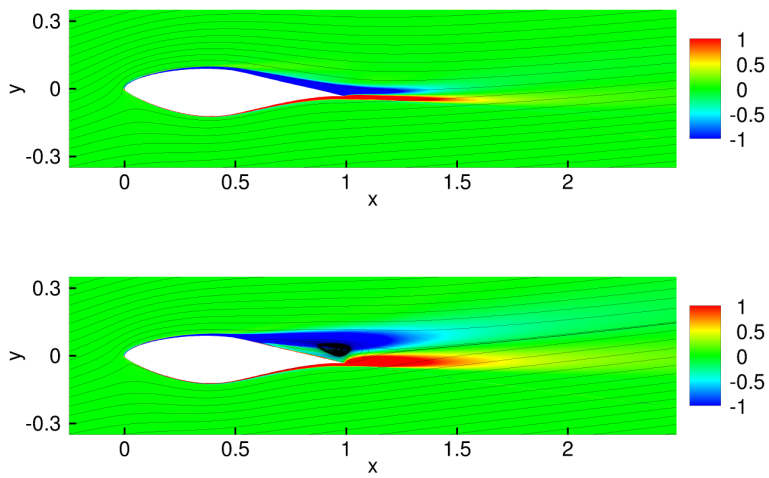

Figure 6.16: Case 2 contours of vorticity and streamlines at 10° angle of attack with transition. **Top:** Upstroke. **Bottom:** Downstroke.

The nature of dynamic stall is easiest to observe in Case 3. Vorticity contours at the lowest angle of attack in Fig. 6.18 show the leading edge vortex moving aft along the airfoil and interacting with the trailing edge vortex. A new vortex is being generated at the leading edge of the airfoil as the previous vortex moves downstream.

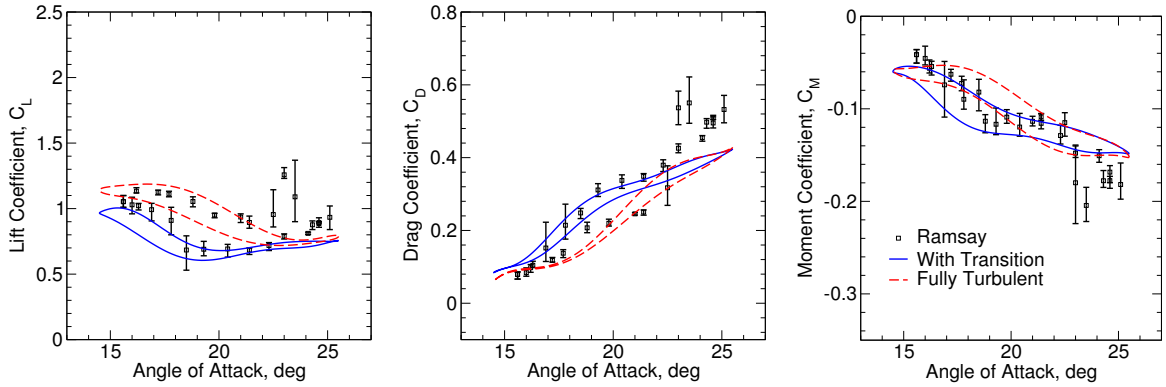

Figure 6.17: Case 3 force coefficients. The transition model solution contains 7 harmonics, and the fully turbulent solution contains 5 harmonics. Mean angle of attack is 20.0°, oscillation amplitude is 5.5°, reduced frequency is 0.025, and Reynolds number is 1.00 million. **Left:** Lift. **Middle:** Drag. **Right:** Moment.

The mean angle of attack is changed back to 8° in Case 4, and the oscillation amplitude is increased from 5.5° to 10°. In the steady force data, a sharp change

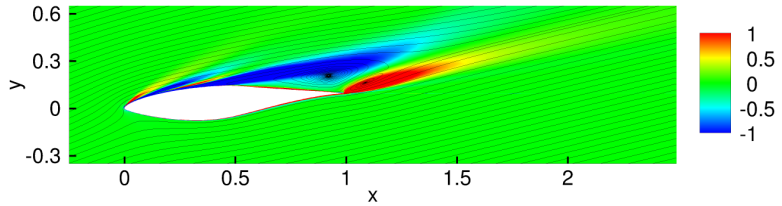

Figure 6.18: Case 3 contours of vorticity and streamlines at 14.5° angle of attack.

in slope occurs right near the maximum angle of attack reached in this case, which makes it especially difficult to model. The lift curves in Fig. 6.19 show that both models predict dynamic stall in this case. The transition model, however, is adversely affected by a poor solution in one sub-time level near the maximum angle of attack. Looking back at the steady force prediction, the largest disagreement between the experimental data and the transition model is at 18°. This is where the transition model prematurely predicts the onset of the slope change. The failure of the transition model in this one location has a strong negative impact on the unsteady solution reconstruction. To minimize the impact of a poor solution at one sub-time level, the number of harmonics could be increased, but such a study is not included here. The fully turbulent model in this case performs better than the related Cases 1 and 2, but dynamic stall is still largely under-predicted.

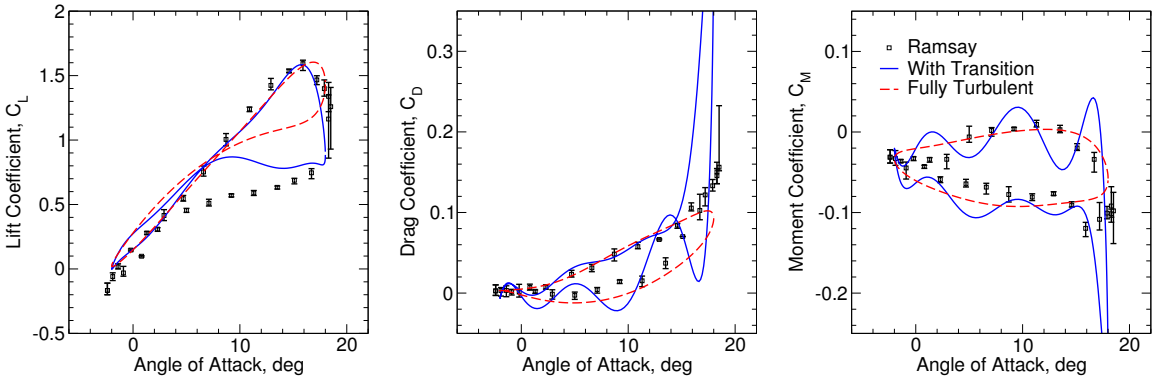

Figure 6.19: Case 4 force coefficients. The transition model solution contains 7 harmonics, and the fully turbulent solution contains 5 harmonics. Mean angle of attack is 8.0°, oscillation amplitude is 10.0°, reduced frequency is 0.077, and Reynolds number is 0.98 million. **Left:** Lift. **Middle:** Drag. **Right:** Moment.

Chapter 7

WindPACT Flutter Analysis

Flutter data for wind turbine blades is very limited. This is mainly owing to the fact that blades up until recently have been small enough that flutter was not a real concern. The baseline blade developed for the WindPACT rotor design study is one of the few blades that has been the subject of any flutter analyses. This chapter presents the results of flutter predictions for this blade using generalized forces derived from inviscid and fully turbulent CFD simulations. The blade geometric and structural properties are presented first followed by a steady aerodynamic simulation. The results of the flutter analysis and the associated unsteady aerodynamics are given in the final portion of the chapter.

7.1 Model Properties

The WindPACT rotor design study was conducted between 2000 and 2002 by Global Energy Concepts, LLC and Windward Engineering [50]. The overall purpose of the WindPACT project was to identify ways to reduce the cost of wind energy per kWh. The baseline 1.5 MW rotor design from this project is analyzed here. The rotor characteristics are summarized in Table 7.1. It is important to realize that this rotor is purely conceptual, and no prototypes were built or tested. The rotor was meant to be representative of a MW scale wind turbine used in onshore wind energy production.

Table 7.1: Characteristics of 1.5 MW Baseline WindPACT Blade

Characteristic	Unit	Value
Rotor diameter	m	70
Max. rotor speed	rpm	20.5
Max. tip speed	m/s	75
Blade coning	deg	0
Max. blade chord	m	8% of radius
Radius to blade root	m	5% of radius
Blade mass	kg	4230

The rotor blade is twisted 11.1 degrees from root to tip. The airfoil profiles are derived from the S818, S825, and S826 series. Thicker versions of these profiles were used since manufacturing limitations at the time suggested that the original profiles were too thin for such a massive blade. The blade planform and cross-sections are shown in Fig. 7.1. Clearly evident is the twist and tapering along the blade span.

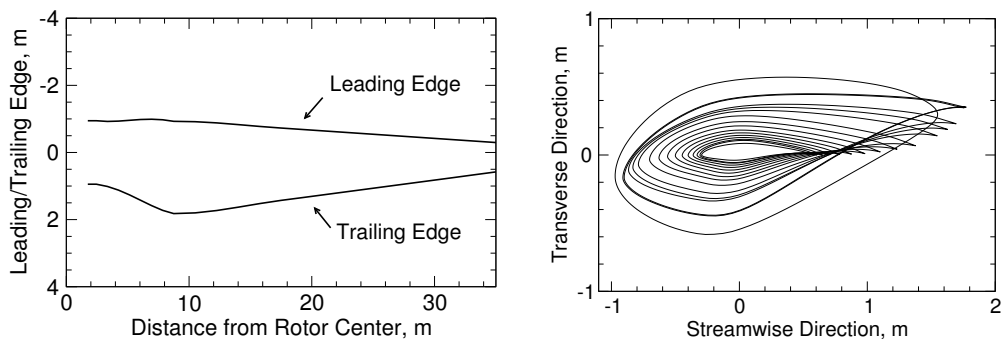

Figure 7.1: WindPACT 1.5 MW blade geometry. **Left:** Blade planform. **Right:** Blade profiles from near root to tip.

7.2 Structural Analysis

Since no physical model exists with which to extract experimental mode shape data for the WindPACT blade, finite element modeling is required. Several models of the blade have been created and results published. Results from RCAS (Rotorcraft Comprehensive Analysis System) and BModes generally agree very well. The former

is a mature tool developed for rotorcraft analysis that was subsequently used by NREL for wind turbine aeroelastic modeling and analysis [7]. The latter is a code developed by NREL for use in FAST [8]. Sandia National Laboratories created a finite element model in NASTRAN for modal extraction [48], but that model is not readily available. Sandia has also created a blade design system in MATLAB known as NuMAD [5]. This program is capable of outputting an FEA model that can be read directly by ANSYS. The 1.5 MW WindPACT blade is included in the distribution as a program demo.

The demo included with NuMAD was used to generate an ANSYS finite element model of the 1.5 MW WindPACT blade. However, this model did not match the modal frequencies listed in various other reports. This shortcoming is documented in the NuMAD manual. Fine tuning of the material properties is suggested to better match published data. In this work, all densities were reduced to 75% of their given values. The modal frequencies of this model are compared with several others in Table 7.2 for the first six mode shapes at several rotor speeds. The first and third modes correspond to the first and second flapwise modes. The second and fourth modes correspond the first and second edgewise modes. The sixth mode corresponds to the first torsional mode.

It is possible for resonant vibrations to occur if the rotor operational speed matches the natural frequencies of the blades. A Campbell diagram graphically shows possible resonant points by plotting multiples of the rotor speed (1E, 2E, etc.) with the natural frequencies of the system. A Campbell diagram for the WindPACT blade is shown in Fig. 7.2. Points of intersection should be avoided during wind turbine operation. This analysis, however, does not take into account other structural frequencies of the wind turbine such as the tower, which could also lead to resonant conditions.

The first, second, third, and sixth modes, which correspond to those used by Lobitz [48] in his flutter analysis, are shown in Fig. 7.3. Looking at Table 7.2, the modal frequencies among the models tend to vary more as the mode number

Table 7.2: WindPACT Natural Frequencies (Hz)

Mode	Rotor Speed (rad/s)	RCAS	BModes	ANSYS	Lobitz
Mode 1	0	1.229	1.228	1.212	1.199
Mode 2		1.875	1.869	1.964	1.714
Mode 3		3.662	3.658	3.372	3.596
Mode 4			6.291	5.740	
Mode 5			7.970	7.354	
Mode 6			10.17	11.57	9.846
Mode 1	2	1.300	1.298	1.277	
Mode 2		1.889	1.883	2.000	
Mode 3		3.736	3.733	3.448	
Mode 4			6.323	5.777	
Mode 5			8.043	7.425	
Mode 6			10.17	11.64	
Mode 1	4		1.484	1.454	
Mode 2			1.924	2.101	
Mode 3			3.948	3.665	
Mode 4			6.418	5.886	
Mode 5			8.257	7.635	
Mode 6			10.18	11.85	

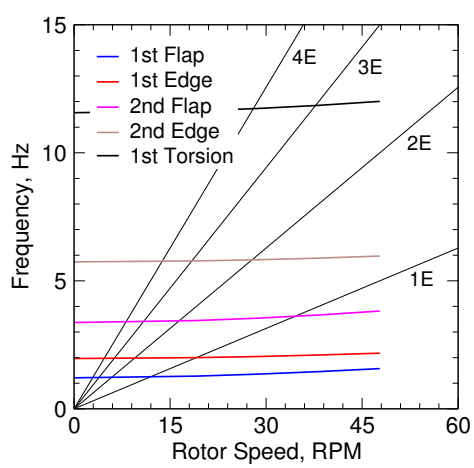

Figure 7.2: Campbell diagram for WindPACT rotor blade.

increases. However, these results suggest that the current structural model is sufficient to compare trends in flutter predictions for the 1.5 MW WindPACT turbine blade.

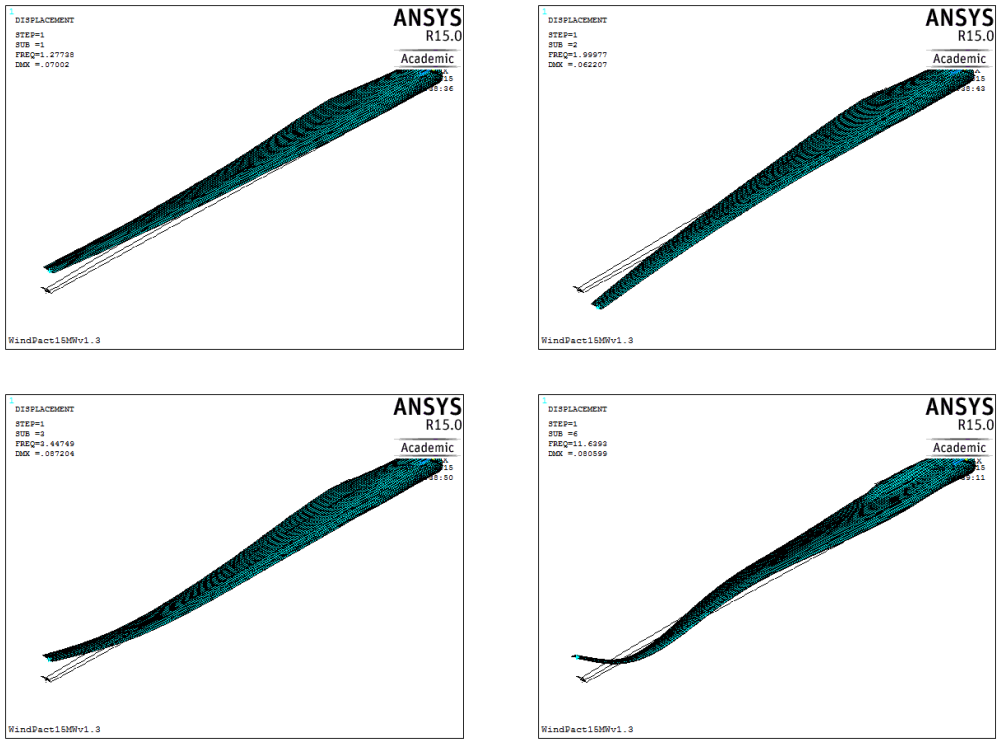

Figure 7.3: Computed mode shapes for WindPACT blade rotating at 2 rad/s. **Top Left:** Mode one (1st flapwise) 1.28 Hz. **Top Right:** Second Mode (1st edgewise) 2.00 Hz. **Bottom Left:** Third mode (2nd flapwise) 3.45 Hz. **Bottom Right:** Sixth mode (1st torsion) 11.64 Hz.

7.3 Steady Aerodynamics

In addition to a structural model, a flutter analysis also requires an aerodynamic model. As was done with the AGARD 445.6, the harmonic balance solver can be used with small amplitude motions of each mode shape to generate the required generalized aerodynamic forces. Before proceeding to an unsteady analysis, it is worth documenting the results from a steady analysis. In this section, an inviscid and fully turbulent simulation of the WindPACT rotor operating near twice the max

speed is examined. This speed (42 RPM or $M_{tip} = 0.45$) was chosen as a starting point for flutter analysis since Lobitz [48] and Owens et al. [57] both observed flutter near the same speed.

An inviscid C-H grid and a viscous C-H grid are used to conduct the steady, inviscid and turbulent simulations, respectively. The inviscid grid contains 193 x 41 x 49 nodes, with 25 nodes on the airfoil in the spanwise direction and 129 nodes on the airfoil in the wrap around direction. The viscous grid (Fig. 7.4) contains 257 x 65 x 33 nodes, with 17 nodes on the airfoil in spanwise direction, 193 nodes on the airfoil in the wrap around direction, and a y+ value of approximately 2.5 at the blade surface. This grid is intentionally coarse for a turbulent simulation to minimize computation times. Simulations need to be performed on finer grids in the future. In both cases, the far field is approximately two blade lengths from the hub, and the side faces of the domain are periodic.

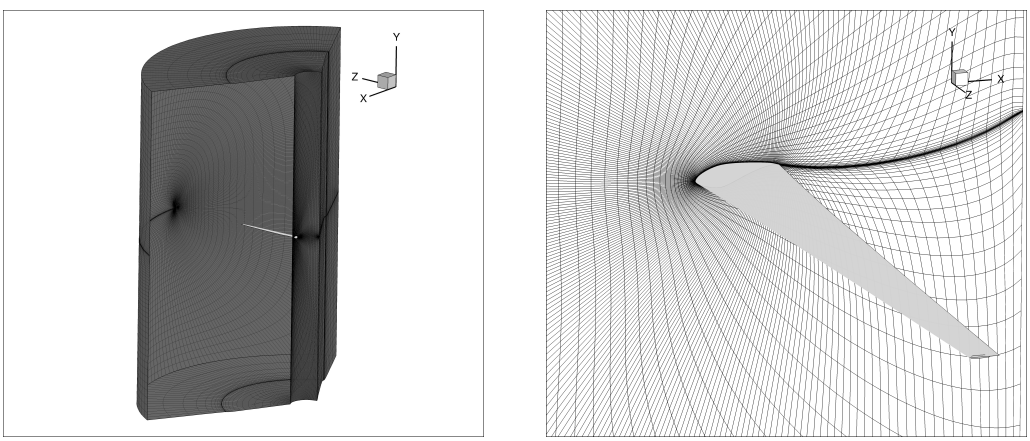

Figure 7.4: Viscous WindPACT C-H grid (257 x 65 x 33). The grid on the right shows the blade starting at 39% span.

For steady aerodynamics, the force on the blade is largely due to the pressure distribution on the blade. Pressure distributions at 5 spanwise stations along the blade are shown in Fig. 7.5. There is no experimental data for comparison, but there are a couple of distinguishing features between the inviscid and turbulent simulations. At all spanwise locations, the results differ over the aft half of the respective airfoil

section. This is not surprising given the results in Chapter 6 where the critical region of wind turbine type airfoils was shown to be in the aft portion of the airfoil. The results tend to agree the most between 62 and 87 percent span. The blade cross-section becomes increasingly thick and round as one moves toward the hub. It is easy to see that an inviscid simulation would be inaccurate here. At the blade tip, vortical structures are lost in an inviscid simulation, and this probably contributes to the increased disagreement near the blade tip.

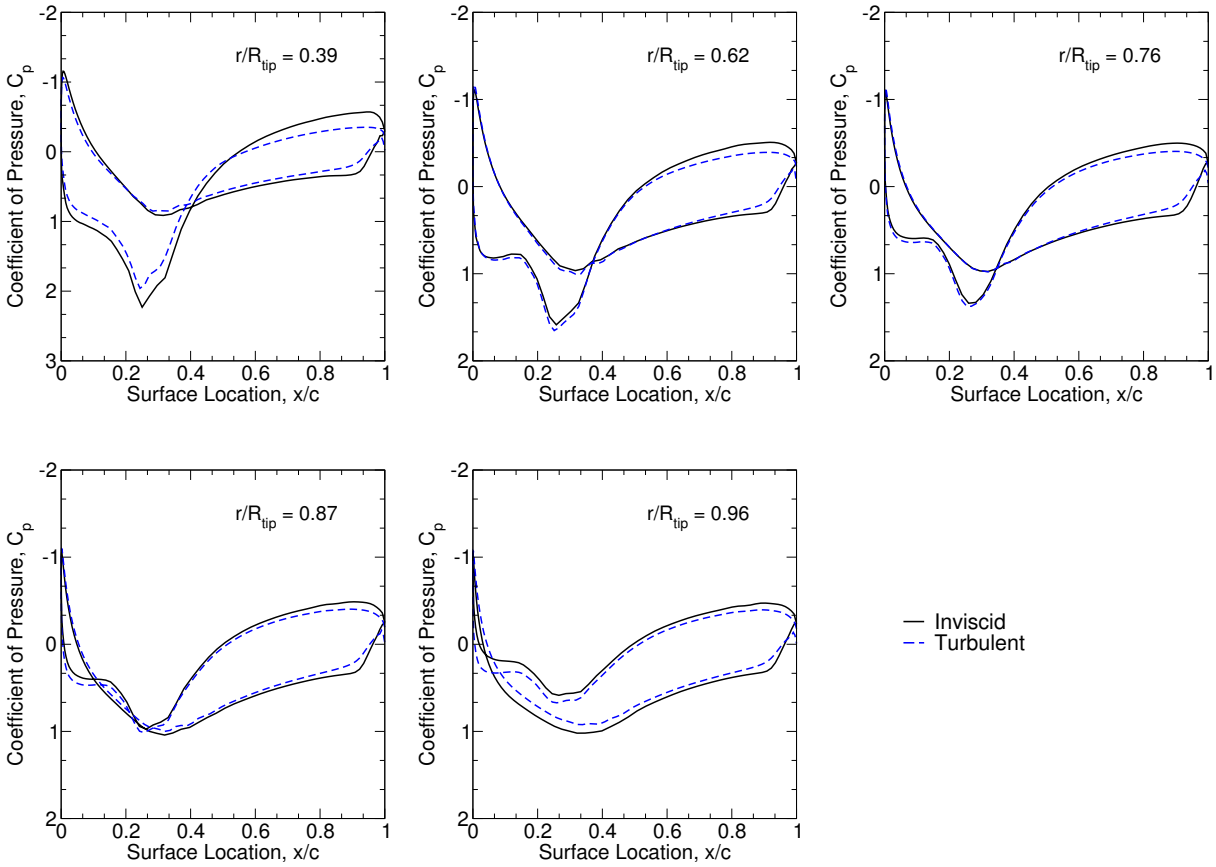

Figure 7.5: Coefficient of pressure distribution for 1.5 MW WindPACT rotor operating at 42 RPM in still air.

7.4 Flutter Analysis

The flutter solution requires complex generalized forces for each considered mode shape. Previous work by Lobitz [48] and Owens et al. [57] suggests that the dominant modes for flutter are the 2nd flapwise and edgewise modes and 1st torsional mode. These three modes are included in the forthcoming analysis as well as the 1st flapwise and edgewise modes. Each of the five mode shapes considered requires a single unsteady aerodynamic solution using a real, small amplitude motion of the respective mode shape. For example, the unsteady aerodynamics for the 2nd flapwise mode are computed by using a 10^{-4} amplitude unsteady grid motion. This unsteady aerodynamic solution gives five complex generalized forces, which are the sensitivities of the five mode shapes being considered to displacements of the 2nd flapwise mode.

Lobitz and Owens et al. both observed flutter around 42 RPM ($M_{tip} = 0.45$). To ensure flutter conditions and test the viability of the technique, a slightly higher rotor speed of 46.4 RPM ($M_{tip} = 0.50$) is considered first. Figures 7.6 to 7.10 show inviscid and fully turbulent generalized forces for the five modes considered at reduced frequencies of 0.12, 0.24, and 0.36. Given that inviscid solutions are very limited in accuracy for wind turbine airfoils, it is not surprising to see the differing generalized forces between inviscid and fully turbulent solutions.

The generalized forces can be used in Eq. 4.12 to determine the flutter solution if it exists. Recall in the derivation of Eq. 4.12 that the structural damping was neglected. Thus, the results here are considered a worst case scenario since all damping must be aerodynamic damping. Including all five modes (1st and 2nd flapwise, 1st and 2nd edgewise, and 1st torsional), the fully turbulent generalized force data predicts a flutter frequency of $\bar{\omega} = 0.232$. A sample calculation is provided in Table 7.3 to show how this number is determined. The reduced frequency, $\bar{\omega}$, is varied until the imaginary part of the reduced velocity, V_f, changes sign. This indicates the existence of a purely real reduced velocity in this frequency range. A value of $\bar{\omega}$ which gives a vanishingly small imaginary value then can be taken as the flutter frequency.

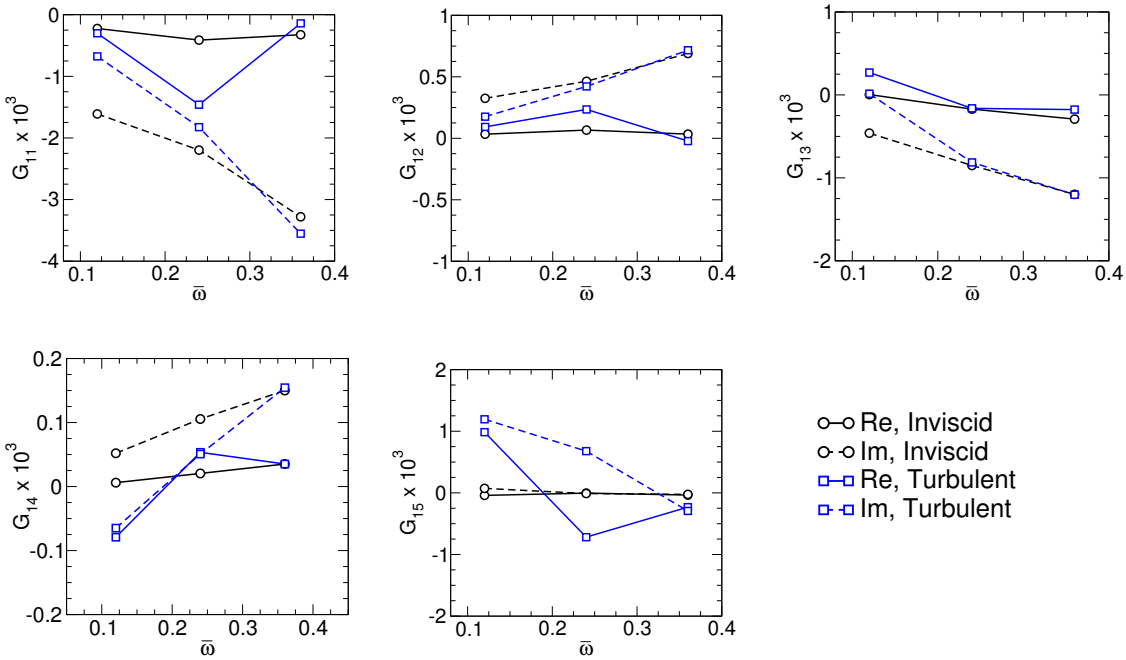

Figure 7.6: Generalized aerodynamic forces for mode shape one with $M_{tip} = 0.500$.

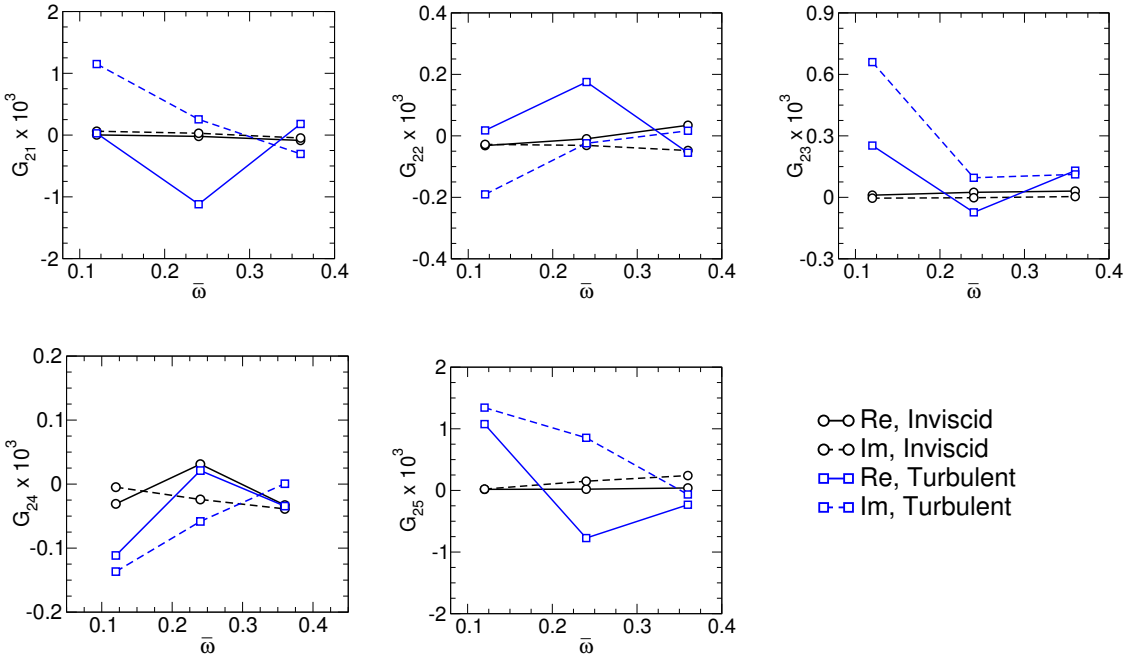

Figure 7.7: Generalized aerodynamic forces for mode shape two with $M_{tip} = 0.500$.

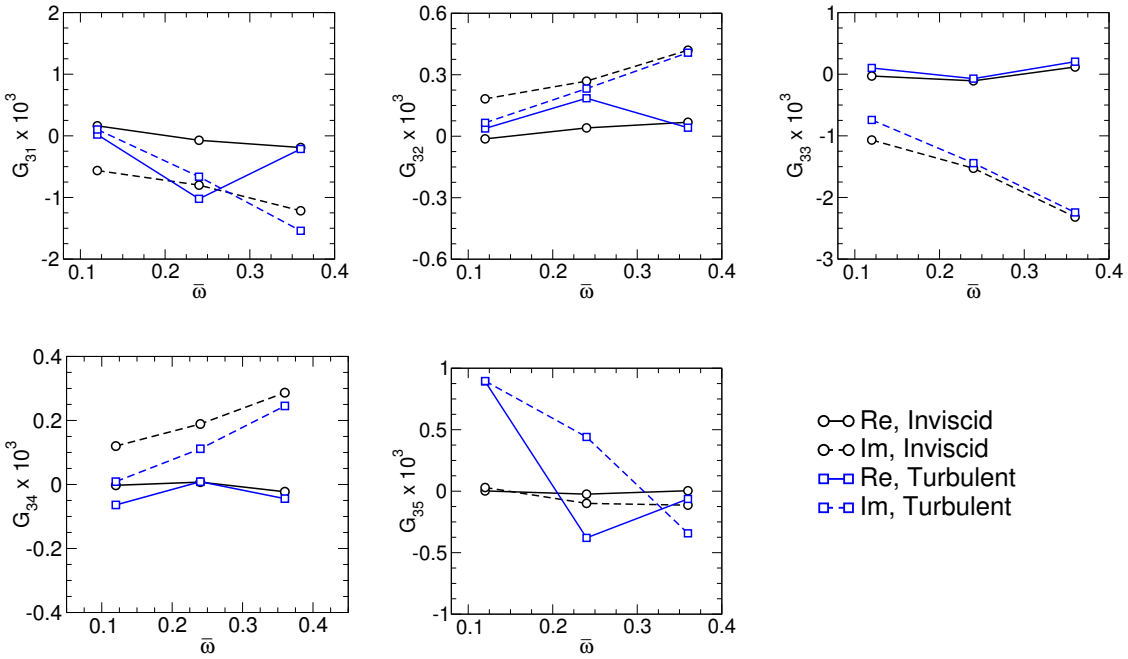

Figure 7.8: Generalized aerodynamic forces for mode shape three with $M_{tip} = 0.500$.

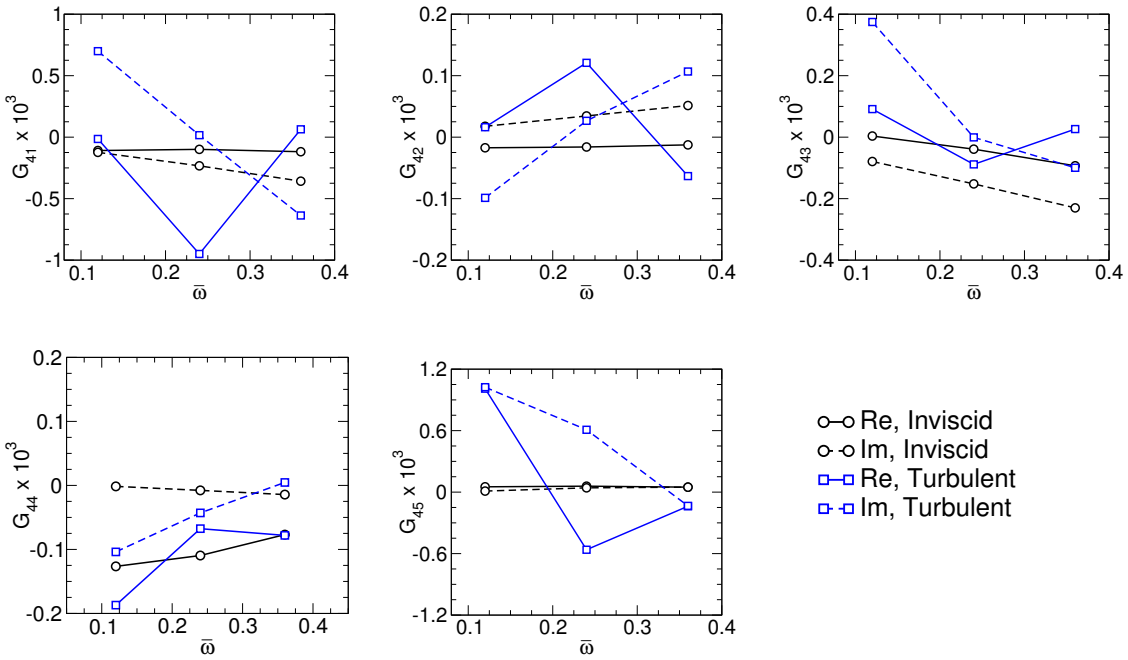

Figure 7.9: Generalized aerodynamic forces for mode shape four with $M_{tip} = 0.500$.

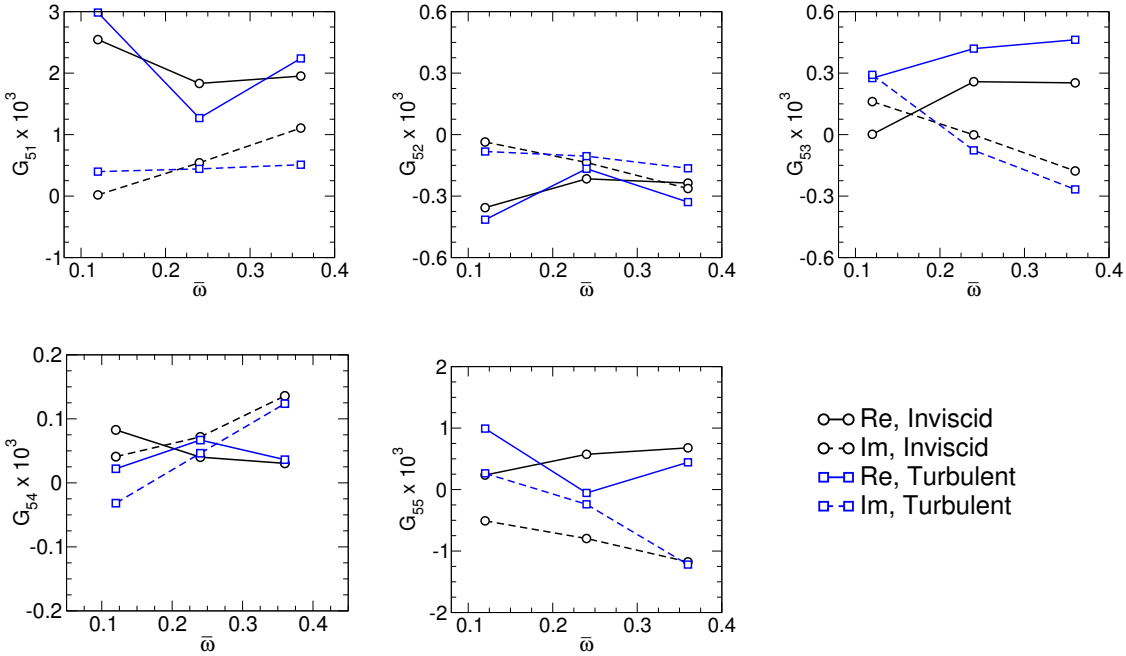

Figure 7.10: Generalized aerodynamic forces for mode shape six with $M_{tip} = 0.500$.

Table 7.3: Sample WindPACT Flutter Calculation, $M_{tip} = 0.500$

$\bar{\omega}$	V_f	Determinant
0.230	$0.0647 - 1.55\times10^{-6}\ i$	$2.28\times10^{-9} - 1.45\times10^{-9}\ i$
0.231	$0.0645 - 7.23\times10^{-7}\ i$	$1.09\times10^{-9} - 6.82\times10^{-10}\ i$
0.232	$0.0642 + 7.71\times10^{-8}\ i$	$9.46\times10^{-11} + 1.12\times10^{-10}\ i$

The two dominant modes are apparently the 1st flapwise and 1st edgewise modes. Including only these two modes in the analysis has a negligible effect on the predicted flutter frequency. Much like the AGARD 445.6 case, flutter analysis can be reduced to these two modes only without loss of accuracy. The torsional mode, which is fundamental to classic flutter, does not play a role in this case. As Lobitz [48] points out, the natural twist of the blade moving in the edgewise direction reproduces the effect of a torsional mode. Interestingly, the inviscid data does not admit a flutter solution within the reduced frequency range considered. The real and imaginary components of the unsteady pressure for the 1st flapwise and 1st edgewise modes are shown at several blades spans in Figs. 7.11 and 7.12 for inviscid and turbulent cases. These plots highlight the differences between the inviscid and turbulent generalized forces along the blade span for these modes. The largest disagreement is near the rotor hub where the thick airfoils make accurate inviscid modeling impossible. Near the blade tips, where the airfoil sections are more streamlined, the inviscid and turbulent models have much better agreement.

Given the importance of the generalized forces, it is useful to examine the first harmonics of the real and imaginary pressures. The imaginary pressure manifests itself as the imaginary generalized force. For stability, this value should be negative. Integration of these pressure distributions largely determines the generalized forces (the shear stress slightly alters the generalized force in turbulent simulations). Figures 7.13 and 7.14 show the unsteady pressure distributions for the first and second mode shapes. The pressures near the hub appear are very similar in both cases. Moving outboard, differences between the two modes begin to emerge. Looking back at Fig. 7.3, the reason is that displacements near the root are minimal in all cases due to the required structural stiffness near the root. The outer portions of the blade are where the critical generalized forces develop.

Flutter for two other rotor speeds is calculated using generalized force data from additional CFD simulations. The tip Mach number is decreased to 0.475 and increased to 0.525 to observe any trends in flutter related to rotor speed. Only the first two

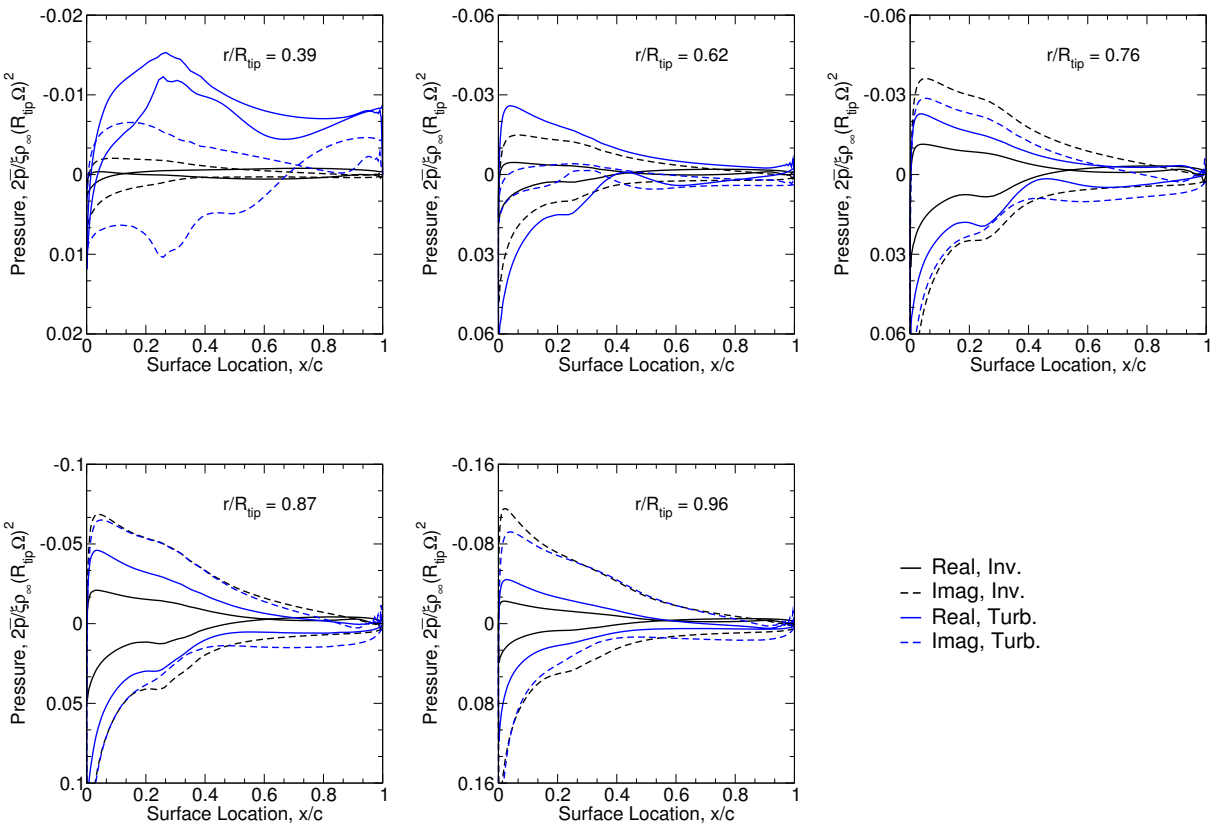

Figure 7.11: Real and imaginary pressures for 1st flapwise mode for 1.5 MW WindPACT rotor operating at $M_{tip} = 0.500$.

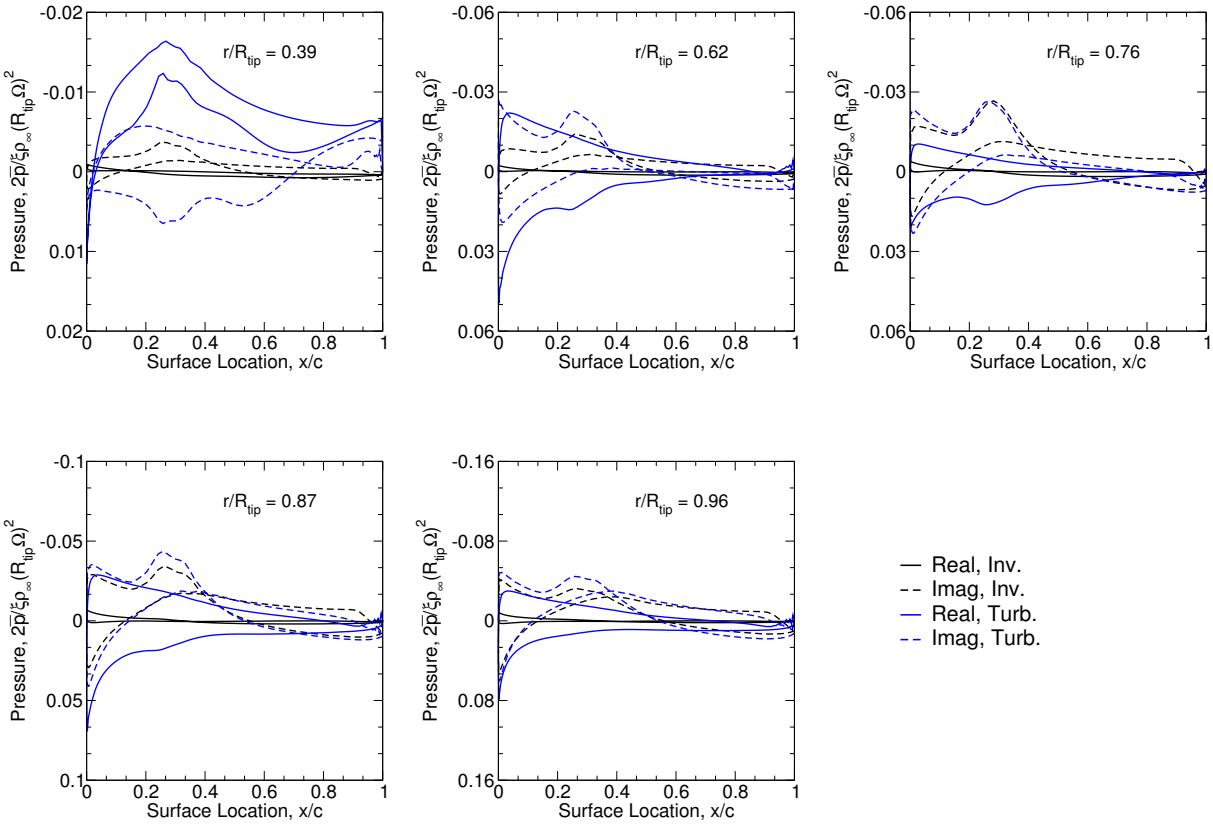

Figure 7.12: Real and imaginary pressures for 1st edgewise mode for 1.5 MW WindPACT rotor operating at $M_{tip} = 0.500$.

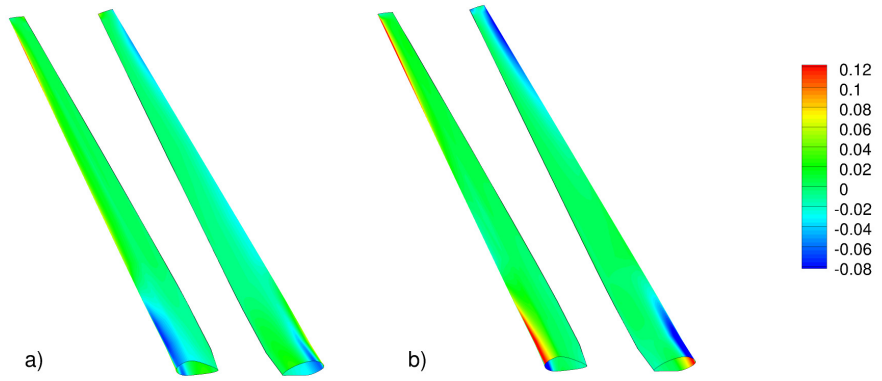

Figure 7.13: Unsteady pressure distributions ($\bar{p}/0.5\rho U_{tip}^2$) on suction and pressure sides of WindPACT blade surface for first flapwise mode with $M_{tip} = 0.500$. Real component is shown in (a), and imaginary component is shown in (b).

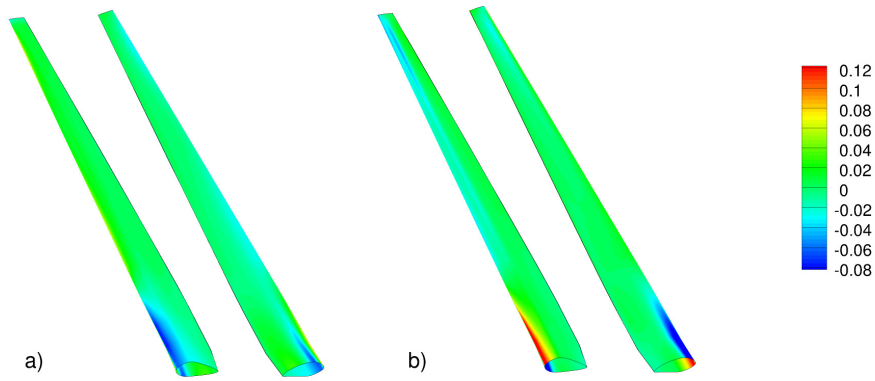

Figure 7.14: Unsteady pressure distributions ($\bar{p}/0.5\rho U_{tip}^2$) on suction and pressure sides of WindPACT blade surface for first edgewise mode with $M_{tip} = 0.500$. Real component is shown in (a), and imaginary component is shown in (b).

mode shapes are considered now given the results of the previous flutter analysis. The required generalized forces are shown in Figs. 7.15 to 7.18. The predicted reduced frequency does not vary much over this range with $\bar{\omega} = 0.223$ and $\bar{\omega} = 0.233$ for $M_{tip} = 0.475$ and $M_{tip} = 0.525$, respectively.

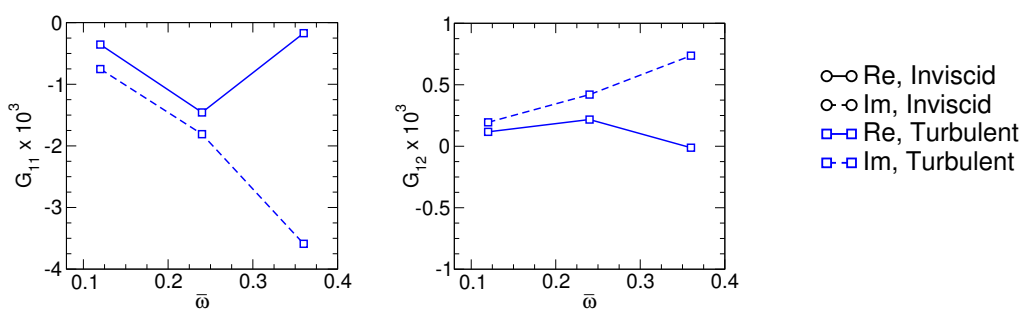

Figure 7.15: Generalized aerodynamic forces for mode shape one with $M_{tip} = 0.475$.

Only Lobitz provides flutter predictions over a range of rotor speeds. Fig. 7.19 compares the predicted flutter frequency ratios vs. rotor speed from Lobitz's analysis and the current analysis. The flutter frequency is normalized in both the traditional way using ω_α and using ω_2. Given that the second mode (1st edgewise) acts as the torsional mode in this case, it may be a more appropriate scaling. The comparison is more qualitative given the known differences in the respective structural models, but

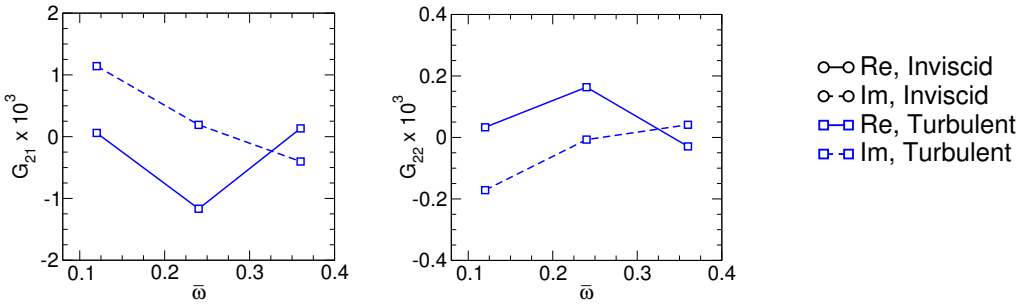

Figure 7.16: Generalized aerodynamic forces for mode shape two with $M_{tip} = 0.475$.

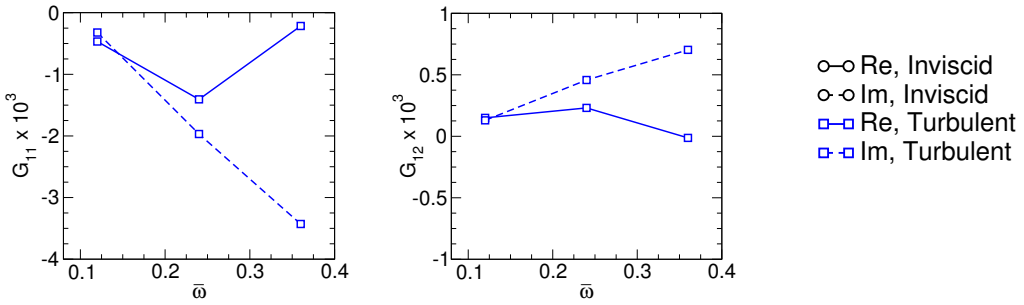

Figure 7.17: Generalized aerodynamic forces for mode shape one with $M_{tip} = 0.525$.

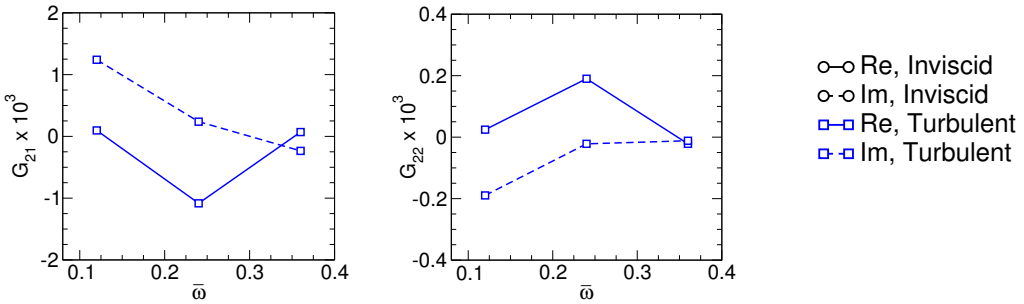

Figure 7.18: Generalized aerodynamic forces for mode shape two with $M_{tip} = 0.525$.

the predicted frequency ratios are similar in magnitude with the average difference over the rotor speed considered being about 8%. Interestingly, the solutions appear to converge at higher rotor speeds. This could be similar to the AGARD 445.6 where predictions typically diverge between models at lower free stream speeds but tend to agree at higher subsonic speeds.

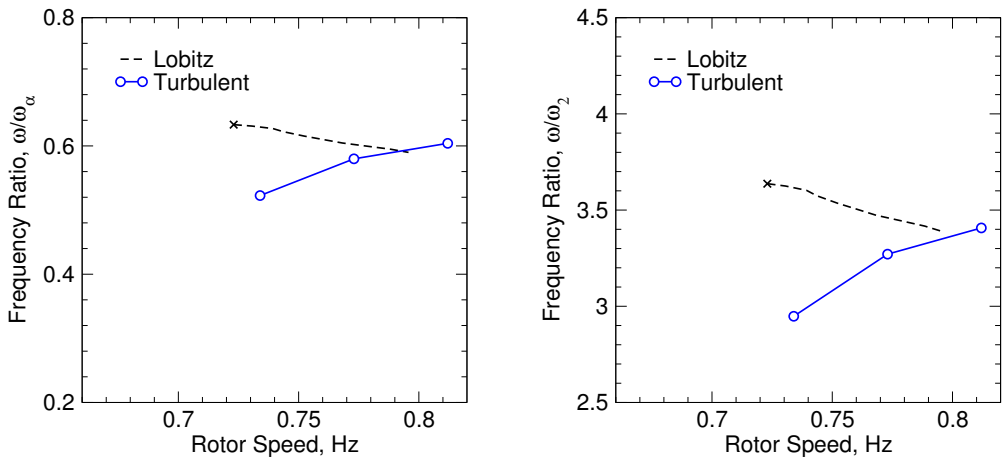

Figure 7.19: Frequency ratio

Chapter 8

Conclusion

8.1 Summary

An aeroelastic model was developed in this dissertation driven by unsteady aerodynamic solutions via the harmonic balance method and a mode shape-based structural dynamics model. This is the first aeroelastic model of its kind to be applied to a wind turbine blade. The model allows for blade motions in the flapwise, edgewise, and torsional directions. Compared to traditional wind turbine aeroelastic models that rely on blade element momentum theory for aerodynamic loads, this model is significantly more robust since the unsteady RANS equations are used to compute the aerodynamic loads. The computational workload associated with the unsteady RANS equations is normally too high to be useful in any realistic scenario, but the harmonic balance method reduces the workload 5 to 10 times keeping solution times manageable. Analysis of the 1.5 MW WindPACT wind turbine blade gave flutter predictions similar to predictions from another published aeroelastic model with an average difference in frequency ratio of about 8% between models.

The first known application of the $\gamma - \overline{\mathrm{Re}_{\theta t}}$ transition model in combination with the harmonic balance method to study unsteady wind turbine flows also appeared in the dissertation. Other authors have shown the necessity of a transition model

to accurately predict static stall of wind tubrine airfoils. Pitching S809 airfoils were analyzed in this dissertation with a fully turbulent model and transition model. The transition model was shown to be far more capable in predicting the onset of dynamic stall than the fully turbulent model.

8.2 Future Work

Inclusion of the transition model into the aeroelastic model is the next logical step in this work. While the implementation is straightforward from the 2-D work presented herein, a significant departure from the fully turbulent flutter predictions is not expected for the WindPACT case considered. The parameters of that case were chosen over a decade ago with the intent to keep the aerodynamics as simple as possible. More interesting results should be encountered if the angle of attack of the blade is changed so that portions of the blade experience dynamic stall.

The current method of flutter solution is somewhat tedious in that a range of generalized forces over a range of frequencies are required to find the flutter condition if it exists. A better approach might be to automate the process such that the flutter condition is automatically found by the solver. Limit cycle oscillation (LCO) frequency finding procedures have been applied to turbomachinery problems, and it should be possible to extend them to wind turbine blades.

Along the same lines as an automated procedure, a fully coupled aeroelastic model should also be developed from the aerodynamic and structural models presented here. In this scenario, the aerodynamic and structural models would be solved simultaneously with the current solution from each solver. Updates of the computational grid might limit the efficiency of the process so an optimal grid updating interval would need to be investigated.

Bibliography

[1] Abu-Ghannam, B. J. and Shaw, R. (1980). Natural transition of boundary layers-the effects of turbulence, pressure gradient, and flow history. *Journal of Mechanical Engineering Science*, 22(5):213–228. 5

[2] Agarwal, R. K. and Deese, J. E. (1987). Euler calculations for flowfield of a helicopter rotor in hover. *Journal of Aircraft*, 24(4):231–238. 17

[3] Agarwal, R. K. and Deese, J. E. (1989). Navier-Stokes calculations of the flowfield of a helicopter rotor in hover. In *26th Aerospace Sciences Meeting*, Reno, NV. AIAA 88-0106. 17

[4] Anderson, C., Heerkes, H., and Yemm, R. (1999). The use of blade-mounted dampers to eliminate edgewise stall vibration. In *European Wind Energy Conference*, Nice, France. 9

[5] Berg, J. C. and Resor, B. R. (2012). Numerical manufacturing and design tool (NuMAD v2.0) for wind turbine blades: Users guide. Sandia Report SAND2012-7028, Sandia National Laboratories. 109

[6] Bijl, H., Lucor, D., Mishra, S., and Schwab, C. (2013). *Uncertainty Quantification in Computational Fluid Dynamics*. Springer, Switzerland. 81

[7] Bir, G. S. (2005). Structural dynamics verification of rotorcraft comprehensive analysis system (RCAS). Technical Report NREL/TP-500-35328, National Renewable Energy Laboratory. 109

[8] Bir, G. S. (2007). Users guide to BModes (software for computing rotating beam coupled modes). Technical report, National Renewable Energy Laboratory. 109

[9] Bisplinghoff, R. L., Ashley, H., and Halfman, R. L. (1996). *Aeroelasticity*. Dover Publications. 7

[10] Blazek, J. (1993). Investigations of the implicit LU-SSOR scheme. Technical Report DLR-FB 93-51, DLR. 50

[11] Blazek, J. (2001). *Computational Fluid Dynamics: Principles and Applications*. Elsevier, first edition. 36, 42, 45, 140

[12] Boussinesq, J. (1877). *Essai sur la théorie des eaux courantes*. Mem. Pres. Acad. Sci., XXIII, 46, Paris. 19

[13] Boussinesq, J. (1896). *Theorie de l' écoulement tourbillonant et tumulteur des liquides dans les lits rectiligues*. Comptes Rendus de l' Acad. des Sciences, CXXII. 19

[14] Brandt, A. (2007). *Guide to Multigrid Development*. Elsevier, second edition. 61

[15] Campobasso, M. S. and Baba-Ahmadi, M. H. (2011). Analysis of unsteady flows past horizontal axis wind turbine airfoils based on harmonic balance compressible Navier-Stokes equations with low-speed preconditioning. In *Proceedings of Gas Turbine Tecnical Congress and Exposition*, Vancouver, Canada. GT2011-45303. 6

[16] Caradonna, F. X. and Tung, C. (1981). Experimental and analytical studies of a model helicopter rotor in hover. NASA/TM 81232, NASA Ames Research Center, Moffett Field, CA. 82

[17] Carlson, J.-R. (2011). Inflow/outflow boundary conditions with application to FUN3D. NASA/TM 2011-7181, Langley Research Center, Hamtpon, VA. 57

[18] Chaviaropoulos, P. K. (1999). Flap/lead-lag aeroelastic stability of wind turbine blade sections. *Wind Energy*, 2:99–112. 9

[19] Choi, Y. H. and Merkle, C. L. (1993). The application of preconditioning in viscous flows. *Journal of Computational Physics*, 105(2):207–223. 66

[20] Courant, R., Friedrichs, K. O., and Lewy, H. (1928). Über die partiellen differenzengleichungen der mathmatischen physik. *Math. Ann.*, 100:32–74. 45

[21] Davis, S. S. (1982). NACA 64a010 (NASA Ames model) oscillatory pitching. AGARD Report 702. Data Set 2. 78

[22] Ekici, K. and Hall, K. C. (2008). Nonlinear frequency-domain analysis of unsteady flows in turbomachinery with multiple excitation frequencies. *AIAA Journal*, 46(8):1912–1920. 27

[23] Ekici, K. and Hall, K. C. (2011). Harmonic balance analysis of limit cycle oscillations in turbomachinery. *AIAA Journal*, 49(7):1478–1487. 6, 87

[24] Ekici, K., Hall, K. C., and Dowell, E. H. (2008). Computationally fast harmonic balance methods for unsteady aerodynamic predictions of helicopter rotors. *Journal of Computational Physics*, 227:6206–6225. 81

[25] Ekici, K., Hall, K. C., and Kielb, R. E. (2010). Harmonic balance analysis of blade row interactions in a transonic compressor. *Journal of Propulsion and Power*, 26(2):335–343. 6

[26] Fung, Y. C. (1993). *An Introduction to the Theory of Aeroelasticity*. Dover Publications, Inc. 10

[27] Glauert, H. (1935). Airplane propellers. In *Aerodynamic Theory*, pages 169–360. 3

[28] Gopinath, A. K. and Jameson, A. (2005). Time spectral method for periodic unsteady computations over two- and three- dimensional bodies. In *43rd AIAA Aerospace Sciences Meething*, Reno, NV. 78, 79

[29] Guillard, H. and Viozat, C. (1999). On the behaviour of upwind schemes in the low Mach number limit. *Computers & Fluids*, 28:63–86. 69

[30] Hall, K. C., Thomas, J. P., and Clark, S. W. (2002). Computation of unsteady nonlinear flows in cascades using a harmonic balance technique. *AIAA Journal*, 40:879–886. 6

[31] Hansen, M. O. L., Sorensen, J. N., Voutsinas, S., Sorensen, N., and Madsen, H. A. (2006). State of the art in wind turbine aerodynamics and aeroelasticity. *Progress in Aerospace Sciences*, 42:285–330. 3, 9

[32] Hirsch, C. (2007). *Numerical Computation of Internal and External Flows: The Fundamentals of Computational Fluid Dynamics*. Elsevier, second edition. 14, 57, 140

[33] Holierhoek, J. G. (2008). *Aeroelasticity of Large Wind Turbines*. PhD thesis, Technische universiteit Delft. 7

[34] Im, H.-S. (2012). *High Fidelity Simulation of a Non-Synchronous Vibration for Aircraft Engine Fan/Compressor*. PhD thesis, University of Miami. 70

[35] Jameson, A. (1983). Solution of the Euler equations for two-dimensional transonic flow by a multigrid method. MAE Report 1613, Princeton University. 61

[36] Jameson, A. and Baker, T. J. (1983). Solution of the Euler equations for complex configurations. AIAA 81-1929. 61

[37] Jameson, A., Schmidt, W., and Turkel, E. (1981). Numerical solution of the Euler equations by finite volume methods using Runge-Kutta time-stepping schemes. In *AIAA 14th Fluid and Plasma Dynamics Conference*, Palo Alto, CA. AIAA 1981-1259. 35, 36, 46

[38] Jonkman, J. M. and Buhl, Jr., M. L. (2005). FAST user's guide. Technical Report NREL/EL-500-38230, National Renewable Energy Laboratory. 11

[39] Langtry, R. B. (2006). *A Correlation-Based Transition Model using Local Variables for Unstructured Parallelized CFD Codes*. PhD thesis, University of Stuttgart. 5, 21, 77

[40] Langtry, R. B., Gola, J., and Menter, R. F. (2006). Predicting 2D airfoil and 3D wind turbine rotor performance using a transition model for general CFD codes. In *AIAA 44th Aerospace Sciences Meeting*, Reno, NV. AIAA 2006-0395. 5, 95

[41] Larsen, T. J. and Hansen, A. M. (2007). How 2 HAWC2, the user's manual. Technical Report Risø-R-1597(ver.3-1)(EN), RISØ. 11

[42] Larwood, S. M. (2015). Prediction and alleviation of flutter in swept wind turbine blades. In *33rd Wind Energy Symposium*, Kissimmee, FL. AIAA 2015-1464. 10

[43] Le Pape, A. and Lecanu, J. (2004). 3D Navier-Stokes computations of a stall-regulated wind turbine. *Wind Energy*, 7:309–324. 4

[44] Lee-Rausch, E. M. and Batina, J. T. (1995). Wing flutter boundary prediction using unsteady Euler aerodynamic method. *Journal of Aircraft*, 32(2):416–422. 91

[45] Lee-Rausch, E. M. and Batina, J. T. (1996). Wing flutter computations using an aerodynamic model based on the Navier-Stokes equations. *Journal of Aircraft*, 33(6):1139–1147. 89

[46] Leishman, J. G. and Beddoes, T. S. (1989). A semi-empirical model for dynamic stall. *Journal of the American Helicopter Society*, 34(3):3–17. 4, 98

[47] Liu, F. and Zheng, X. (1996). A strongly coupled time-marching method for solving Navier-Stokes and k-ω turbulence model equations with multigrid. *Journal of Computational Physics*, 128:289–300. 48

[48] Lobitz, D. W. (2004). Aeroelastic stability predictions for a MW-sized blade. *Wind Energy*, 7:211–224. 10, 109, 112, 114, 118

[49] Lundsager, P., Petersen, H., and Frandsen, S. (1981). The dynamic behavior of the stall-regulated Nibe A wind turbine: Measurements and a model for stall-induced vibrations. Technical Report Risø-M-2253, RISØ. 9

[50] Malcolm, D. J. and Hansen, A. C. (2002). WindPACT turbine rotor design study. Subcontractor Report NREL/SR-500-32495, National Renewable Energy Laboratory. Revised 2006. 107

[51] Martinelli, L. (1987). *Calculations of Viscous Flows with a Multigrid Method*. PhD thesis, Princeton University. 38

[52] Mayle, R. E. (1991). The role of laminar-turbulent transition in gas turbine engines. *ASME Journal of Turbomachinery*, 113(4):509–537. 5

[53] McMullen, M., Jameson, A., and Alonso, J. J. (2002). Application of a non-linear frequency domain solver to the Euler and Navier-Stokes equations. In *40th AIAA Aerospace Sciences Meeting*, Reno, NV. AIAA 2002-0120. 78, 79, 87

[54] Medida, S. and Baeder, J. D. (2011). Application of the correlation-based γ–$\overline{\mathrm{Re}_{\theta t}}$ transition model to the Spalart-Allmaras turbulence model. In *20th AIAA Computational Fluid Dynamics Conference*, Honolulu, HI. AIAA 2011-3979. 6, 21, 22, 23, 24, 77, 78

[55] Menter, F. R. (1994). Two-equation eddy-viscosity turbulence models for engineering applications. *AIAA Journal*, 32(8):1598–1605. 16

[56] Merci, B., Steelant, J., Vierendeels, J., Riemslagh, K., and Dick, E. (2000). Computational treatment of source terms in two-equation turbulence models. *AIAA Journal*, 38(11):2085–2093. 48

[57] Owens, B. C., Griffith, D. T., Resor, B. R., and Hurtado, J. E. (2013). Impact of modeling approach on flutter predictions for very large wind turbine blade designs. In *American Helicopter Society 69th Annual Forum*, Phoenix, AZ. Paper No. 386. 10, 112, 114

[58] Øye, S. (1991). Dynamic stall, simulated as a time lag of separation. In *Proceedings of the 4th IEA Symposium on the Aerodynamics of Wind Turbines*, Harwell, UK. ETSU-N-118. 4

[59] P., T. J., Dowell, E. H., and C., H. K. (2002). Nonlinear inviscid aerodynamic effects on transonic divergence, flutter, and limit-cycle oscillations. *AIAA Journal*, 40(4):638–646. 72

[60] P., T. J., Dowell, E. H., and C., H. K. (2004). Modeling viscous transonic limit-cycle oscillation behavior using a harmonic balance approach. *Journal of Aircraft*, 41(6):1266–1274. 72

[61] Pavel, M. D. and Schoones, M. M. J. (1999). Literature survery on aeromechanical instabilities for helicopters and wind turbines. Memorandum M-877, TU Delft. 7, 11

[62] Pavel, M. D. and van Holten, T. H. (2000). A rotor-tower instability associated with the advancing lead/lag mode. In *2000 Wind Energy Symposium*, Reno, NV. AIAA 2000-0068. 11

[63] Petersen, J. T., Madsen, H. A., Bjorck, A., Enevoldsen, P., Øye, S., Ganander, H., and Winkelaar, D. (1998). Prediction of dynamic loads and induced vibrations in stall. Technical Report Risø-R-1045(EN), RISØ. 9

[64] Pitt, D. M. and Peters, D. A. (1983). Rotor dynamic inflow derivatives and time constants from various inflow models. In *9th European Rotorcraft Forum*, Stresa, Italy. 4

[65] Pulliam, T. H. and Steger, J. L. (1985). Recent improvements in efficiency, accuracy, and convergence for implicit approximate factorization schemes. In *23rd AIAA Aerospace Sciences Meeting*, Reno, NV. AIAA 85-0360. 52

[66] Ramsay, R. R., Hoffman, M. J., and Gregorek, G. M. (1995). Effects of grid roughness and pitch oscillations on the S809 airfoil. Technical Paper 442-7817, NREL. 93, 98

[67] Resor, B. R., Owens, B. C., and Griffith, D. T. (2012). Aeroelastic instability of very large wind turbine blades. In *European Wind Energy Association Annual Event*, Copenhagen, Denmark. 10

[68] Roe, P. L. (1981). Approximate Riemann solvers, parameter vectors, and difference schemes. *Journal of Computational Physics*, 43(2):357–372. 35, 38

[69] Schlichting, H. (1979). *Boundary Layer Theory*. McGraw-Hill, New York, 7th edition. 16

[70] Schmitt, V. and Charpin, F. (1979). Pressure distributions on the ONERA-M6-wing at transonic Mach numbers. In *Experimental Data Base for Computer Program Assessment*. Report of the Fluid Dynamics Panel Working Group 04. AGARD AR 138. 81

[71] Sharov, D. and Nakahashi, K. (1997). Reordering of 3D hybrid unstructured grids for vectorized LU-SGS Navier-Stokes calculations. In *13th Computational Fluid Dynamics Conference*. AIAA 97-2102. 52

[72] Slater, J. W. (2008). NPARC Alliance Validation Archive: ONERA M6 Wing. http://www.grc.nasa.gov/WWW/wind/valid/m6wing/m6wing.html. Accessed 2012. 81

[73] Smith, A. M. . O. and Gamberoni, N. (1956). Transition, pressure gradient and stability theory. Report ES 26388, Douglas Aircraft Company, Long Beach, CA. 5

[74] Somers, D. (1989). Design and experimental results for the S809 airfoil. Technical report, Airfoils, Inc., State College, PA. 93

[75] Spalart, P. R. and Allmaras, S. R. (1992). One-equation turbulence model for aerodynamic flows. In *30th Aerospace Sciences Meeting and Exhibit*, Reno, NV. AIAA 1992-0439. 16, 19

[76] Spekreijse, S. P. (1987). *Multigrid Solution of the Steady Euler Equations*. PhD thesis, Centrum voor Wiskunde en Informatica. 41

[77] Stiesdal, H. (1994). Extreme wind loads on stall regulated wind turbines. In *Proceedings of 16th British Wind Energy Association*, Stirling, UK. Mechanical Engineering Publications Ltd. 8

[78] Stokes, G. G. (1845). On the theories of the internal friction of fluids in motion and of the equilibrium and motion of elastic solids. *Trans. Cambridge Philos. Soc.*, 8:287–319. 16

[79] Swanson, R. C. and Radespiel, R. (1991). Cell centered and cell vertex multigrid schemes for the Navier-Stokes equations. *AIAA Journal*, 29(5):697–703. 43

[80] Swanson, R. C. and Turkel, E. (1992). On central-difference and upwind schemes. *Journal of Computational Physics*, 101(2):292–306. 38

[81] Swanson, R. C. and Turkel, E. (1997). Multistage schemes with multigrid for euler and navier-stokes equations. Technical Paper 3631, NASA, Hamtpon, VA. 44, 57

[82] Tai, C.-H., Sheu, J.-H., and Tzeng, P.-Y. (1996). Improvement of explicit multistage schemes for central spatial discretization. *AIAA Journal*, 34:185–188. 47

[83] Tai, C.-H., Sheu, J.-H., and van Leer, B. (1995). Optimal multistage schemes for euler equations with residual smoothing. *AIAA Journal*, 33:1008–1016. 47

[84] Tannehill, J. C., Anderson, D. A., and Pletcher, R. H. (1997). *Computational Fluid Mechanics and Heat Transfer*. Taylor and Francis, 2nd edition. 31

[85] Tatum, K. E. and Slater, J. W. (1999). The validation archive of the NPARC alliance. In *AIAA 37th Aerospace Sciences Meeting*, Reno, NV. AIAA 99-0747. 81

[86] Tongchitpakdee, C., Benjanirat, S., and Sankar, L. N. (2005). Numerical simulation of the aerodynamics of horizontal axis wind turbines under yawed flow conditions. In *AIAA 43rd Aerospace Sciences Meeting*, Reno, NV. AIAA 2005-0773. 4

[87] Turkel, E. (1987). Preconditioned methods for solving the incompressible and low speed compressible equations. *Journal of Computational Physics*, 72(2):1052–1070. 66

[88] Turkel, E., Fiterman, A., and van Leer, B. (1994). Preconditioning and the limit to the incompressible flow equations. Contractor Report 191500, NASA. 68

[89] Turkel, E., Radespiel, R., and Kroll, N. (1997). Assessment of preconditioning methods for multidimensional aerodynamics. *Computers & Fluids*, 26(6):613–634. 66, 68

[90] Turkel, E., Swanson, R. C., Vatsa, V. N., and White, J. A. (1991). Multigrid for hypersonic viscous two- and three-dimensional flows. AIAA 91-1572. 61

[91] Turkel, E., Vatsa, V. N., and Radespiel, R. (1996). Preconditioning methods for low-speed flows. In *Applied Aerodynamics Conference*, New Orleans, LA. AIAA 1996-2460. 68

[92] Van Albada, G. D., Van Leer, B., and Roberts, W. W. (1982). A comparative study of computational methods in gas dynamics. *Astronomy and Astrophysics*, 108:76–84. 41

[93] Van Holten, T., Pavel, M. D., and Smits, G. N. (1999). Aeroelastic stability of modern wind turbines, Final report phase I. Memorandum M-880, TU Delft. 7, 10

[94] Van Ingren, J. L. (1956). A suggested semi-empirical method for the calculation of the boundary layer transition region. Report VTH-74, University of Delft, Department of Aerospace Engineering, Delft, The Netherlands. 5

[95] Van Leer, B. (1979). Towards the ultimate conservative difference scheme. v. a second order sequel to Godunov's method. *Journal of Computational Physics*, 32(1):101–136. 41

[96] Van Leer, B., Lee, W.-T., and Roe, P. L. (1991). Characteristic time-stepping or local preconditioning of the euler equations. In *10th Computational Fluid Dynamics Conference*, Honolulu, HI. AIAA 1991-1552. 66

[97] Vatne, S. R. (2008). *Aeroelastic Instability and Flutter for a 10 MW Wind Turbine*. PhD thesis, Norwegian University of Science and Technology. 10

[98] Venkatakrishnan, V. (1993). On the accuracy of limiters and convergence to steady state solutions. In *31st Aerospace Sciences Meeting*, Reno, NV. AIAA 93-0880. 42

[99] Weiss, J. M. and Smith, W. A. (1995). Preconditioning applied to variable and constant density flows. *AIAA Journal*, 33(11):2050–2057. 66

[100] White, F. M. (1991). *Viscous Fluid Flow*. McGraw-Hill, New York. 16

[101] Williamson, C. H. K. (1988). Defining a universal and continuous Strouhal-Reynolds number relationship for the laminar vortex shedding of a circular cylinder. *Physics of Fluids*, 31:2742–2744. 87

[102] Yates, E. C. J. (1985). AGARD standard aeroelastic configurations for dynamic response i - wing 445.6. In *Proceedings of the 61st Meeting of the Structures and Materials Panel*, Germany. AGARD-R-765. 88, 89

[103] Yates, E. C., J., Land, N. S., and Fougher, J. T., J. (1963). Measured and calculated subsonic and transonic flutter characteristics of a 45 deg sweptback wing planform in air and in freon-12 in the langley transonic dynamics tunnel. NASA TN D-1616. 88, 91

[104] Yoon, S. and Jameson, A. (1986). A multigrid LU-SSOR scheme for approximate newton iteration applied to the Euler equations. Contractor Report 179524, NASA. 50, 51

Appendix

A Face Vectors in 3-D

This appendix shows the calculation of face vectors on a 3-D structured computational grid as described in Hirsch [32] and Blazek [11]. Since each face is shared by two volumes, only three face vectors are required per volume. The remaining three face vectors can be retrived from the neighboring volumes as needed. To start, consider the generic volume shown in Fig. 1. Using this notation, the x, y, and z components of the face vectors S_1, S_2, and S_3 can be calculated as

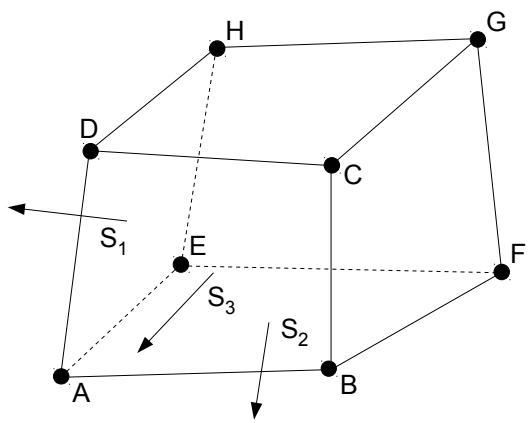

Figure 1: Face vectors on a 3-D volume

$$S_{1x} = \frac{1}{2}\left[(y_H - y_A)(z_D - z_E) - (z_H - z_A)(y_D - y_E)\right] \tag{1}$$

$$S_{1y} = \frac{1}{2}\left[(z_H - z_A)(x_D - x_E) - (x_H - x_A)(z_D - z_E)\right] \tag{2}$$

$$S_{1z} = \frac{1}{2}\left[(x_H - x_A)(y_D - y_E) - (y_H - y_A)(x_D - x_E)\right] \tag{3}$$

$$S_{2x} = \frac{1}{2}\left[(y_F - y_A)(z_E - z_B) - (z_F - z_A)(y_E - y_B)\right] \tag{4}$$

$$S_{2y} = \frac{1}{2}\left[(z_F - z_A)(x_E - x_B) - (x_F - x_A)(z_E - z_B)\right] \tag{5}$$

$$S_{2z} = \frac{1}{2}\left[(x_F - x_A)(y_E - y_B) - (y_F - y_A)(x_E - x_B)\right] \tag{6}$$

$$S_{3x} = \frac{1}{2}\left[(y_C - y_A)(z_B - z_D) - (z_C - z_A)(y_B - y_D)\right] \tag{7}$$

$$S_{3y} = \frac{1}{2}\left[(z_C - z_A)(x_B - x_D) - (x_C - x_A)(z_B - z_D)\right] \tag{8}$$

$$S_{3z} = \frac{1}{2}\left[(x_C - x_A)(y_B - y_D) - (y_C - y_A)(x_B - x_D)\right] \tag{9}$$

Vita

Jason Howison was born in Cincinnati, OH, and is the youngest of three brothers. After moving with his family to Palm Harbor, FL, at the age of 15, he graduated high school in 2001. Jason attended Clemson University, graduating with a B.S. in Mechanical Engineering in 2006 while also completing the cooperative education program. Jason went directly to graduate school at the University of Virginia where he received his M.S. in Mechanical & Aerospace Engineering in 2009. He worked for a year at the Allegany Ballistics Laboratory in Rocket Center, WV, as a solid rocket ballistic analyst before returning to school at the University of Tennessee for his Ph.D. Jason is currently an Assistant Professor in Mechanical Engineering at The Citadel in Charleston, SC. He lives there with his wife and children.